



MISURI

MCGILL SCIENCE UNDERGRADUATE RESEARCH JOURNAL

VOLUME 19 | ISSUE 1 | APRIL 2024

ON THE COVER

An ever-expanding body of science strives to shine light on the secrets of the distant universe, including vast sectors of space whose soul-stirring mysteries have been capturing the imagination of humankind since time immemorial. On page 13, author Wiktoria Tarnopolska explores various models for black holes and their interaction with photons and spacetime.

The painting on the cover, created using mixed media — oil and digital — depicts this journal's home campus of McGill University at the foot of Montréal's Mount Royal. The city-scape, illuminated by the blinding accretion disc of a black hole in the night sky, brings these elusive and distant bodies within reach of scientific and creative minds alike.

Designed by **David Derish**

BOARD 2023-2024

Editors-in-Chief

David Derish
Medicine
Laura Reumont
Computer Science

Managing Editors

Armance Volta
Physics
Benjamin Herfray
Mechanical Engineering
Benjamin Lévesque Kinder
Neuroscience
Mina Mahdi
Cognitive Science

Senior Editors

Ines Durant
Physiology
Mackenzie Pereira
Physics
Tiffany Spector
Pharmacology

Editors

Alegria Rohlfs
Immunology
Dashiell Rich
Computer Science
Jessica Mizrahi
Mechanical Engineering
Leah Summers
Pharmacology
Lisa Xie
Biochemistry
Ojas Srivastava
Mathematics and Computer Science
Yavuz Shahzad
Statistics
Aziz Benchabir
Psychology

Former Editor

Layout Designers

Benjamin Herfray
Armance Volta
Mackenzie Pereira
Mina Mahdi
Ojas Srivastava

Graphic Designer

David Derish

805 Sherbrooke St. West, Room 1B22
Montreal, Quebec, H3A 2K6 Canada
Phone: (514) 398-6979
Fax: (514) 398-6766
Email: msurj.sus@mail.mcgill.ca
Website: <https://msurjonline.mcgill.ca/about/editorialTeam>

TABLE OF CONTENTS

VII Foreword

IX Acknowledgements

RESEARCH ARTICLES

1 An Optimization of Experimental Conditions to Characterize Perineuronal Nets in the Human Cerebellum
Lena Hug, Refilwe Mpai

7 Orthopedics in Space Travel: Developing Procedures to Evaluate the Safety of Implants Amidst the Rise of Commercial Space Tourism
Chloe Jacquet, Jay Patel, Pierre Khoury, Xingbo Huang, Theodore Glavas

13 Properties of Accretion Discs Around Black Holes Through Modelling
Wiktoria Tarnopolska

19 The Effects of Climate Change on Oceanic Sonar Use in the Upper European Continental Shelf
Abigail Farkas

27 Cinnamomum cassia and Origanum compactum Essential Oils as Antifungal Candidates for the Treatment of Aspergillosis
Manon Leclercq, Isciane Commenge, Marylou Bouriot, Floricia Crusset, Patrick Gonzalez, Julien Grimaud, Frank Yates, Jacqueline Sarfati-Bert, Agnès Saint-Pol

33 Elevated Ambient Carbon Dioxide Levels Induce Attraction but Not Attachment of Adult *Ixodes scapularis* in Artificial Membrane Feedings
Elizabeth Breitbach, Victor Lai

39 A Replication Study to Evaluate the Effects of Awe on Humility
Alexandra Bertrand, Jonah Kimmel, Salomé Duhamel, Héloïse Puel, Alexandra Schifano, and Émilie Wood

REVIEW ARTICLES

47 Antimicrobial Resistance Mechanisms: Using Examples from Gram-Positive and Gram-Negative Bacteria
Zhiwen Xiao

53 Endocrine Resistance in Breast Cancer: The Role of mTOR Signaling in Mediating Resistance to Selective Estrogen Receptor Modulators
Olivia Dumas

59 The Use of Leishmania-Derived Extracellular Vesicles as a Vaccine Platform Against Emerging Viral Diseases: A Systematic Review
Susan Cai

FOREWORD

Dear Reader,

As we reflect on 19 years of publication, we are filled with pride in the legacy built by generations of authors, editors, and peer-reviewers. Each passing volume is testament to the ingenuity and perseverance of our undergraduate peers, who continue to be at the forefront of scientific research.

Featured in this issue is an investigation into the safety of orthopaedic implants during rocket liftoffs. The authors were driven by the rise of space tourism and the growing potential for passengers with implants. We believe this embodies the remarkable spirit of undergraduate researchers, who not only anticipate the future but also work hard to improve it.

With the privilege of leading our brilliant team, comes the responsibility of honouring the legacy of our journal. This year, we strengthened our efforts to engage students in new ways, including running a research seminar and joining the journal collection into McGill University's institutional library. We hope these initiatives inspire more curious students to conduct their own research projects in their quests for knowledge, innovation, and progress.

We present to you the 19th volume of the McGill Science Undergraduate Research Journal, enclosing ten research and review articles authored by undergraduates across several universities. The science they cover is expansive, from immunology to astrophysics, and we hope their insights will inspire you to think of all the discoveries and changes that lie ahead.

On behalf of our entire editorial board, we wholeheartedly thank you.

Laura Reumont & David Derish
Editors-in-Chief

ACKNOWLEDGEMENTS

The McGill Science Undergraduate Research Journal would like to thank its generous contributors without whom this journal would not have been possible.

We thank the librarians of McGill University for their guidance. We thank the Office for Science Education for their continued support of both undergraduate research at McGill and the MSURJ. Furthermore, we thank our advisors Dr. Armin Yazdani, Dr. Christie D. Rowe, and John Ni for their continued support.

We thank all our financial supporters in the McGill community for their generous support:

Faculty of Medicine and Health Sciences
Centre de recherche en biologie structurale
Department of Physics
Department of Pharmacology and Therapeutics
Department of Physiology
Department of Anatomy and Cell Biology
Science Undergraduate Society of McGill University

Finally, we thank the peer reviewers, including Dr. Anna Obiegala, Dr. Ilia Rochlin, Dr. Jasmin Chahal, Dr. Jeff Jenks, Dr. Alfonso Bucio, Dr. John White, Dr. John Paul Minda, Dr. Daniel Brown, Eric Siegel, Honghui Liu, and the anonymous peer-reviewers. Their careful revision of the articles is critical to the success of the 19th volume of the MSURJ.

Research Article

¹Department of Psychology,
McGill University, Montreal,
QC, Canada

²Department of Psychiatry,
McGill University, Montreal,
QC, Canada

Keywords

Perineuronal nets, child abuse,
major depression, cerebellum,
RNAscope, immunofluorescence

Email Correspondence

lena.hug@mail.mcgill.ca

<https://doi.org/10.26443/msurj.v19i1.224>

©The Authors. This article is
published under a CC-BY license:
<https://creativecommons.org/licenses/by/4.0/>

Lena Hug¹, Refilwe Mpai²

Optimization of Experimental Conditions to Characterize Perineuronal Nets in the Human Cerebellum

Abstract

During childhood and adolescence, the brain is highly responsive to external stimuli compared to adulthood. Perineuronal nets (PNNs), play a crucial role during this period by reducing neuroplasticity. These mesh-like structures protect and fortify neural connections between cells. Child abuse includes physical, emotional, and sexual abuse and/or neglect¹. It is consistently associated with negative mental and physical health outcomes, underscoring the importance of identifying risk and resilience factors for effective prevention of such outcomes. Our laboratory focuses on understanding the cellular and molecular neuroanatomy of major depression and the lasting impact of child abuse (CA) on the brain. However, the impact of CA on PNNs remains relatively unexplored. How does CA influence the brain, potentially contributing to negative outcomes in the future? Samples from post-mortem human brain cerebellum were dissected and then used to perform RNAscope experiments to label glutamatergic, GABAergic, and parvalbumin-positive cells, following a brief IF protocol using Wisteria Floribunda Lectin (WFL) to visualize PNNs. The RNAscope protocol was successfully optimized by the addition of normal donkey serum (NDS), manipulation of incubation time, and WFL concentration. PVALB+ mRNA expression was positively identified in Purkinje cells, molecular layer interneurons, and deep cerebellar nucleus (DCN) neurons. SLC17A7+ mRNA expression was evident in granule cells and excitatory projection DCN neurons. GAD1+ mRNA expression was detected in Purkinje cells and inhibitory DCN neurons. These results provide an experimental protocol for future studies investigating the role of PNNs in the human cerebellum. We propose that CA alters the recruitment of PNNs, influencing circuitry and potentially increasing susceptibility to various mental illnesses, including major depressive disorder (MDD). MDD, also called clinical depression, causes a persistent feeling of sadness and loss of interest. This study aims to optimize fluorescent in situ hybridization (FISH, RNA-scope) and immunofluorescence (IF) markers for the localization and phenotyping of PNN-enwrapped neurons in the human cerebellum. This article describes problems we encountered when running experiments and ways to optimize them. As this work is preliminary, it will help develop future protocols for exploring the effects of depression on PNNs and the phenotype of the cells they encircle. Comparing depressed individuals with and without a history of CA with neurologically and psychiatrically healthy controls will allow us to determine whether a history of CA impacts the distribution and density of PNNs.

Introduction

The pivotal periods of childhood and adolescence are characterized by high neuroplasticity, in which the brain is highly adaptable and neuronal connections can undergo significant changes. A child's environment is thus highly important for their developmental trajectory. Throughout childhood, the brain is especially responsive to external stimuli and is therefore more malleable relative to adulthood. PNNs are key structures that reduce neural plasticity and mark an end to this critical period. These intricate structures of condensed extracellular matrix consist of chondroitin sulphate proteoglycans (CSPGs)² and lecticans, forming a mesh-like net around specific brain cells. Serving as both protectors and solidifiers, PNNs fortify the connections between cells, ultimately closing the window of critical plasticity³. In this way, PNNs are also involved in encoding, maintaining, and updating memories⁴. Previous studies have shown that the digestion of PNNs in animal models increases plasticity, leading to enhanced memory interference from competing information during the encoding process. But this removal can render neurons vulnerable to damage, particularly in neurodegenerative conditions³.

CA encompasses physical, emotional, or sexual maltreatment and neglect of a child, leaving enduring impacts on the brain and severe consequences

for psychological development. Individuals with both MDD and a history of CA tend to experience more severe diagnoses, recurring episodes, and resistance to treatment⁵. Results from the study by Gruhn and Compas (2020) show that CA is associated with poor emotion regulation, increased social avoidance, expression of negative emotion in stressful moments and emotion suppression⁶. Hart and Rubia (2012) use neuroimaging studies to show that childhood maltreatment is associated with neuropsychological impairments in academic achievement, IQ, memory, emotion processing, attention, and response inhibition⁷. Evidence has emerged for maltreatment-associated structural deficits in the adult hippocampus, corpus callosum, anterior cingulate cortex (ACC), orbitofrontal cortex (OFC), and dorsolateral prefrontal cortex (PFC) have all been shown in the literature⁸. Moreover, CA is associated with increased recruitment of PNNs in the ventromedial prefrontal cortex in depressed suicides (DS) compared to DS with no history of CA and healthy controls⁹. Aside from this study, the impact of CA on PNNs remains relatively unexplored.

Traditionally, the cerebellum (CB) has been primarily associated with maintaining balance and controlling motor functions. Nonetheless, recent studies have begun to uncover additional roles of the CB, such as regulating emotions, suppressing impulsive decision-making, enhancing atten-

tion, and facilitating working memory^{10,11}. The CB is increasingly implicated in many psychiatric disorders, including attention deficit hyperactivity disorder, autism spectrum disorders, schizophrenia, bipolar disorder, major depressive disorder, and anxiety disorders¹²⁻¹⁴. The vast majority of existing studies looking at psychiatric disorders have employed neuroimaging methods. However, little is known about the cellular and molecular changes in the CB that are caused by psychiatric disorders, as well as the impact of CA on this brain region.

In regions where PNNs have been localized, these structures were shown to surround parvalbumin-expressing (PV) inhibitory neurons. PV neurons have been shown to regulate cortical sensory plasticity during both child development and adulthood⁹. Unpublished work from the Mechawar lab has shown that, in healthy individuals with no history of neurological or psychiatric illnesses, PNNs in the deep cerebellar nuclei (DCN) preferentially surround SLC17A7+/PVALB+ cells (~70%), while a much smaller percentage surround GAD1+/PVALB+ cells (~20%). The remainder of PNNs are surrounding PVALB- cells that are either GAD1+ or SLC17A7+. SLC17A7 is a gene expressed in glutamatergic cells, GAD1 is a gene expressed in inhibitory cells, and PVALB is expressed in PV+ cells.

PV+ cells play a crucial role in generating and sustaining cortical gamma oscillations, which are essential for the consolidation and retrieval of memories. In the absence of proper regulation of cortical PV+ neuron activity, there is a disruption in the excitatory-inhibitory balance and signal transmission within vital neural networks associated with cognition. Such disruptions that may be implicated in CA could contribute to changes in inhibitory signaling and gamma oscillations implicated in various psychiatric conditions that manifest during childhood and early adulthood¹⁵. As the cerebellum's role in psychiatric conditions is increasingly studied, PV+ neurons in this brain region could influence signal transmission and other cognitive processes.

The study by Tanti et al. (2022) looked at PNN changes in the ventromedial prefrontal cortex (vmPFC)⁹. This brain region is involved in emotional learning, which is functionally altered in individuals with a history of child abuse. They investigated how both PNNs and the phenotype of cells they surround are impacted in depressed suicides both with and without a history of childhood, as well as in comparison to psychologically healthy controls, in the CB. We hypothesize that child abuse alters the recruitment of PNNs, affecting the circuitry, and possibly predisposing individuals with such a history to various mental illnesses including MDD. With the results we have obtained in the deep cerebellar nuclei, we anticipate that the PNNs will be reduced in DS-CA compared to the other groups, resulting in asynchronous cell firing in the DCN and impacting communication between the CB and other regions involved in MDD like the vmPFC, hippocampus, and amygdala. We anticipated DS (without CA) condition to look like the control condition, a hypothesis aligned with Tanti et al (2022)⁹.

As this work is still in progress, this study aims to establish a working RNAscope and IF protocol to investigate how both cerebellar PNNs and the phenotype of cells they surround are impacted in depressed suicides with or without a history of childhood maltreatment compared to neurologically and psychiatrically healthy controls. By optimizing fluorescent in situ hybridization (FISH, RNA-scope) and immunofluorescence (IF) markers for the localization and phenotyping of PNN-enwrapped neurons in the human CB, we hope to provide a strong protocol for future studies.

Materials and Methods

To test our hypothesis, we dissected human post-mortem brain samples and performed fluorescent in situ hybridization (FISH; RNAscope) experiments to label vesicular glutamate transporter 1 (SLC17A7+), glutamate

decarboxylase 1 (GAD1+), and Parvalbumin (PVALB+) cells. We then performed a short immunofluorescence (IF) protocol using Wisteria Floribunda Lectin (WFL) to visualize PNNs and looked at our samples using a VS120 Olympus Slide scanner microscope. Nuclei 6-diamidino-2-phenylindole (DAPI) helped visualize nuclear DNA in cells, as it is a marker for membrane viability. In theory, WFL (green) should appear with PVALB (white dots), as it surrounds neuronal cells (with a blue nucleus). The association of WFL and PVALB in the result should indicate PNN's presence¹⁶. See Figure 1B of the cortex.

Human post-mortem brain samples

The lab works in close relation with the Douglas-Bell Canada Brain Bank in Montréal. Brain samples underwent a series of procedures prior to inclusion in this project. Consent from the next of kin and the Quebec Coroner's Office was secured and helped us conduct standardized psychological autopsies for gathering phenotypic information. Individuals with neurological or neurodegenerative disorders were excluded. After examination of medical charts and Coroner records, case and control groups were defined. Additionally, proxy-based interviews with individuals closely acquainted with the deceased obtained from hospitals, the Coroner's office, and social services provided supplementary information. To qualify individuals according to the DSM-IV diagnostic criterion, a panel of clinicians listed and revised the criterion based on questionnaires covering sociodemographic characteristics, social developmental history, DSM-IV axis I diagnostic information, and behavioural traits. This was conducted before the death of patients or by questioning their relatives. Using Childhood Experience of Care and Abuse (CECA)⁹ interviews, clinicians were able to identify the presence of severe child abuse, focusing on sexual and physical abuse and neglect. Toxicological assessments and medication histories were also obtained. Subject characteristics are described in Table 1. The REB of the protocol is # IUSMD-20-35. All individuals were Caucasian. The method of death wasn't shared with the researchers. Therefore, we only have information on whether the individual died by accident, natural causes, or suicide.

While depression is almost 2 times more likely to occur in females than in males, completed suicides are more common in men. Therefore, our depressed suicides tend to include more men than women. In addition, we are using mostly the same cohort used in Tanti et al. (2022). Keeping the same subjects helps us to compare the changes in PNNs in both the vmPFC⁹ and the CB. This way, we can better understand the impact of child abuse on PNNs in different regions at the same time.

Table 1. Subject Characteristics — CTRL: Control; DS: Depressed suicide; DS-CA: Depressed suicide with a history of child abuse.

	CTRL	DS	DS-CA
Axis I Diagnostic	Nil	MDD/DD-NOS(2)	MDD-DD-NOS(1)
Age (years)	45±5.27	49±3.29	41±3.17
Sex (F/M)	2F/13M	2F/13M	41 ± 3.17
Post-mortem interval (hours)	37±4.66	46±8.16	46±6.14
Substance dependence	1	5	6
Tissue pH	6±0.1	7±5.3	7±0.1
Medication	SSRI (1)	Benzodia-zepines (5), SSRI (3), SNRI (1), Anti-psychotics (2), TCA (1), Antimanic (1)	Benzodia-zepines (3), SSRI (4), SNRI (1), Antipsychotics (3), Antimanic (1), Opiate (1)

Tissue dissections

The dissections were performed by expert brain bank staff on fresh-frozen 1 cm-thick sections, using a human brain atlas. Sections of the deep cerebellar nuclei (DCN) were dissected at the level of the dentate nucleus. A section of the cerebellar cortex was used for comparison. A ventromedial prefrontal cortex (vmPFC) region was used as a positive control but is not displayed in the figures. Samples were kept frozen at -80°C until cryosection.

RNAscope and Immunofluorescence

Since we sought to uncover the phenotype of cells surrounded by PNNs, immunofluorescence was limiting for various reasons. Due to the loss of PV antigenicity that occurs during the freezing process, antibodies against PV neurons don't work in frozen tissue. On the other hand, the markers for PNNs don't work in long-term fixed tissue. Due to the time constraint of this project, using fresh-fixed tissue was not feasible as it is dependent on how often a brain is received (average: 1 – 3 a week). Moreover, inhibitory interneuron markers commonly used in the cerebrum do not work as well in the CB. To circumvent these issues, RNAscope was a logical step as we could label PNNs and all our cells of interest in the tissue we had available.

Frozen unfixed blocks were cut serially into $10\ \mu\text{m}$ sections using a cryostat and collected on SuperFrost[®] charged slides. The slides were stored at -80°C until they were used for experimentation. Advanced Cell Diagnostics RNAscope probes and reagents were used to perform the RNAscope experiment, following the manufacturer's instructions. Upon removal from the freezer, the sections were initially fixed in cold (4°C) 10% neutral buffered formalin for 15 minutes. Subsequently, they underwent dehydration through increasing gradients of ethanol baths (75%, 95%, and 100%) and were air-dried for 5 minutes. To quench endogenous peroxidase activity, a 10-minute incubation at room temperature was carried out using 3% hydrogen peroxide in PBS. Following this, the designated probes: Hs-GAD1 (no. 573061.o1.C3); Hs-SLC17A7 (no.415611); Hs-PVALB (no.422181.C2) were hybridized for 2 hours at 40°C in a humidity-controlled oven. Due to limitations of the number of channels that can be included in one experiment, we had two conditions. The first was PVALB+SLC17A7+, where PVALB was diluted in the C1 SLC17A7. The second was PVALB+GAD1+, where both probes were diluted in probe diluent. During our troubleshooting, we included a third condition which served as a negative control, with only probe diluent and opal dyes. If our conditions with the active probes looked like the negative control, we concluded that further optimization of the experiment was necessary. Amplifiers were added using the proprietary AMP reagents, and the signal was visualized through probe-specific HRP-based detection by tyramine signal amplification with Opal dyes (Opal 570 and Opal 690 for SLC17A7/GAD1 and PVALB respectively; Perkin Elmer) diluted 1:500.

We then conducted a short immunofluorescence measure using biotinylated Wisteria Floribunda Lectin (WFL). Slides were rinsed in PBS and incubated in a solution of WFL (1:500) diluted in PBS/0.2% Triton-X/5% normal donkey serum (NDS) for 15 minutes at room temperature. Slides were rinsed again with PBS and incubated in a secondary solution of Alexa 488 conjugated streptavidin (1:500) diluted in PBS/0.2% Triton-X/5% NDS to detect PNNs. During our optimization process, we made changes to the length of incubations, the percentage of NDS, as well as the concentration of WFL used. Sections were rinsed. Endogenous autofluorescence from lipofuscin and cellular debris was quenched with TrueBlack (Biotium), omitted for tissues used for intensity measurements. Sections were mounted on SuperFrost[®] charged slides and cover slipped with Vectashield mounting medium (Vector Laboratories, H-1800).

Microscope and Image analysis

Image acquisitions were performed on a FV1200 laser scanning confocal microscope using a 10X objective. Charged slides with two sequential sections per subject were used, where we visualized DAPI (405), WFL with Streptavidin-Alexa 488, either GAD1 or SLC17A7 with Opal dye 570, and PVALB with Opal dye 690. The images served for cell counting and overlap.

Results

The current investigation improves the existing experimental procedure for examining the influence of suicidal depression and childhood maltreatment on PNNs and neurons in the deep cerebellar nuclei. This methodology is a refinement of two previous studies carried out in the lab. We successfully optimized an RNAscope protocol. Our initial trial involved negative control slides, visually distinct from slides where the RNAscope probes were applied. This distinction provides us with confidence in the authenticity of the observed staining.

Specifically, PVALB+ mRNA expression was identified in Purkinje cells, molecular layer interneurons, and DCN neurons. SLC17A7+ mRNA expression was evident in granule cells and excitatory DCN neurons. GAD1+ mRNA expression was detected in Purkinje cells and inhibitory DCN neurons (see Figure 1). The absence of staining resembling the structure of PNNs suggests that the morphology of PNNs is not present. We can tell that the WFL staining was suboptimal in Figure 1, as the staining is similar to non-specific lipofuscin staining.

The validity of the staining was verified using the cerebellar cortex as a comparison, as more is known about the expected staining pattern of these probes than in the DCN. We were able to optimize the WFL IF separately but encountered problems when the IF was conducted in combination with RNAscope experiments. During the initial RNAscope attempt, WFL was diluted at a ratio of 1:500 in PBS+0.2% Triton-X (blocking solution) for a 15-minute incubation, followed by the dilution of conjugated streptavidin 488 in the same solution, without the addition of TrueBlack. In this condition, WFL staining resembled the staining pattern seen in the negative control. The expected PNN-patterned staining was not seen. Moreover, in the absence of TrueBlack, there was a lot of background lipofuscin, especially in the 488 channel. Subsequent IF experiments excluding the RNAscope steps but including TrueBlack, resulted in tissue dissolution, necessitating repetition. In the revised experiment, 10% neutral buffered formalin (NBF) and ethanol dehydration steps at increasing concentrations were introduced to enhance tissue adhesion to the slides. As these are the first steps of an RNAscope experiment there was no concern that this would negatively affect staining or tissue quality.

To further optimize the experiment, two other variables were manipulated: the concentration of WFL (1:250 vs. 1:500, settling on 1:500) and the incubation duration (15 mins vs. 30 mins). Previous IF experiments conducted over two days in the lab using WFL used a concentration of 1:1000. As the goal was to conduct the IF in a short amount of time following the RNAscope, we increased the concentration to compensate for the reduced time. 1:1000 was not sufficient to examine PNNs with the reduced incubation time. PNNs could be visualized well at 1:500, therefore that was the concentration we chose to proceed with. There was no meaningful difference in staining quality between a 15-minute and a 30-minute incubation at room temperature. We therefore chose to proceed with the shortest possible time, which was 15 minutes. When we included TrueBlack following the formalin and alcohol steps, the endogenous lipofuscin was quenched, allowing us to better differentiate true signal from noise.

After this, 5% normal donkey serum (NDS) was incorporated into the

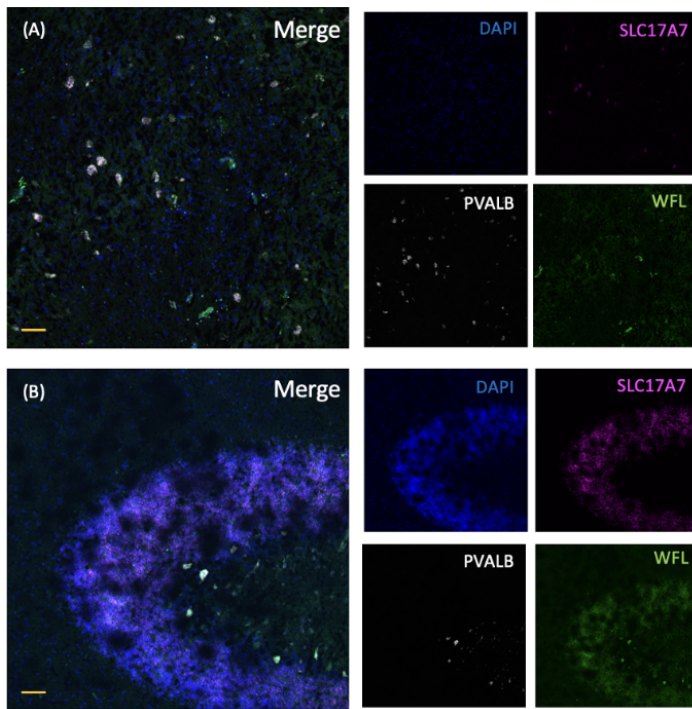


Figure 1. Representative image of 2 males depressed suicides with no history of CA. (A) DCN merge: DAPI marker of cell nuclei in blue, SLC17A7 marker of excitatory cell + in pink, PVALB marker of PV neurons in white, WFL marker of PNN in green. (B) Representative image of the cerebellar cortex as a comparison for staining validity. Coronal section corresponding to Brodmann areas 11 and 12. We can see PNN are present by the superposition of PVALB and WFL signals. 50 μ m scale bars

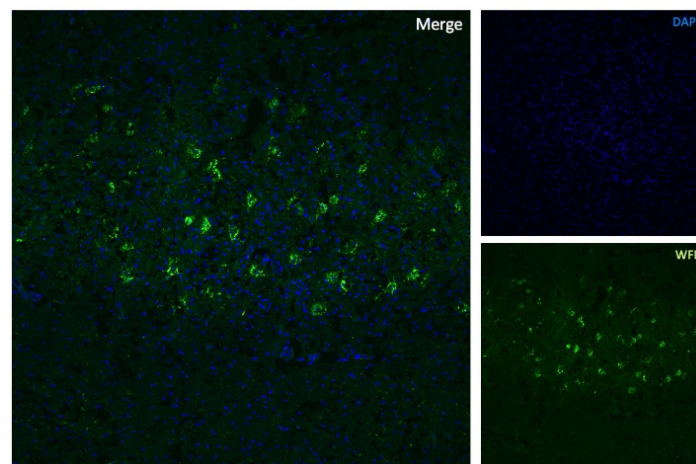


Figure 2. Representative figure of WFL in DCN after IF optimization WFL worked with the addition of 5% NDS and TrueBlack 50 μ m scale bars.

will be evaluated under different conditions, and their role will be better assessed. Following optimization, the complete cohort will be processed in four batches, and all slides will be subjected to scanning using a slide scanner. PNNs, glutamatergic cells (SLC17A7), GABAergic cells (GAD1), and PV cells will undergo quantification through QuPath. The densities and extent of overlap between each marker will then be compared across three groups: depressed suicides (DS), depressed suicides with a history of child abuse (DS-CA), and controls (CTRL). The outcomes of this analysis will enable us to address our hypothesis. Future research could use QuPath, following the acquisition of images using a slide scanner to visualize the entire section of tissue.

blocking solution to mitigate non-specific antibody binding, along with the inclusion of NBF and ethanol steps. This, in combination with TrueBlack, allowed for less background non-specific staining. Additionally, a positive control region, the ventromedial prefrontal cortex (vmPFC), known for its high PNN density in layers 3–5 was introduced. This served to distinguish whether the issue lay with the lectin (indicated by an absence of WFL+ PNNs in the vmPFC) or was specific to the CB (WFL+ PNNs in the vmPFC but not in the CB). Notably, the staining was successful (see Figure 2). Upon repetition, and incorporating the RNAscope, the experiment failed without clear reasons. Consequently, further optimization of the IF in conjunction with the RNAscope will be pursued.

Discussion

The present study is ongoing, and the results outlined are preliminary and will be used to further optimize the methodology. The concentration of WFL and incubation length have been manipulated in this study. However, future steps include examining variables such as the concentration of Triton-X (or perhaps omitting it) or the incubation temperature, to help speed up the reaction. WFL (also known as WFA) has been used, in the past, as a marker for PNNs in the CB. Unpublished work from the Mechawar lab has used both WFL and ACAN and shown significant results. In unpublished work conducted in controls, we labelled PNNs using both WFL and ACAN to examine whether there were differences in staining patterns. As both markers were good quality, and there was almost a complete overlap of the two markers, we then proceeded with WFL, the more canonical marker.

The optimization of our experimentations should provide insightful results. This molecular biology work will serve as a breeding ground for future research on the subject. Once optimization is complete, the PNN population

We hypothesize a reduction in PNNs among those with a history of suicidal depression and child abuse (DS-CA) compared to other groups. This reduction may lead to asynchronous cell firing in the DCN, affecting communication between the CB and other regions implicated in MDD, such as the ventromedial prefrontal cortex (vmPFC), hippocampus, and amygdala.

What if we could manipulate PNN's expression to change those maladaptive responses in later adulthood? Through meticulous adjustment, there exists the potential to disrupt maladaptive memories, as evident in conditions like post-traumatic stress disorder or drug addiction¹⁷. In the context of age-related cognitive decline and dementia, PNNs may play a pivotal role in fortifying memories or even restoring impaired memory with careful modulation¹⁸. Several studies have shown the significance of epigenetics, pointing to disruptions in the HPA axis, plasticity, and myelination as changes observed in individuals with a history of CA¹⁹. These converging molecular components can be affected by CA and increase the susceptibility to mental disorders in adulthood, and should thus be investigated further. As we know that psychotherapy helps to counteract the impact of CA, different types of interventions (e.g., biological/pharmaceutical) for individuals who experienced child abuse are important additions to the research canon²⁰. This study is one of the first to look at cellular and molecular substrates of depression and child abuse, especially in the CB. The impact of CA on PNNs in postmortem tissue is a novel field that has much to reveal.

Acknowledgements

I thank Dr. Naguib Mechawar for this opportunity in his laboratory. Thank you again to MA Davoli and the rest of the team for the inclusivity and the positivity. The work was supported by the Douglas Hospital of Montreal, the McGill University and the Brain Bank of Canada. *This work was supported by a CIHR Project Grant to NM and by HBHL and Brain Canada*

References

1. Ontario Association of Children's Aid Societies. What is child abuse? (2022); <https://www.oacas.org/childrens-aid-child-protection/what-is-abuse/>
2. Kwok, J., Dick, G., Wang, D. & Fawcett, J. Extracellular matrix and perineuronal nets in CNS repair. *Dev. Neurobiol.* **71**, 1073–89 (2011). <https://doi.org/10.1002/dneu.20974>
3. Reichelt, A., Hare, D., Bussey, T. & Saksida, L. Perineuronal Nets: Plasticity, Protection, and Therapeutic Potential. *Trends Neurosci.* **42**, 458–470 (2019). <https://doi.org/10.1016/j.tins.2019.04.003>
4. Carulli, D., Broersen, R., Winter, F., et al. Cerebellar plasticity and associative memories are controlled by perineuronal nets. *Proc. Natl. Acad. Sci.* **117**, 6855–6865 (2020). <https://doi.org/10.1073/pnas.1916163117>
5. Bains, N. & Abdijadid, S. Major depressive disorder (2023); <https://www.ncbi.nlm.nih.gov/books/NBK559078/>
6. Compas, B. E. & Gruhn, M. A. Effects of maltreatment on coping and emotion regulation in childhood and adolescence: A meta-analytic review. *Child Abuse & Neglect* **103**, 104446 (2020). <https://doi.org/10.1016/j.chiabu.2020.104446>
7. Hart, H. & Rubia, K. Neuroimaging of child abuse: a critical review. *Front. Hum. Neurosci.* (2012). <https://doi.org/10.3389/fnhum.2012.00052>
8. Teicher, M., Samson, J. & et al., C. A. The effects of childhood maltreatment on brain structure, function and connectivity. *Nat. Rev. Neurosci.* **17**, 652–666 (2016). <https://doi.org/10.1038/nrn.2016.111>
9. Tanti, A., Belliveau, C., Nagy, C. & et al. Child abuse associates with increased recruitment of perineuronal nets in the ventromedial prefrontal cortex: a possible implication of oligodendrocyte progenitor cells. *Mol. Psychiatry*. **27**, 1552–1561 (2022). <https://doi.org/10.1038/s41380-021-01372-y>
10. Ravizza, S., McCormick, C., Schlerf, J., Justus, T. & Ivry, R. Cerebellar damage produces selective deficits in verbal working memory. *Brain* **129**, 306–320 (2006). <https://doi.org/10.1093/brain/awh685>
11. Schmahmann, J., Weilburg, J. & Sherman, J. The neuropsychiatry of the cerebellum - insights from the clinic. *Cerebellum* **6**, 254–67 (2007). <https://doi.org/10.1080/14734220701490995>
12. Phillips, J., Hewedi, D., Eissa, A. & Moustafa, A. The cerebellum and psychiatric disorders. *Front. Public Health* **3**, 132123 (2015). <https://doi.org/10.3389/fpubh.2015.00066>
13. Chen, T. et al. Resting-state fMRI mapping of cerebellar functional dysconnections involving multiple large-scale networks in patients with schizophrenia. *Schizophr. Res.* **149**, 26–34 (2013). <https://doi.org/10.1016/j.schres.2013.05.029>
14. Baldaçara, L. et al. Is cerebellar volume related to bipolar disorder? *J. Affect. Disord.* **135**, 305–9 (2011). <https://doi.org/10.1016/j.jad.2011.06.059>
15. Rupert, D. & Shea, S. Parvalbumin-Positive Interneurons Regulate Cortical Sensory Plasticity in Adulthood and Development Through Shared Mechanisms. *Front. Neural Circuits* **6**, 886629 (2022). <https://doi.org/10.3389/fncir.2022.886629>
16. Takesian, A. & Hensch, T. Balancing plasticity/stability across brain development. *Prog. Brain Res.* **207**, 3–34 (2013). <https://doi.org/10.1016/B978-0-444-63327-9.00001-1>
17. Sorg, B., Barretta, S. & et al., J. B. Casting a wide net: role of perineuronal nets in neural plasticity. *J. Neurosci.* **36**, 11459–11468 (2016). <https://doi.org/10.1523/JNEUROSCI.2351-16.2016>
18. Brewton, D., Kokash, J., Jimenez, O. & et al. Age-Related Deterioration of Perineuronal Nets in the Primary Auditory Cortex of Mice. *Front. Aging Neurosci.* **8**, 270 (2016). <https://doi.org/10.3389/fnagi.2016.00270>
19. Almeida, D., Ibrahim, P., Nagy, C. & Turecki, G. Molecular impacts of childhood abuse on the human brain. *Neurobiol. Stress* **15**, 100343 (2021). <https://doi.org/10.1016/j.yjnstr.2021.100343>
20. Teicher, M. & Samson, J. Annual Research Review: enduring neurobiological effects of childhood abuse and neglect. *J. Child Psychol. Psychiatry*. **57**, 241–266 (2016). <https://doi.org/10.1111/jcpp.12507>

Research Article

¹Department of Bioengineering, McGill University, Montréal, QC, Canada

²Department of Mechanical Engineering, McGill University, Montréal, QC, Canada

³Department of Electrical Engineering, McGill University, Montréal, QC, Canada

⁴Department of Computer Engineering, McGill University, Montréal, QC, Canada

Keywords

Orthopedic implants, finite element analysis, vibrations, space travel

Email Correspondence

rocketteam.payload@mcgillus.ca

Chloe Jacquet¹, Jay Patel², Pierre Khoury³, Xingbo Huang², Theodore Glavas⁴ Orthopedics in Space Travel: Developing Procedures to Evaluate the Safety of Implants Amidst the Rise of Commercial Space Tourism

Abstract

With the rise of commercial space tourism, the barrier to entry into space lowers. Therefore, passengers with more complex medical conditions are predicted to enter space. This report aims to initiate the development of procedures assessing the safety of space travel for individuals with orthopedic implants. In preparation for the 2023 sounding rocket launch by McGill Rocket Team, the Payload subteam developed a bone model, a human model, a finite element analysis model, and a testing model to determine the safety of orthopedic implants under the harsh conditions of spaceflight. Measuring the dynamic forces of the MRT's *Porthos* rocket in flight yielded vibrations in the 300–2750 Hz range, which is valuable for creating better models of the loading conditions on orthopedic implants *in silico*. Three point bending testing revealed high precision but low accuracy in measuring the mechanical strength of the models. Ultimately, the study recommends adjusting the testing models to prevent oversimplification. Future work should analyze bone screw interfaces on a microscopic level to detect small changes in implant stresses. By implementing these changes, procedures can accurately describe the safety of spaceflight for those with orthopedic implants.

<https://10.26443/msurj.v19i1.221>

©The Authors. This article is published under a CC-BY license: <https://creativecommons.org/licenses/by/4.0/>

Introduction

Orthopedics in space travel

In the age of Blue Origin, Virgin Galactic, Rocketplane Global, and other novel commercial spacecraft companies, space tourism is revolutionizing space travel¹. As the industry grows, we expect a rise in passengers entering space with increasingly diverse medical backgrounds. This will require protocols that evaluate the safety of spaceflight for passengers with different medical conditions. Although we project an increase in this type of research in the coming years, the literature is currently limited. Within the context of orthopedics, it is largely under-researched.

This paper introduces methods to study the impact of flight conditions on the strength of an orthopedic device. The results lay the groundwork for developing future procedures that assess whether individuals with orthopedic implants can safely travel to space. These procedures will hold important implications in both the commercial and professional space industries. Commercially, since orthopedics are often permanent implants, our research questions the accessibility of space travel within a rapidly expanding industry. Professionally, it can help agencies evaluate the risks of potential emergency procedures involving orthopedic implants for use in long-term missions.

McGill Rocket Team

The McGill Rocket Team (MRT) is an interdisciplinary student-led design team tasked with designing and launching a sounding rocket each year. Sounding rockets are designed to complete scientific research in a sub-orbital trajectory². This research is encapsulated in the rocket's payload. Each year, MRT's Payload team designs a scientific experiment that leverages the unique conditions of spaceflight. During the 2023 launch in Timmins, Ontario, the team launched the payload LOVE (Launching Orthopedics Vibration Experiment) on MRT's *Porthos* rocket at an apogee of 2400 m. LOVE was MRT's first attempt to initiate research in the sphere of orthopedics within space travel. This paper presents the experiment's findings and discusses methods for assessing the safety of orthopedic implants in space travel, as well as how to evaluate the quality of these methods.

Model Development

Bone Model

For pilot testing, long bone screw-plate fixations were chosen due to their simple modeling and high failure rates³. High clinical failure rates were optimal for modeling as the team aimed to evaluate the most vulnerable orthopedic fixations. The independent variable in the study was bone density. Decreased bone density, otherwise known as osteopenia, is a widely

observed phenomena amongst astronauts subjected to long periods of decreased gravitational forces, particularly in load-bearing bones like the tibia⁴. With this in mind, models of both healthy and osteopenic bone were included in the payload. Bone consists of two distinct components: the outer cortical layers and the inner cancellous tissues. Cortical bone is hard and stiff with high mechanical properties, whereas cancellous bone is soft and spongy with low mechanical properties. Therefore, the biomechanical contributions of cancellous bone were considered negligible and excluded from the model. Nevertheless, bone loss manifests differently in the two bone components. Whereas cancellous bone uniformly increases porosity in response to osteoclast dominance, cortical bone resorption occurs primarily on the innermost layer^{5,6}. As a result, osteopenia presents as cortical thinning, which we simulated by decreasing the cortical thickness of the bone samples.

Another component of the bone model is the fracture type. Depending on the mechanism of injury, three common fracture types can occur: simple, wedge, and complex⁷. For feasibility, only simple fractures were considered. Complex fractures, such as spiral fractures, often require more intricate internal fixations, which is beyond the scope of our abilities⁷. Wedge fracture patterns vastly complicate modeling and would prevent thorough and substantial pre-flight modeling. Therefore, a simple fracture was modeled in the diaphyseal portion of the tibia. To simulate the least stable fixation condition, oblique fractures were modeled where transverse fractures have higher mechanical stability. Since oblique fractures most commonly range between 10–40 degrees from the horizontal axis⁸, we selected a 23 degree angle to maximize instability without interfering with the screws.

When selecting a bone material, the team considered three options as human bone analogues: animal bones, 3D printed segments, and composite biomechanical models. To simulate the mechanical strength of bone most accurately, the team prioritised a close match on Young's modulus and cortical thickness. Human cortical bone has a Young's modulus of around 16 GPa⁹. Common animal bones have both a larger cortical thickness and a lower Young's modulus compared to humans¹⁰. Furthermore, the Payload could only fit four samples: two healthy and two osteopenic models. Due to the experiment's limited repetition, inconsistencies between samples would thus introduce too great an uncertainty, disqualifying the animal bone. Traditional 3D printing methods were also unsuitable as they could not achieve the necessary Young's modulus¹¹. Consequently, the team selected Sawbones glass fiber epoxy composites from Pacific Research Laboratories, for their accurate simulation of the biomechanical properties of cortical bone with a Young's Modulus of 16 GPa¹². For order of magnitude validation, the same experiment was performed on juvenile bovine tibias. These were tested against the control and flight samples.

Human Model

The payload's structure was designed to incorporate the orthopedics experiment, particularly how the bone analogs would connect to the structure. During this design phase, the team had to make assumptions to simplify the anatomical bone model, making the project feasible within time and space constraints. The first assumption regarded the biomechanics of the joints surrounding the tibia, which largely determine the forces felt by the bone and ultimately describe the effects of flight on the bone. However, due to the small space in the payload (roughly 10 by 10 by 25 cm), the joints had to be simplified to fit multiple samples. Through consultation with the McGill Orthopaedics Research Laboratory (ORL) and McGill Musculoskeletal Biomechanics Research Laboratory, the team found that the knee-tibia joint acted like a pinned or hinged connection, while the tibia-ankle joint acted as a fixed connection. Similarly for space constraints, the team chose to ignore the mass and mechanical properties of the flesh surrounding the tibia. This flesh is made up largely of the gastrocnemius muscle and the attached Achilles tendon, which lie at the back of the leg.

Through comparison of their Young's moduli (440 kPa compared to 16 GPa), the flesh is more than 10^4 times weaker than the tibia's cortical bone, or the bone analogs used in this experiment⁹. This justifies the choice to ignore the muscles and tendons surrounding the tibia in our payload, as they do not have a significant effect on the strength of the sample. These two assumptions, to simplify the joints and ignore the flesh, allowed for a total of four fractured and plated samples in the final payload.

One of the experiment's design variables was the angle at which to hold the bones at during flight. Since the force would be transferred into the samples through vertical acceleration (G-forces) and vibrations from the engine, this orientation variable was extremely important to define. The team researched how astronauts sit in human-rated capsules, like Blue Origin's suborbital New Shepard¹³. The team determined that an angle of 25 degrees from the horizontal would replicate seating conditions closely. These assumptions and simplifications led us to the final design of our structure (Figure 1).

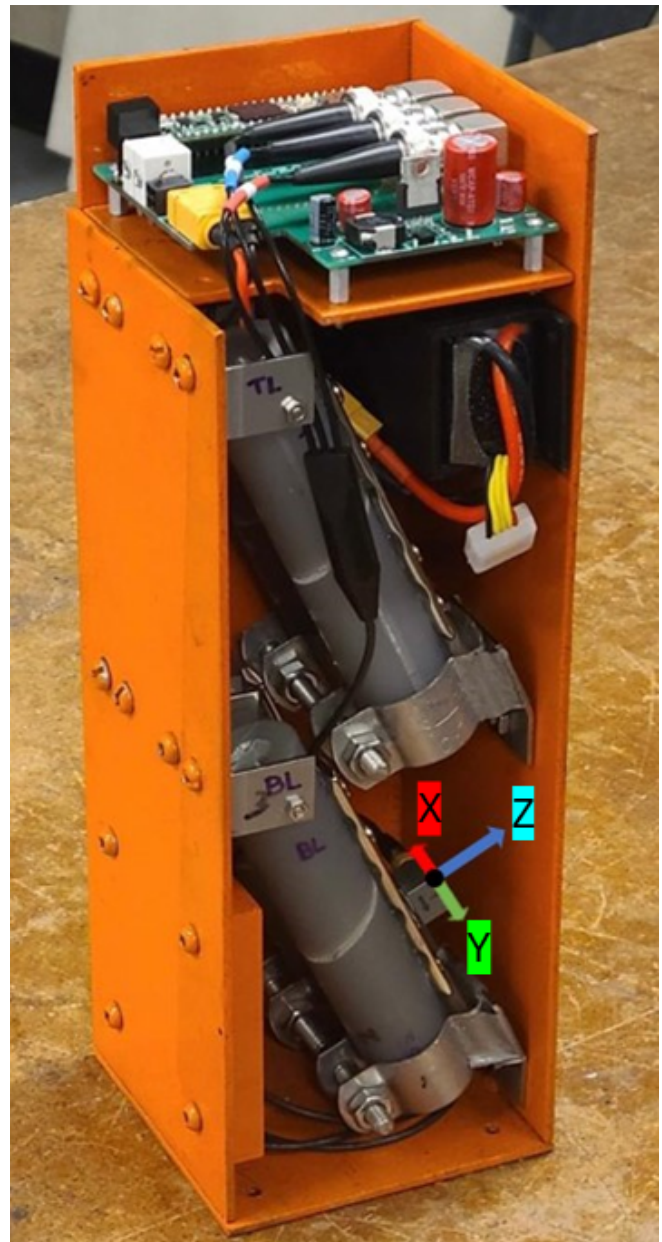


Figure 1. Finalized structure of the Payload with labelled x, y and z-axis of the Accelerometer where x-axis points into the bone, y-axis points along the DCP orthopedic plate and Z points in the direction perpendicular to the DCP orthopedic plate.

Force Model

A rocket environment demonstrates two distinct types of acceleration: dynamic and linear. Dynamic acceleration results from the vibrations and shaking of the rocket, whereas linear acceleration is generated by the upward thrust of the rocket. To have a comprehensive understanding of all the forces acting on the bone model, both dynamic and linear acceleration must be studied.

The top compartment of the Payload contained a student-developed Vibration Data Acquisition (DAQ) System (Figure 1). This custom Printed-Circuit Board (PCB) was used during the August 28, 2023 flight to acquire vibrations data by powering the 3 axial vibrational accelerometer and conditioning its output signal. The accelerometer was an Integrated Electronics Piezo-Electric (IEPE) sensor specifically suited for the aerospace industry, generously provided as a sponsorship by Hottinger Brüel Kjaer Inc. It specializes in accurately measuring dynamic acceleration and omits linear accelerations. As the PCB also contained a linear accelerometer, all acceleration types were measured.

Studying the vibration effects of the rocket environment on an orthopedic implant cannot be accurately replicated in a laboratory setting. Although there exist vibration testing equipment such as a shaker table, it has a set of limitations. NASA's space-grade shaker tests consist of a sinusoidal sweep test and a random vibration test. These tests create uniformly distributed vibrations to the device under test. However, in-flight conditions are harsher than simulated environments, and rockets are subject to forces of differing magnitudes¹⁴. Furthermore, shakers can only generate acceleration along a single axis at a time, whereas during flight, acceleration occurs in all degrees of freedom simultaneously. Perhaps the greatest limitation of a shaker test is its inability to properly simulate a shock event, a big burst in energy in a short amount of time. Shock events such as rocket engine fire or a stage separation are extremely common in rocket launches and correspond to events when mechanical stresses are extremely high.

Finite Element Model

Before performing the experiment by launching the rocket, the team used finite element analysis (FEA) to predict the effects of the different conditions in the rocket to help experimental design. When used correctly, FEA can identify areas of larger stress, deformation, and modes of vibration, providing preliminary knowledge to aid in experiment setup. A pre-launch analysis was also performed using FEA to confirm that the bone and plate assembly would not fail catastrophically under the loads experienced in the rocket. A set of hand calculations confirmed this. Using Siemens NX Nastran software, the team made several assumptions related to the material and the bone-plate assembly. In the initial computer model, the bolts connecting the bone and plate together were removed entirely and replaced with a gluing condition holding the plate to the bone, along with pinned conditions in the bolt holes. This simplification was feasible as the strength of the metal bolts far exceeded that of the bone, allowing them to be replaced with infinitely strong pins. This simplified the analysis, allowing us to create higher resolution and therefore more accurate results for stress concentrations in the bone. The fixed-pinned end conditions were modeled with a fixed constraint at one end and a pinned constraint at the other, which assumes the connections to the bone are rigid and frictionless. Once again, the designed metal fixtures to hold the bones at each end were far stronger than the bones themselves, so we did not expect significant deformation or damage in the end fixtures. The Sawbones models had a listed density of 1.64 g/cm^3 , Young's modulus of 16 GPa, and a Poisson's ratio of 0.26⁽¹²⁾. These were used to create a custom material in NX Nastran FEA, which remained the bone material throughout the analyses (Figure 2a).

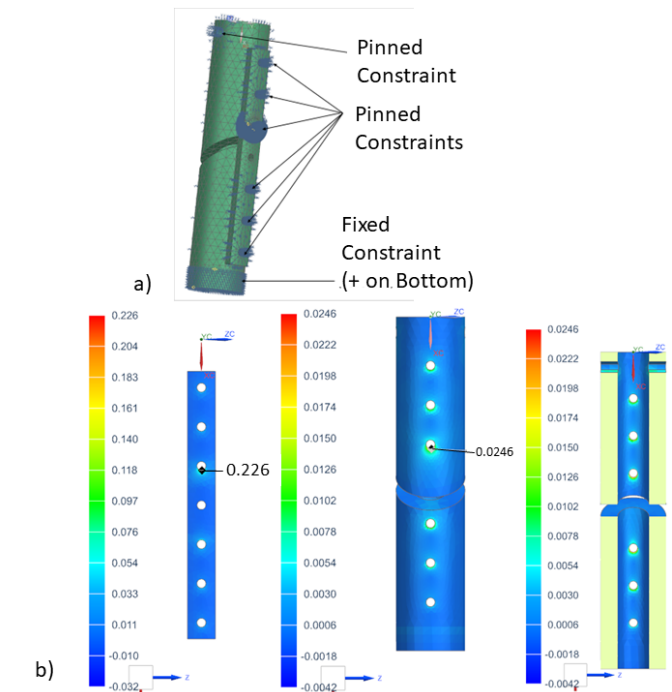


Figure 2. a) The meshed FEA model with all assumed constraints b) Results of the static FEA under launch conditions

Methods

Vibration Instrumentation

The Data Acquisition (DAQ) PCB measures the dynamic acceleration of the system. To optimize measurement accuracy, the DAQ PCB was calibrated according to the expected frequency and acceleration amplitude range. These parameters were obtained by testing the rocket engine, which is the main source of vibration. Through a series of engine tests, the team confidently assumed that all vibrations would range between 100 to 5000 Hz. These measurements correlated with what is observed by typical sounding rockets. The frequency range of the DAQ system was then limited, thus optimizing sampling precision and accuracy comparably with controlled vibration sources.

Finite Element Model Validation

The pre-launch analysis using FEA provided the team with insights into in-flight conditions. FEA involves making a computer model, with assumptions and simplifications as described in the previous section, that is then broken up into small mesh elements (meshed). In static analysis, the acceleration conditions of the rocket at both launch and parachute deployment are given to the program and applied to the elements. The program then outputs a coloured model displaying the stresses felt throughout the model. Viscoelasticity was not considered for our FEA model as the glass transition temperature was not made apparent by the supplier. Through iterative refinement of the mesh, we developed a static FEA model that applied a downward acceleration of 10 Gs and held the bones at 25°, which matched the experiment set-up. The results are shown in Figure 2b). The maximum in-plane stresses were 226 kPa and 24.6 kPa for the plate and bones, respectively. Both stresses were located around the hole directly above the fracture. These results are far below the yield stresses for the plate (275 MPa) and cortical bone (51.0 MPa). The same analysis was then repeated with the acceleration direction instead pointing up to simulate parachute deployment. With this change, similar stress values were calculated but the area of high stress was re-situated to the hole directly below the fracture.

Since the rocket's ascent subjects the bones to vibrations from the engine, we decided to conduct a normal modes vibration analysis. This analysis aimed to identify the natural frequencies of vibration and their corresponding mode shapes. The first ten modes of vibrations were between 1.182 kHz and 4.425 kHz, with shapes varying between longitudinal and torsional vibrations.

A limitation of this study is that it precludes damping. In reality, mode shapes are expected to be lower due to stress and deformation. However, this analysis does help identify areas of high stress, such as at the pin connection at the top of the bone (the knee-tibia interface), and the first four bolt holes closest to the fracture. These simulation results agree with solid mechanics theory, which states that stress tends to concentrate around holes or interruptions in 'stress flow'¹⁵.

Determination of Natural Frequency of Continuous Systems

The upper bound of the natural frequency of a continuous mass system can be approximated using Rayleigh's method as described below:

$$\omega_n^2 \leq \frac{\int_0^L EI \left(\frac{d^2 y}{dx^2} \right)^2 dx + \sum_{i=1}^n m_i y_i}{\int_0^L m y^2 dx + \sum_{i=1}^n m_i y_i^2}, \quad (1)$$

whereby ω_n is the natural angular velocity, m_i and m are the lump mass and continuous mass per unit length, E is the elastic modulus, I is the second moment of area, L is the length of the orthopedic plate, y_i is the static displacements induced by the lump masses, and $y = y(x)$ is the global shape function given by

$$y(x) = y_0(L^3 - 3Lx^2 + 2x^3) \quad (2)$$

for pin-fixed boundary conditions, whereby y_0 is a constant.

Preparing models and animal samples

Eight models were constructed, four healthy and four with osteopenia. Each model was 12.0 cm in length with an outer diameter of 27.0 mm. The healthy samples had an inner diameter of 13.0 mm and the samples with osteopenia had an inner diameter of 17.0 mm. This is because a 2.0 mm change in cortical thickness per side follows the estimated maximum decrease in cortical thickness observed for an ageing subject with no other health problems¹⁶. Two healthy samples and two samples with osteopenia were flown in the rocket and the remainder were used for control testing.

The fixation of the fractured bone segments was completed under the supervision of an orthopedic surgeon. A 1.3 mm fracture gap was maintained to further destabilize the interface. The two fragments were arranged such that they were separated by a 1.3 mm washer in a bench vise. Beginning with the center most hole, a 3.5 mm cobalt drill with a surgical drill guide was used to bore completely through both cortices. The 4.5 mm self-tapping screw was tightened using a hex screwdriver. This was repeated for the remaining holes. There was slight translation and torsion of the bone fragments during the first plating. To prevent downward translation of the second fragment, an upward force was applied to the bottom of the fragment while drilling. To prevent torsion of the plate, the vise was further tightened and the plate was clamped on both ends.

Post-Launch analysis

To assess the impact of the rocket launch on the bone segments post-launch, we subjected the flown samples and control samples to mechanical testing. During healing, bones are subjected to three major loading conditions: axial loading, bending, and torsion. Due to the seating orientation during ascent and descent, the tibia was assumed to be primarily subjected to bending.

Both samples were fixed at the ends, thereby minimizing motion in the x and y -axis. However, the pinned configuration imposed no moment along the bone axis that would have allowed for bending. As the leg is typically securely fastened during ascent and landing, torsion forces were assumed to be minimal.

The greatest changes in mechanical strength were therefore predicted to be in the bending modulus. The model's variation in strength was characterized by performing 3-point bend testing on the plate/fracture interface. The control models were tested before flight and the experimental models were tested after recovery.

In accordance with industrial conventions, the international standard of regulatory testing (ISO 178) was adapted for the purposes of biomechanical testing¹⁷. The flexural properties of rigid and semi-rigid materials during 3-point bending are detailed in ISO 178. The bending modulus was extracted from the stress strain curves and used to characterize the effects of the measured vibrations and forces.

Results

Launch Outcome

The results presented below were gathered using the Vibration Data Acquisition System described in the methods section above. The data presented is based on the 3-axis shown in Figure 1. Due to human mishandling, the z -axis connector was not properly connected. As a result, no vibration data was collected on that axis.

The 150-second flight contained three unique flight events: engine burn, drogue deployment, and landing. The results presented in the subsequent paragraph will focus on these engine burn event as a means of demonstrating the type of data collected.

Vibrational data can be presented in the time domain, the frequency domain, and spectrographically. The time domain representation is used for looking at a vibration, such as a shock event, over a small interval of time. Data can be observed in the frequency domain by plotting a Fast Fourier Transform (FFT), acquiring a broad overview of the vibration amplitude as a function of frequency. Viewing the data in the frequency domain allows us to understand the vibration profile of the rocket by highlighting the main frequency modes. Finally, the spectrogram is a series of FFTs over time. This data representation shows the evolution of the frequency response of the rocket over time. This is especially useful in a changing environment such as a rocket, where different mechanical phases are present. In the case of rockets, the frequency domain and spectrographic representations offer the best visuals of the vibrations.

The engine burn lasted roughly 20 seconds. The vibrations observed are up to 35 m/s² in the x -axis and up to 80 m/s² in the y -axis, with an overall range of 300–2750 Hz. It had a dominant mode of 1500 Hz and secondary modes (harmonics) at 500 Hz and 2500 Hz, thus confirming the frequency range assumptions made while calibrating the DAQ system. This data for the x -axis is conveyed in the frequency domain and spectrogram graphs which can be found in Figure 3 and 4, respectively.

Natural Frequency Calculation

Data was acquired through an accelerometer located at the midspan of the orthopedic plate on one of the four samples. The sample is assumed to be symmetric along the circumferential direction. Specifically, two time-series acceleration datasets were taken at the accelerometer location in the x and y directions, as depicted.

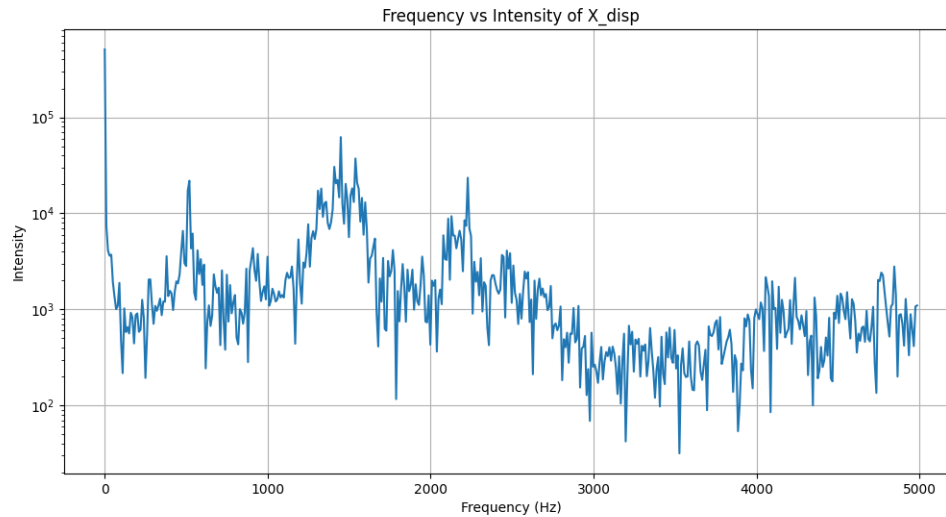


Figure 3. Frequency vs. Intensity graph of accelerometer data.

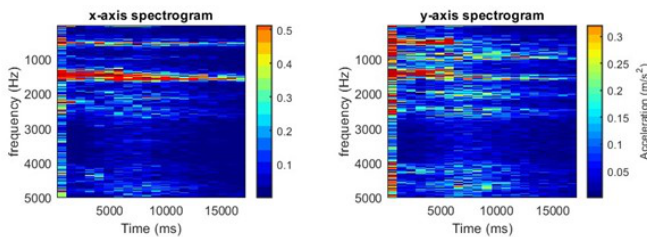


Figure 4. Spectrogram for engine burn for the x-axis (left) and y-axis (right).

Discussion

Model Evaluation

As observed in the bending results, the composite Sawbones models allowed for very precise results. The variability between trials was maximized at 30 MPa for the osteopenia-affected control samples, and minimized at 11 MPa for the osteopenia-affected test samples. This is much lower than was observed in the juvenile bovine samples, with a 96 MPa difference in the bending modulus between samples 1 and 2. The composite models were therefore ideal for the constraint of limited repeatability. The procedures for preparing the models are concluded to have been ideal for maximizing precision and use of space. However, the accuracy of the model was sacrificed by an oversimplification based on our limitations.

The lack of variance between the healthy samples and those with osteopenia indicates an issue with the model's evaluation of mechanical strength. Literature supports that bone density has significant impact on tibial mechanical strength¹⁸. Therefore, we conclude our method of three point bending was not an effective procedure for measuring mechanical strength. During testing, the stainless steel orthopedic plate yielded before the bone, meaning any deterioration that occurred in the bone itself was not measured.

Subsequently, the results between the flown and control models are invalidated. This could also be attributed to the bone model used. We hypothesize that neglecting the cancellous bone and focusing on the diaphyseal tibia was an oversimplification. The diaphyseal tibia is the strongest section of the bone with the most cortical tissue¹⁶. This section is therefore the most stable location for a screw fixation. Further work should analyse cancellous bones in sections with lower cortical composition like the epiphysis, where weakening is most likely. The results also implicate that macroscale analysis is not sufficient to understand the strength of the interface. This is supported by the FEA results which predicted minimal changes after flight. Small changes in compressive forces can have significant implications including induced apoptosis, increased resorption, reduced vascularization, and microfractures¹⁹. By analyzing cancellous bone on the microscale, small changes in compressive forces can be measured. The implications of these forces can be estimated in reference to existing literature.

The material we chose could also have affected the accuracy of the results.

Using the specifications of the healthy bone sample and the orthopedic plate, we obtain from Equations 1 and 2 an estimated upper limit for the first natural vibration angular velocity of $\omega_n \leq 2405.1$ rad/s or a natural frequency of $f_n \leq 382$ Hz.

Bend Testing

No significant difference was observed between the mean flexural strength of the flown and control samples. Further, no significant differences were observed between the mean flexural strength of the healthy samples versus those with osteopenia. However, the values measured for the juvenile bovine tibias had very high variability and were significantly lower than the composite samples (Table 1).

Table 1. Calculated Bending Modulus of the juvenile bovine samples, and the pre- and post- flight Sawbones samples.

Sample Type	Sample 1 (MPa)	Sample 2 (MPa)	Sample 3 (MPa)	Averaged Value (MPa)
Juvenile Bovine	123	219	167	169.7
Healthy Pre-Flight	298	276	-	287.0
Osteopenic Pre-Flight	244	277	-	260.5
Healthy Post-Flight	268	276	-	272.0
Osteopenic Post-Flight	283	294	-	288.5

The Sawbones composites accurately modelled the bulk of the mechanical properties of the cortical bone, but they were unable to represent microstructures and porosity. For analysis on the microscale, real bone internal geometries should be used to accurately represent the interaction with the screws. In the Sawbone model, the screw is completely engaged with the composite at all positions. In cortical bone, the porosity of the material would change the thread engagement. Using real bone samples can accurately represent this interaction.

The human model must also be re-evaluated. The assumption of a cylindrical structure negates the effects of stress concentrations. In reality, the tibia is not a perfect circle and the cortical thickness is not uniform. Stresses would not be uniformly distributed within the bone, allowing for failure modes in areas of high stress concentration.

We can also compare the FEA predictions from pre-flight to the observed forces during flight. From Figure 3, it can be seen that the FEA excitation frequency range of 1182 – 4425 Hz does not fully bind the accelerometer excitation frequency, meaning there was some error in approximating the first vibration mode. However, the dominant vibration frequency observed at 1500Hz was correctly identified. The FEA performed for vibration analysis can be further improved through the use of more accurate forcing conditions for the acceleration phase, as well as the use of other deformable solid models that more closely resemble our orthopedic sample.

The observed frequency dominant vibration frequency is significantly higher than the theoretical natural frequency from Equation 1, of the first mode of 382 Hz. This suggests that the operating frequency range with external forcing from acceleration does not instill any resonance phenomena. Forced vibration analysis FEAs can be performed in future works in reference to the accelerometer data and the discovered excitation frequencies.

Limitations and future work

As a pilot study, LOVE provided insight into quantifying the effects of spaceflight forces and vibrations on the stability of orthopedic implants. Using the lessons learned from this study, the payload team will implement a microscale analysis on screw insertions in cancellous bone in next year's payload. Further, the vibration profile collected from the first flight will allow predictive analysis using FEA to estimate the effects of the launch on next year's model.

Acknowledgments

Writing this paper would not have been possible without all the talented students in the McGill Rocket Team who succeeded in launching and recovering a rocket, a first for all who were involved. A special thank you to the Payload subteam for bringing LOVE to life, as well as to all our advisors and sponsors who supported us throughout the journey: Thank you to Dr. Peter Glavas for sharing your expertise in orthopedics, as well as to Dr. Ahmed Aoude and Dr. Emily Newell for your valuable feedback. We are grateful to Nikita Letov & Lucie Riffard for providing testing equipment, to Thom Porro from Sawbones and Jonathan Trottier from Synthes for sponsoring important materials.

References

- Davidian, K. Space Tourism Industry Emergence: Description and Data. *New Space* **8**, 87–102 (2022). <https://doi.org/10.1089/space.2019.0040>
- Huh, J. & Kwon, S. A practical design approach for a single-stage sounding rocket to reach a target altitude. *Aeronaut. J.* **126**, 1084–1100 (2022). <https://doi.org/10.1017/aer.2022.18>
- Nicholson, J., Makaram, N., Simpson, A. & Keating, J. Fracture nonunion in long bones: A literature review of risk factors and surgical management. *Injury* **52**, S3–S11 (2021). <https://doi.org/10.1016/j.injury.2020.11.029>
- Genah, S., Monici, M. & Morbidelli, L. The Effect of Space Travel on Bone Metabolism: Considerations on Today's Major Challenges and Advances in Pharmacology. *J. Mol. Sci.* **22**, 4585 (2021). <https://doi.org/10.3390/ijms22094585>
- Hadjikidakis, D. J. Bone Remodeling. *Ann. N. Y. Acad. Sci.* **96**, 385–396 (2006). <https://doi.org/10.1196/annals.1365.035>
- Ott, S. M. Cortical or Trabecular Bone: What's the Difference? *Am. J. Nephrol.* **47**, 373–375 (2018). <https://doi.org/10.1159/000489672>
- Madadi, F. Adult tibial shaft fractures – different patterns, various treatments and complications. *Med. Sci. Monit.* **17**, 640–645 (2011). <https://doi.org/10.12659/msm.882049>
- The Royal Children's Hospital Melbourne. Clinical Practice Guidelines: Tibial shaft (diaphyseal) fracture — Emergency Department; https://www.rch.org.au/clinicalguide/guideline_index/fractures/tibial_shaft_emergency/
- Isogai, K. et al. Young's moduli of subcutaneous tissues and muscles under different loads at the gluteal region calculated using ultrasonography. *J. Phys. Ther. Sci.* **34**, 777–783 (2022). <https://doi.org/10.1589/jpts.34.777>
- Jovanovic, S. Applicability of bovine tibia as a model in research on various osteosynthesis techniques. *Period. Biol.* **112**, 59–62 (2010).
- Li, Z., Wang, Q. & Liu, G. A Review of 3D Printed Bone Implants. *Micromachines* **13**, 528 (2022). <https://doi.org/10.3390/mi13040528>
- Pacific Research Laboratory. Biomechanical Materials for Testing and Validation (2023); <https://www.sawbones.com/biomechanical-product-info>
- Blue Origin. New Shepard (2023); <https://www.blueorigin.com/new-shepard>
- Sarafin, T. *Vibration Testing of Small Satellites* tech. rep. (Instar Engineering and Consulting, Inc., 2017). https://s3vi.ndc.nasa.gov/ssri-kb/static/resources/Instar_Vibration_Testing.pdf
- Beer, F. P., Johnston Jr, E. R., DeWolf, J. T. & Mazurek, D. F. *Mechanics of Materials* (McGraw-Hill Education, 2020).
- Maeda, K. Cortical thickness of the tibial diaphysis reveals age- and sex-related characteristics between non-obese healthy young and elderly subjects depending on the tibial regions. *J. Exp. Orthop.* **7**, 1–11 (2020). <https://doi.org/10.1159/000489672>
- International Organization for Standardization. Determination of Flexural Properties, Plastics (2019); <https://www.iso.org/obp/ui/es/#iso:std:iso:178:ed-6:v:1:en>
- Deckard, C. Using three-point bending to evaluate tibia bone strength in ovariectomized young mice. *J. Biol. Phys.* **43**, 139–148 (2017). <https://doi.org/10.1007/s10867-016-9439-y>
- Norton, M. Bone glue – The final frontier for fracture repair and implantable device stabilization. *Int. J. Adhes. Adhes.* **102**, 102647 (2020). <https://doi.org/10.1016/j.ijadhadh.2020.102647>

¹School of Physics, University of Bristol, Bristol, United Kingdom

Keywords

Accretion discs, black holes, thick discs, accretion flows

Email Correspondence

zo20222@bristol.ac.uk

<https://doi.org/10.26443/msurj.v19i1.229>

©The Authors. This article is published under a CC-BY license: <https://creativecommons.org/licenses/by/4.0/>

Wiktorja Tarnopolska¹

Properties of Accretion Discs Around Black Holes through Modelling

Abstract

We examine accretion discs within the context of Einstein's general relativity. We use the metrics corresponding to the four black hole solutions proposed by Einstein, with the Shakura-Sunyaev model of the disc. Starting from the definition of the "no-hair theorem" that a black hole only stores information about three main parameters — mass, angular momentum and charge — we tested the impact of varying these parameters, emphasising the relations between them. Moreover, the research we present here captures and illustrates two pivotal aspects predicted by general relativity: the circular photon ring and the frame-dragging effects of the ergosphere. Our research delves into emissivity profiles, exploring both the well-established lamp post model and the beamed point source model. We reproduced the results from the literature and noted the inconsistencies between the works and our results while also providing an alternative source supporting our results. Altogether, this work presents a comprehensive exploration of accretion disc dynamics around central compact objects within the framework of Einstein's general relativity, shedding light on intricate phenomena that continue to captivate the scientific community.

Introduction

Black holes, with their unparalleled gravitational force, stand as some of the most enigmatic objects in the Universe. Their intense gravitational pull has made it challenging to scrutinize them through direct observation. It was not until 2019 that the groundbreaking work of the Event Horizon Telescope provided the first visual confirmation of a black hole's existence in the Messier 87 galaxy¹. Nevertheless, the theoretical groundwork for black holes had been laid long before, rooted in mathematical and theoretical models that predicted their existence.

The currently prevailing belief, resulting from work in the late 20th century, is that dense star clusters and massive stars have an almost inexorable destiny of collapsing into black holes. This hypothesis suggests the likely existence of supermassive black holes at the cores of galaxies, especially if they have been active². Beyond their role in cosmic architecture, black holes serve as astonishingly efficient power sources. Accretion onto a black hole stands as the most efficient process known for emitting energy. Of particular note are Kerr rotating black holes, renowned for their exceptional power. Accretion onto a Kerr black hole is actually the most efficient process in the Universe, with efficiency 0.426 for a maximally rotating black hole in the Kerr metric³.

Methods

`Gradus.jl`⁴ is a novel photon ray tracing code authored by Baker & Young (2022) and proves to be an essential tool in black hole modelling. This software enables a range of numerical simulations, with a primary focus on exploring various accretion disc scenarios. We used a new photon integration code to investigate photon orbits around the black holes, since the `Gradus` code allows arbitrary spacetime metrics to be used in a straightfor-

ward manner. We focused on the four distinct black holes solutions arising from general relativity, with particular emphasis on Kerr, Kerr-Newman, and Reissner-Nordstrom metrics. These simulations provided a platform for testing the "no-hair theorem" by testing the effects of varying the three black hole parameters — mass M , angular momentum J and charge Q — predicted by the theorem to be the only information characterising a black hole. We used point-source ray tracing, and reconfigured the present lamp post model to represent a flare within the accretion disc. This enabled investigation of how photon trajectories are influenced by the presence of singularities in different metrics.

Furthermore, by using and modifying `Gradus.jl`, we simulated emissivity profiles both for a stationary and a beamed point source, as well as line profiles for black holes of varying spin and charge parameters.

Testing the No-Hair Theorem

In 1972, Jacob Bekenstein first introduced the "no-hair theorem," a concept later revised in 1995. This theory postulates that black holes possess minimal characteristics, encompassing only three fundamental components: mass M , angular momentum J , and charge Q . Remarkably, John A. Wheeler, who famously coined the term "black hole," drew upon Bekenstein's "no-hair" concept to propose an intriguing notion. Wheeler suggested that if two black holes shared identical values of momentum, charge, and mass, yet one was composed of matter while the other consisted of antimatter, they would be indistinguishable, as outlined in his work⁵.

The intriguing consequence of the no-hair theorem's violation is the disruption of symmetry, leading to the transformation of the photon ring's shape. Johannsen & Psaltis⁶ state that the degree of asymmetry is a direct measure of the violation of the "no-hair theorem." Furthermore, research conducted

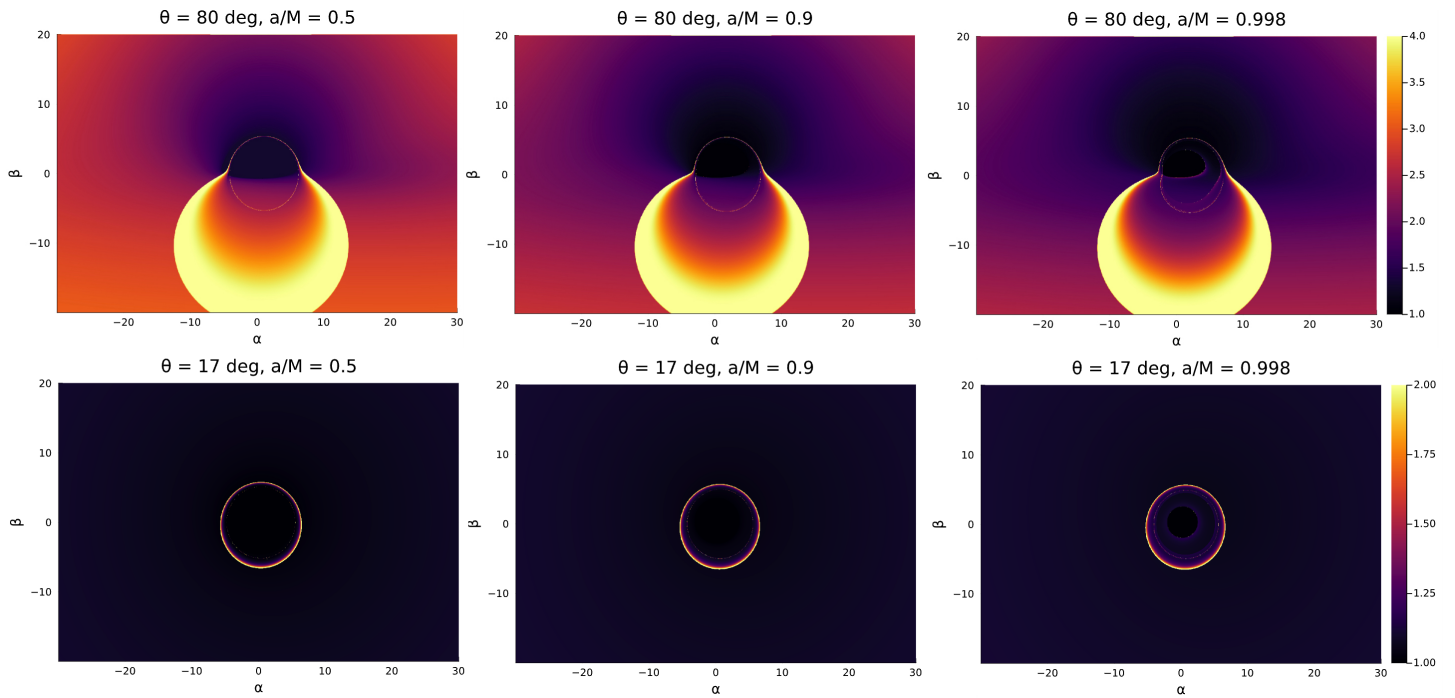


Figure 1. Effects of varying the a/M ratio for a rotating Kerr black hole, increased from left to right, with α and β representing the impact parameters. The first row shows the black hole as viewed from an inclination angle of 80° and the row below with the observer at an inclination angle of 17° . The shape of the photon ring becomes increasingly asymmetric and offset from the origin, remaining almost circular for $a \leq 0.9M$ and losing the circular shape for a rapidly rotating black hole at $a/M = 0.998$.

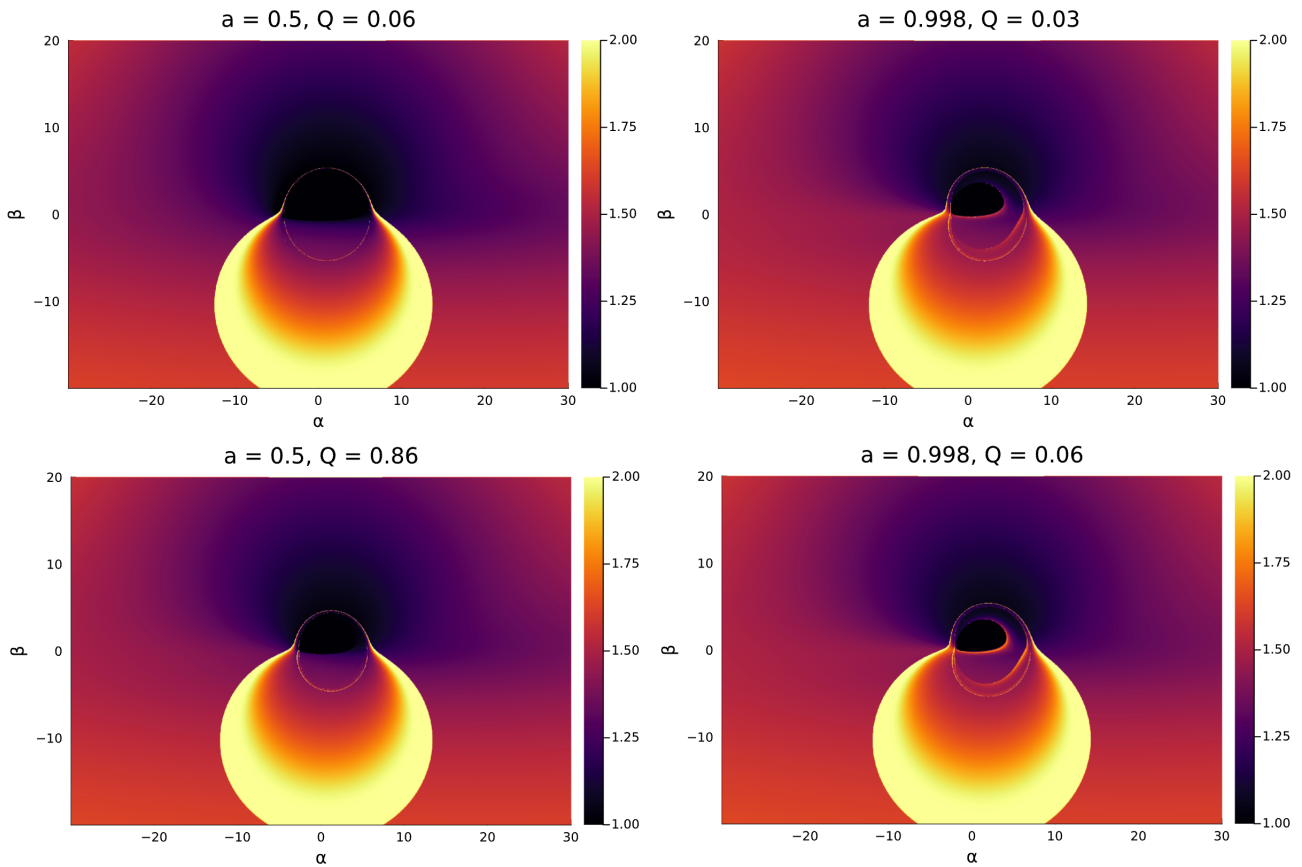


Figure 2. Results of varying charge for black holes in the Kerr–Newman metric with spin $a/M = 0.5$ (left) and $a/M = 0.998$ (right). Deformation of the photon ring is observed as the charge is increased for the $a = 0.5$ case while for the rapidly rotating $a = 0.998$ black hole, increased radiative transfer is observed “inside” the photon ring.

by Bambi & Freese⁷ explored the possibility of using the black hole images to test if black holes with $a \leq M$ violate the “no-hair theorem,” depending on whether general relativity remains valid in this strong field regime. Specifically, in the case of a Schwarzschild non-rotating black hole, the photon ring becomes elliptical. For a rotating Kerr black hole, this asymmetry becomes even more pronounced, as detailed by the research conducted by Johannsen & Psaltis⁶. Using the computational capabilities of `Gradus.jl`, we validated these findings. Our investigation demonstrates that, within the Kerr metric framework, the ring remains virtually circular for values of spin $a \leq 0.9M$, where $a = J/M$ with increased asymmetry observed at higher values.

While the Kerr metric serves as the spinning extension of the Schwarzschild solution, the Kerr-Newman spinning-charged solution represents both a charged generalization of the Kerr metric and a spinning counterpart to the Reissner-Nordstrom solution. Collectively, these four metrics constitute the cornerstone of the black hole solutions of general relativity⁸.

Results

Kerr metric

The Kerr metric serves as a spinning generalization of the Schwarzschild solution⁹. Within the framework of the Kerr metric, Figure 1 illustrates the effects stemming from variations in the spin-to-mass ratio (a/M) from the vantage points of two distinct observers. In Figures 1, 2, 3, the colours correspond to energy flux and the parameters α and β span the grid of the impact parameters and each pixel on the grid is coloured in the units proportional to units of intensity. As pointed out by Johannsen & Psaltis, as the a/M ratio is increased, the photon ring’s symmetry diminishes. Upon reaching the maximum spin value of $a = 0.998$, the once-circular photon ring undergoes a significant transformation, becoming highly asymmetric and displaced from its original position. This transformation is a consequence of the black hole’s ability to warp spacetime and induce frame-dragging, a phenomenon that occurs within the ergosphere of a black hole. This characteristic feature is described by the Kerr and Kerr–Newman metrics, which pertain to rotating black holes¹⁰.

Kerr–Newman metric

The Kerr-Newman metric introduces a charge parameter Q into the description of a rotating black hole with non-zero spin. This mathematical framework captures the intricate interaction between gravitational and electromagnetic fields emanating from a rotating mass with an electric charge distributed along its axis of symmetry. Notably, the Kerr-Newman metric characterizes a rotating mass endowed with an electric charge, an extension originally crafted by Newman et al. in 1965¹¹, thereby arguing for the existence of the broader Kerr family of solutions.

It is worth noting that in astrophysical contexts, the electric charge of black holes is typically considered negligible. However, despite its minor role in natural astrophysical scenarios, accounting for electric charge remains valuable in theoretical modelling. Charge possessed by a black hole can still impact charged particles in the disc.

Plots were generated to illustrate four scenarios involving a charged rotating black hole within the Kerr–Newman metric framework. Two where $a/M = 0.5$, with values of Q set to 0.06 and 0.86 and two of a rapidly rotating black hole with $a/M = 0.998$ and charge 0.03 and 0.06 as depicted in Figure 2. Analogous to the scenario in the Kerr metric, these plots reveal frame dragging within the ergosphere and a distortion in the circular shape of the photon ring.

It is important to note the constraint

$$a^2 + Q^2 \leq M^2 \quad (1)$$

where equality holds for the extremal black hole¹², which originates from the Kerr solution itself. This condition ensures that the black hole’s properties remain consistent with the underlying spacetime geometry. Taking this constraint into account, for a black hole with a spin parameter of $a = 0.5$, the maximum permissible charge is approximately $Q = 0.86$, while for a rapidly rotating black hole with $a = 0.998$, the maximum charge decreases significantly to around $Q = 0.06$.

Reissner–Nordström metric

Reissner–Nordström introduces the charge parameter Q as a specific instance of the Kerr–Newman metric. According to Misner¹³, all static (i.e. non-rotating) black holes are distinctly defined by the parameters M and Q , and they exhibit the Reissner–Nordström form. The charged generalization of the Schwarzschild solution was independently uncovered by Reissner (1916) and Nordström (1918)¹¹. There are no other existing solutions for stationary black holes.

The formula for the black hole shadow size as a function of its charge was derived in Zakharov¹⁴ as

$$D = -512 \cdot \left(Q - \frac{9}{8}\right)^3 \quad (2)$$

where D is the shadow diameter and Q is the charge in units of mass M .

We created a black hole in Reissner–Nordström metric (Figure 3) and varied the charge to examine how the appearance of a black hole depends on Q . As predicted from the formula in the Equation 2, as the charge is increased, the diameter of the shadow decreases.

Point Source Ray Tracing

`Gradus` can simulate various corona models, including the lamp post model. By adapting the code to this model, we scrutinized the behavior of photons and their trajectories as if they emanated from an isotropic point source, and traced their paths to the accretion disc. Ray tracing is emerging as a powerful tool. Specifically, it facilitates the generation of images at remarkably high resolutions, allowing for a detailed examination of the substructure within the photon ring, as well as the influence of turbulence. The distinctive properties of photon subrings can be investigated¹⁵ by employing an adaptive scheme and subring decomposition.

The results obtained from tracing these photon paths provide valuable insights into how altering the spin parameter (a) changes the behavior of black holes and the nearby photon paths. Notably, as the spin increases, the event horizon’s diameter decreases in the Kerr metric. Despite the fact that the faster rotation of the black hole induces greater spacetime curvature due to frame-dragging (as illustrated in Figure 4), we observed photon paths to be less bent by a black hole with a smaller diameter, while the distance of the flare from the singularity remained constant. This phenomenon is attributed to the decreasing innermost stable circular orbit (ISCO) with increasing spin, which causes the photon orbit’s radius to be smaller than that of a Schwarzschild black hole. In the latter case, the ISCO can be found at approximately three times the Schwarzschild radius ($3r_s$) before spiraling beyond the event horizon.

Emissivity Profiles

The corona is situated above the black hole and continuously emits X-rays that subsequently illuminate the accretion disc. This process generates a

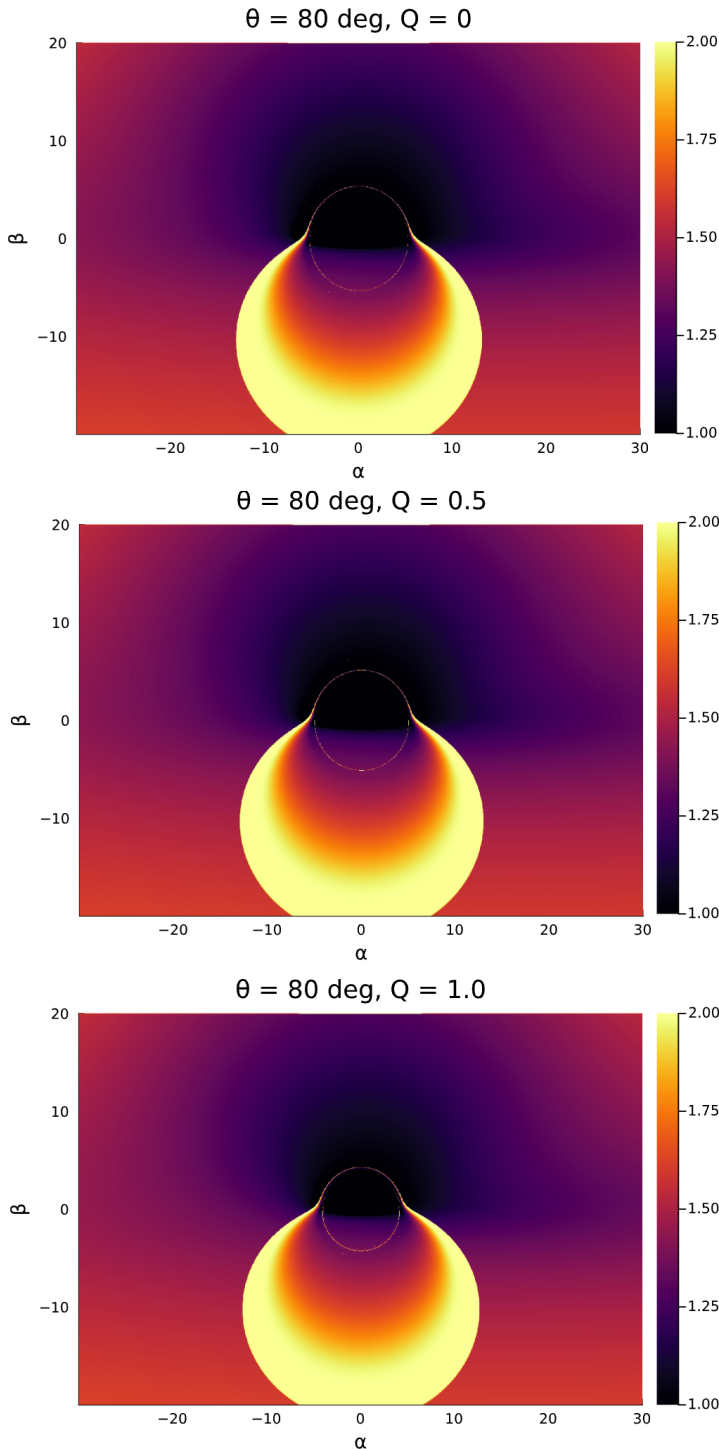


Figure 3. Energy flux of the Reissner–Nordström black hole with charge varied between 0 and 1. The first image at the top is the case of vanishing charge which, combined with absence of spin, illustrates the Schwarzschild metric for comparison. The results imply that the black hole shadow diameter decreases when charge Q is increased, which is consistent with literature.

discernible pattern interpreted as the emissivity profile. This profile depends on various factors, including the precise location and geometry of the X-ray source, as well as the characteristics of the accretion disc¹⁶.

Using the Gradus tool, we replicated models proposed by Gonzalez et al. in 2017¹⁷. Our objective was to discern how the emissivity profile relies on parameters such as the height above the black hole, the displacement axis, and the photon index within the lamp post model. Furthermore, we

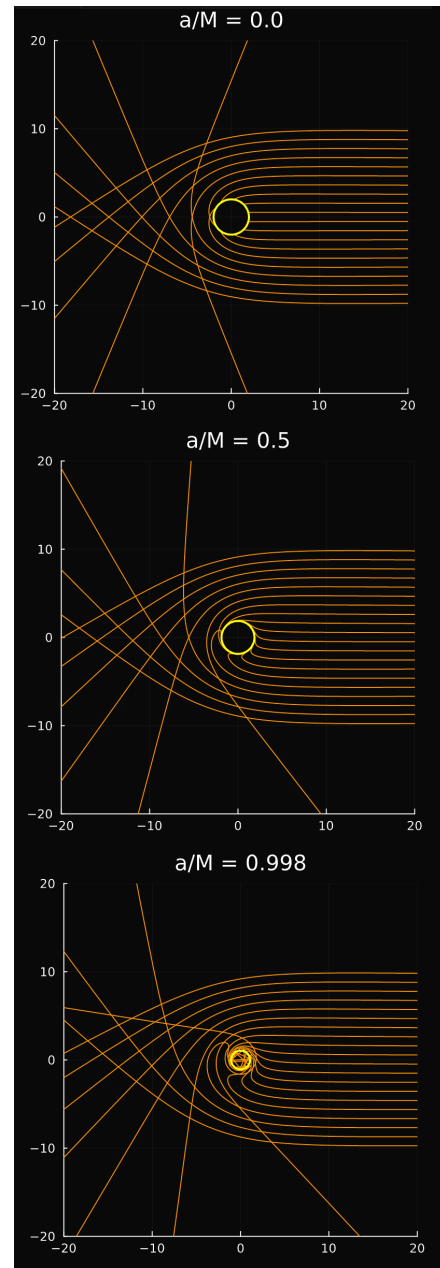


Figure 4. Frame dragging can be observed around rotating black holes, making a significant difference compared to a Schwarzschild black hole with $a/M = 0$.

examined insights from Dauser et al. 2013¹⁸ on beamed point sources.

Results

Stationary lamp post

We simulated a Kerr black hole with a spin parameter of $a = 0.998$, representing the maximally rotating case. We employed the lamp post model to emulate the corona.

We systematically varied the height h of the radiation source within the range of 2.5 to 20 Schwarzschild radii, as illustrated in Figure 5. In the case of low resolution, which manifests as irregularities in the line plots, increasing the number of samples should resolve the issue, albeit at the cost of greater computation time. The results are consistent with existing literature findings^{17,19}. Notably, the steepest slope in the observed emissivity profile

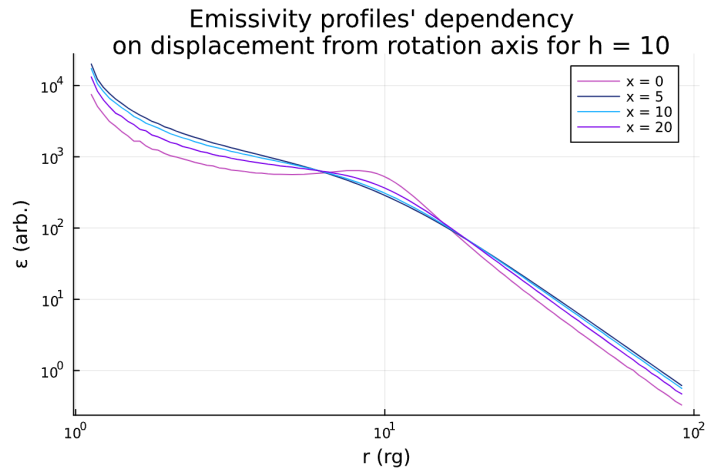
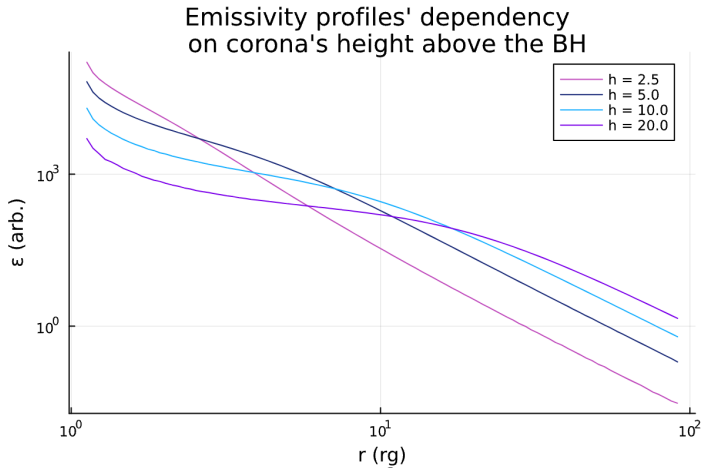


Figure 5. Results of varying corona's height (left) and displacement from rotation axis (right) above the black hole and accretion disc. First plot becomes more steep as the height is increased and the second shows that largest number of photons land under the source since as the corona is displaced from the rotation axis, outer disc receives more photons than the innermost parts and therefore becomes more illuminated.

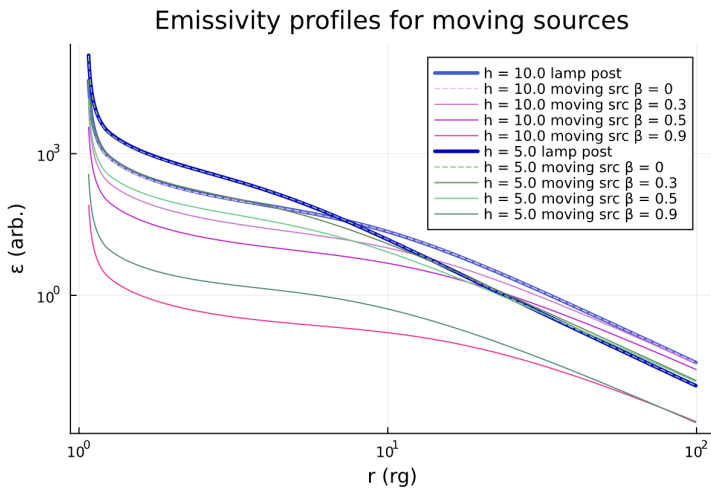


Figure 6. Emissivity profiles for sources at heights $h = 5$ and $h = 10$ with varying velocity of the jet base β . Includes 'tests' by comparing a stationary lamp post (blue) with a beamed source models with $\beta = 0$ (dashed) to show that the beamed point source model satisfies the predictions and to prove its correctness and consistency within the software as a whole.

corresponds to the source positioned closest to the black hole ($h = 2.5$ Schwarzschild radii). As the source distance increases, a diminishing slope is observed due to time dilation effects that enhance the flux of photons reaching the innermost region of the accretion disc¹⁷.

Furthermore, the displacement of the radiation source from the rotation axis also influences the emissivity profile, as depicted in Figure 5. Axisymmetric system implies a disk-like of ring-shaped corona. Novel models provided within *Gradus.jl* calculate emissivity profiles in two-dimensional space on the disc, allowing us to analyse non-axisymmetric systems. Using the Voronoi decomposition of the disc, the profile is calculated and in the limit of large sample points approaches the true emissivity function. This displacement accentuates the discontinuity in the plot as it increases. The reason behind this behavior is that as the source moves away from the innermost section of the accretion disc, the outer regions become increasingly illuminated, with more photons impinging upon the disc beneath the source¹⁷.

Beamed point source

Aside from stationary sources as found in the stationary lamp model, beamed sources play a crucial role, particularly in active galactic nuclei (AGN) exhibiting jet-like structures or outflows. Given that point sources are among the most likely candidates to exhibit beaming effects, we formulated a model of a beamed point source. The corona begins at a designated height h and can subsequently be projected upward with a velocity β (note: not the impact parameter as before). To simulate this model, we modified the *Gradus* code. We introduced a new datatype that enables the specification of a corona that dynamically moves away from the vicinity of the black hole. This feature has now been successfully implemented within the software.

However, the results obtained from the beamed source (Figure 6) do not align with those reported in literature^{17,19}. Furthermore, when examining the moving source plots in Fig. 6(c) in Gonzalez et al. (2017)¹⁷, and Fig. 11 in Wilkins et al. (2012)¹⁹, the two datasets do not agree either, despite the sole variation being the height of the corona.

Gonzalez et al. report that a sudden drop is observed in emissivity over the middle region of the disc due to relativistic effects caused by the beamed source¹⁷. The same was not reported by Wilkins et al.¹⁹. Wilkins et al. do not describe in detail their method for calculating these beamed point source emissivities¹⁹. On the other hand, the tetrad calculation by Gonzalez et al. is consistent with the one implemented in *Gradus.jl*, and the local momenta are consistent with Wilkins et al. However, the outcomes presented in Figure 6 ultimately agree with those reported in Fig. 6(a) of Dauser et al. (2013)¹⁸. The trends we observed are consistent and the quantitative comparison will be performed in the future. As the height of the jet base increases, the plot shifts downward, and with an increase in velocity, it becomes less steep. This suggests that the photon flux diminishes with higher speeds, as photons are propelled away from the accretion disc.

Conclusion

In conclusion, employing powerful computational tools such as *Gradus.jl*, yielded profound insights into the behaviour of black holes and their interaction with the spacetime and photons. Through intricate simulations based on established metrics such as Kerr, Kerr-Newman, and Reissner-Nordström, the study has not only validated key theoretical predictions but also expanded the understanding of these objects and the

results coming from the environment they create.

The definition of the “no-hair theorem” states that a black hole only stores information about three parameters — mass, angular momentum and charge. The impact of varying these parameters on the photon ring’s shape, as demonstrated through simulations, emphasises the relations between the three black hole parameters.

The application of point-source ray tracing allowed us to observe and justify the intricate behaviour of photons in close proximity of black holes. Moreover, the study of emissivity profiles, both from stationary and beamed point sources, has provided valuable insights into the intricate dynamics of accretion flows.

Navigating through the implications of black holes parameters such as height, displacement, and velocity in the simulations, the significance of the versatility of tools like `Gradus.jl` becomes apparent. Computational simulations notably serve as a bridge connecting theoretical predictions with observable phenomena, offering a unique way of analysing black holes in diverse astrophysical contexts.

Acknowledgements

In this article, I would like to specifically honour the memory of my beloved Grandfather, Zbigniew Komorowski, who passed away in October of 2022. He was a great man without whom I would not be where I am today and I will always be grateful for his support, love and sharing his passion for science. I am honoured to be able to celebrate his memory in this beautiful way.

Special thanks to Professor Andrew Young for his help and guidance, feedback and supervision of this project. Extending my sincere thanks to Fergus Baker, the mind behind `Gradus`, for countless code checks, support and collaboration during my work.

I would like to express my deep gratitude for a grant from the Royal Astronomical Society that financed my research this summer alongside funding from the University of Bristol.

References

1. Akiyama, K. et al. First M87 event horizon telescope results. IV. Imaging the central supermassive black hole. *Astrophys. J. Lett.* **875**, L4 (2019). <https://doi.org/10.3847/2041-8213/ab0e85>
2. Rees, M. J. Black hole models for active galactic nuclei. *Annu. Rev. Astron. Astrophys.* **22**, 471–506 (1984). <https://doi.org/10.1146/annurev.aa.22.090184.002351>
3. Choudhury, M. Black Holes and the Scientific Process. Preprint at <https://doi.org/10.48550/arXiv.1506.01957> (2015).
4. Baker, F. & Young, A. *Gradus.jl* version 0.1.0. 2022. <https://doi.org/10.5281/zenodo.6471796>.
5. Ruffini, R. & Wheeler, J. A. Introducing the black hole. *Phys. Today* **24**, 30–41 (1971). <http://dx.doi.org/10.1063/1.3022513>
6. Johannsen, T. & Psaltis, D. Testing the no-hair theorem with observations in the electromagnetic spectrum. II. Black hole images. *Astrophys. J.* **718**, 446–454 (2010). <https://doi.org/10.1088/0004-637X/718/1/446>
7. Bambi, C. & Freese, K. Apparent shape of super-spinning black holes. *Phys. Rev.* **79**, 043002 (2009). <https://doi.org/10.1103/PhysRevD.79.043002>
8. Adamo, T. & Newman, E. T. The Kerr-Newman metric: A Review. *Scholarpedia* **9**, 31791 (2014). <https://doi.org/10.4249/scholarpedia.31791>
9. Kerr, R. P. Gravitational field of a spinning mass as an example of algebraically special metrics. *Phys. Rev. Lett.* **11**, 237–238 (1963). <https://doi.org/10.1103/PhysRevLett.11.237>
10. Wex, N. & Kopeikin, S. M. Frame dragging and other precessional effects in black hole pulsar binaries. *Astrophys. J.* **514**, 388 (1999). <http://dx.doi.org/10.1086/306933>
11. Wald, R. M. *General Relativity* chap. 8 (University of Chicago Press, 1984).
12. Liu, C. Q. Collision of two general geodesic particles around a Kerr–Newman black hole. *Chin. J. Phys.* **30**, 100401 (2013). <https://doi.org/10.1088/0256-307X/30/10/100401>
13. Misner, C. W., Thorne, K. S. & Wheeler, J. A. *Gravitation* chap. 33 (W. H. Freeman and Company, 1973).
14. Zakharov, A. F. Constraints on a charge in the Reissner–Nordström metric for the black hole at the Galactic Center. *Phys. Rev.* **90**, 062007 (2014). <https://doi.org/10.1103/PhysRevD.90.062007>
15. Gelles, Z. et al. The Role of Adaptive Ray Tracing in Analyzing Black Hole Structure. *Astrophys. J.* **912**, 39 (2021). <http://dx.doi.org/10.3847/1538-4357/abee131>
16. Wilkins, D. R. & Fabian, A. C. Determination of the X-ray reflection emissivity profile of 1H 0707–495. *Mon. Not. R. Astron. Soc.* **414**, 1269–1277 (2011). <http://dx.doi.org/10.1111/j.1365-2966.2011.18458.x>
17. Gonzalez, A. G. et al. Probing the geometry and motion of AGN coronae through accretion disc emissivity profiles. *Mon. Not. R. Astron. Soc.* **472**, 1932–1945 (2017). <http://dx.doi.org/10.1093/mnras/stx2080>
18. Dauser, T. et al. Irradiation of an Accretion Disc by a Jet: General Properties and Implications for Spin Measurements of Black Holes. *Mon. Not. R. Astron. Soc.* **430**, 1694–1708 (2013). <http://dx.doi.org/10.1093/mnras/sts710>
19. Wilkins, D. R. & Fabian, A. C. Understanding X-ray reflection emissivity profiles in AGN: locating the X-ray source. *Mon. Not. R. Astron. Soc.* **424**, 1284–1296 (2012). <http://dx.doi.org/10.1111/j.1365-2966.2012.21308.x>

Research Article

¹Department of Physics,
McGill University, Montréal,
QC, Canada

Keywords

Oceanic sonar, climate change,
underwater acoustics

Email Correspondence

abigail.farkas@mail.mcgill.ca

<https://doi.org/10.26443/msurj.v19i1.203>

©The Authors. This article is
published under a CC-BY license:
<https://creativecommons.org/licenses/by/4.0/>

Abigail Farkas¹

The Effects of Climate Change on Oceanic Sonar Use in the Upper European Continental Shelf

Abstract

As the global effects of climate change become more known year by year, it becomes ever-more pertinent to examine the effects this may bring for every aspect of modern life we rely on. One topic of focus is that of multi-frequency sonar communication and navigational systems, which rely on well-established relationships relating to wave speed, signal intensity, and attenuation. We compiled data on oceanic temperature, acidity, and salinity in the Upper European Shelf, which includes the North Sea and Mediterranean Sea, from 2006 to 2072 using the CMIP5 future climate model in the RCP8.5 scenario. We calculate that the speed of sound in the northern European oceanic area will decrease by almost 18 m/s by 2072, with an average yearly decrease in sound speed by 0.37 m/s. The attenuation of sound through water will change year by year, calculated based on a higher-order polynomial regression dependent on the frequency of sonar used. The maximum operating ranges of active low-frequency, mid-frequency, and high-frequency sonar systems would theoretically change by +0.06%, -0.19%, and +0.71%, respectively per year, if no other factors are affected. Due to increased sound propagation, the ambient noise level of the ocean would also increase and have some counter-effect to the increased detection range however that increase in noise level was not quantitatively analyzed in this study.

Introduction

Multi-frequency sonar communication and navigational systems depend on being properly calibrated to the acoustical properties of the environment in which the sonar system is used. Rising global temperatures and other long-term changes in oceanic biomarkers may have a notable effect on the accuracy and effectiveness of these systems, and so analysis is required to determine the potential significance of these impacts and open a discussion into the topic.

Nautical navigational systems use either active or passive sonar in order to map their surroundings, locate marine life, or locate and communicate with other vessels at sea. Signal pulses from sonar systems can have a set frequency anywhere in the 1–200 kHz range, because different frequencies have different resolutions and can serve these various purposes better.

Active sonar consists of sending out these signal pulses, then listening for the returned signal that was reflected off of nearby vessels, sea life, or the ocean floor, and calculating the distance d based on the time t between the sent signal and the received reflection using the equation $d = \frac{t \cdot c}{2}$ where c is the speed of sound in m/s.

Passive sonar is quite different, where the system only listens for any incoming acoustic signals emitted from any sources of interest with an array of sensors. Determining the distance from the vessel to the detected source employs a model of non-linear equations based on the differences in detection time at each sensor in the array. Passive sonar systems are less sensitive to changes in speed of sound, and so this analysis only pertains to active sonar.

A simplified 3rd order polynomial equation for the speed of sound under-water is given by Medwin (1975)¹:

$$c \text{ (m/s)} = 1449.2 + 4.6T - 0.055T^2 + 0.00029T^3 + (1.34 - 0.010T)(S - 35) + 0.016D, \quad (1)$$

where T is temperature in °C, S is salinity in parts per thousand (ppt), and D is depth in meters (m). The variables must be within the parameters

$$0^\circ\text{C} \leq T \leq 35^\circ\text{C}, \quad 0 \text{ ppt} \leq S \leq 45 \text{ ppt}, \quad 0 \text{ m} \leq D \leq 1000 \text{ m}$$

for Medwin's equation to hold.

The effects from climate change on the effectiveness or accuracy of sonar systems can be theorized as follows: if the speed of sound through water varies due to rising temperatures, then the system may inaccurately calculate the distance of the object to the ship. If the attenuation of the signal through the ocean is higher than it is expected to be, then the range estimates generated by the sonar are reduced.

The change in accuracy of sonar is determined using Equation 1, and the change in effective range is determined using the sonar equation, which is the ratio of the sound intensity of the detected sonar signal that was emitted and reflected to the background noise present in the environment²:

$$SNR(\text{dB}) = SL - 2(TL_s + TL_a) + TS - NL. \quad (2)$$

Here, SNR is the Signal-to-Noise Ratio, SL is the source level, $TL_c = 10 \log_{10}(\frac{d}{d_{ref}})$ is the transmission loss due to the cylindrical spread of sound where $\frac{d}{d_{ref}}$ is the ratio of the initial reference distance* to the distance over which the sound travels³, TL_a is the transmission loss due to attenuation, TS is the target strength, and NL is the noise level. More advanced navigational systems will use beamforming⁴ to only listen for signals from a specific direction by using a spatial array of multiple receivers, effectively reducing the noise level and adding an additional term $+AG$ for array gain⁵.

There is precedence in this area of research with regards to the effects of climate change on ecological life, such as bats, dolphins, and whales which

* d_{ref} is set to a distance of 1 km in all subsequent calculations, as is standard for underwater acoustics applications².

communicate in various ranges of frequency bands. One especially relevant and extensive study is that conducted by Luo et al. (2013) on the effects of global warming on echolocating bats³. They theorize that bats are altering the frequencies of their calls to compensate for the increase in atmospheric transmission loss used in Equation 2, given by

$$TL_a = \alpha(d - d_{ref}) \quad (3)$$

where d_{ref} (km) is the reference distance to the sound source from where the sound pressure would be measured, d (km) is the distance that sound travels, and α (dB/km) is the atmospheric absorption coefficient, which is a function of frequency, air pressure, temperature, and relative humidity⁶.

Although the model formed by Luo et al. considers sonar frequencies travelling through air, the same concepts could also be directly applied to sonar travelling through water. Studies have also already shown that baleen whales, who typically operate in low frequencies (<100 Hz)⁷, are also decreasing the frequencies of their calls by a rate of more than 0.1 Hz per year⁸.

The main difference for applications of underwater acoustics is the definition of the absorption coefficient, which is now the seawater absorption coefficient defined as

$$\alpha = \alpha_{H_3BO_3} + \alpha_{MgSO_4} + \alpha_{H_2O} = \frac{A_1 P_1 f_1 f^2}{f_1^2 + f^2} + \frac{A_2 P_2 f_2 f^2}{f_2^2 + f^2} + A_3 P_3 f^2. \quad (4)$$

Here, $\alpha_{H_3BO_3}$, α_{MgSO_4} , and α_{H_2O} are the absorption contributions from boric acid⁹, magnesium sulphate, and pure water¹⁰, respectively, A_1, A_2, A_3 are constants, P_1, P_2, P_3 are the pressure dependencies of each compound, and f_1, f_2 are the relaxation frequencies of the two respective compounds. These are given by¹¹

$$f_1 = 0.78 \sqrt{\frac{S}{35}} e^{\frac{T}{26}} \text{ kHz},$$

$$f_2 = 42 e^{\frac{T}{17}} \text{ kHz}.$$

With all constants and functions inputted, the coefficient becomes:

$$\alpha = 0.0827 \frac{\sqrt{\frac{S}{35}} e^{\frac{T}{26}} f^2}{0.0174 S e^{\frac{T}{14}} + f^2} e^{\frac{pH-8}{0.56}} + 0.52 \left(1 + \frac{T}{43}\right) \left(\frac{S}{35}\right) \frac{42 e^{\frac{T}{17}} f^2}{1764 e^{\frac{2T}{17}}} e^{-\frac{D}{6}} + 0.00049 f^2 e^{-\frac{T}{27} - \frac{D}{17}} \quad (5)$$

which now is dependent on salinity S (ppt), acidity pH (pH), depth D (km), sea temperature T (°C), and frequency f (kHz) in the given units.

Ainslie and McColm¹¹ further simplify this equation by using $pH = 8$, $S = 35$ ppt, and $T = 10$ °C, however for the purposes of this study, the predicted change in these values are of importance to determine the increase of the α coefficient, and thus the decrease of effective range.

Methods

One location of interest had to be determined for this study, based on where changes in oceanic bio-markers such as temperature, salinity, and acidity change the most dramatically. This location should also be an area where sonar navigational systems are most critically used.

The main limiting factor in choice of location, however, was the ease of access and the extensiveness of available data for the region. We then decided that the region of interest would be the European shelf, which includes the North Sea and Mediterranean Sea. Vessel activity is typically most concentrated around bottlenecks and passages out to open water from ports with

high traffic and throughway channels, where it is most important for ships to get accurate sonar readings on their surroundings.

The data set we used was a POLCOMS-ERSEM product compiling marine biochemistry data in the European shelf from 2006 up to 2100, derived from CMIP5 climate projections¹². We used the RCP8.5 “business-as-usual” future scenario model, in which current activities concerning greenhouse gas emissions continue to rise through the century. Data with parameters of acidity, salinity, and sea water potential temperature were pulled and analyzed, with a resolution of 1 month. The values pulled were at a depth of 5 meters from the ocean surface. Atlas figures were created to show trends of the typical variation of the biomarker value within one year, and the total change in average biomarker value in a specified span of time. These two trends will be compared and we will discuss whether the total change over time due to climate change has significant potential effects on sonar communications.

One-year variation is calculated using the known formula for standard deviation, and total changes in average values of temperature, salinity, and acidity are calculated using the following formula:

$$\Delta X = \frac{\sum \mu_N}{N} = \frac{\sum \frac{x_{N_i}}{12}}{N}, \quad (6)$$

where $\frac{\sum x_i}{12}$ is the mean data value for a given year from twelve monthly data points and N is the number of years in the relevant time span of interest.

Analysis

One-year variations in each of the biomarkers were analyzed quantitatively and then graphed, showing examples for one year in the past (2006) and present (2023). The total change in the average value for each of the biomarkers was analyzed using Equation 6 and then graphed for spans of time in the past (2006 – 2023) and in the future (2023 – 2072).

The overall trends in variation and average values were then plotted and we determined whether they had weak or strong correlation depending on the residuals of the data to a linear fit, as well as whether the trends accurately represent the entire region of interest.

Although the data spans 2006 to 2100, our analysis was limited to 2072 in order to find more conclusive and relevant results for the “near future” in the next 50 years. It was found that year-by-year, from 2023 to 2072, there will be an increase in oceanic temperature and a decrease in salinity and acidity in the upper European continental shelf.

Temperature

The average sea water potential temperature is predicted to rise by approximately 1.2 °C in the next 50 years (Table 1). This change is of a smaller magnitude than that of the average variations of sea temperature in a given year, seen in Figure 5, and this yearly variation in temperature is also rising (Figure 2). In 2006, the sea temperature fluctuated by around 2.8 °C throughout the year. In 2072, temperatures are predicted to fluctuate by a little more than 3 °C during the year (Table 2). Fluctuations and long-term changes are seen across the entirety of the North Sea and Mediterranean Sea.

Salinity

The changes in salinity are mostly restricted to the shorelines off of Norway and the Adriatic Sea surrounded by Italy and Croatia, as seen in Figure 6. It is important to note that from 2006 to the present, overall salinity had been

rising in the Adriatic Sea, yet also decreasing in the North Sea closer to where polar ice formations occur. However, there appears to be an overall decreasing trend in salinity with a 20-year periodicity cycle, which can be seen in Figure 3. In the next 50 years, there is a predicted drop in salinity by approximately 0.2 PSU (Practical Salinity Units)[†] across the wider region of the open ocean, as seen in Table 1. The predicted year with the lowest oceanic salinity will occur in 2045.

No concurrent explanation could be found for the periodic trend, however the overall decrease is corroborated by Junlin et al. (2023) looking at salinity trends in the Pacific Ocean from 2005 to 2019¹³, and by Bagnell et al. (2023) studying global oceanic trends from 2001 to 2019¹⁴. Bagnell presents the correlation of steady, decreasing salinity with dilution due to the melting of icecaps, which introduce more freshwater into the oceans. Thus, we can speculate that the overall predicted change could be due to the disappearance of all ice formations. This aligns with some of the latest research conducted on when the world will first see ice-free summers, predicted to be in the 2030s – 2050s¹⁵.

Acidity

Overall acidity in the ocean is expected to decrease – becoming more acidic – in the next 50 years. This is a widely confirmed trend known as *ocean acidification* and is attributed to rising dissolved CO₂ levels¹⁶. The changes in acidity modelled from the dataset are concentrated to the north shoreline of the Western Mediterranean Basin, right in the French Gulf of Lion as seen in Figure 7. There is a clear trend of decreasing acidity year by year (Table 1) and in comparison the yearly acidity fluctuates at varying magnitudes year by year (Figure 4). Thus, the yearly variation has a statistically weak trend but the change in average acidity over time is still statistically significant.

Results

Accuracy

Using the yearly changes of each biochemical marker which showed strong trends, the changes in speed of sound (Equation 1) and transmission loss (Equation 5) through the ocean were calculated over the 50-year span, which were then used to determine the percentage decreases of accuracy and efficacy each year.

We calculated that the speed of sound in the relevant oceanic area will decrease by almost 18 m/s from 2023 to 2072, with an average yearly decrease in sound speed by about 0.37 m/s. This, in turn, implies that if an active sonar system is not re-calibrated it would decrease in accuracy by approximately 0.025% every year, and will read that objects are farther away due to the longer return time of the signal pulse — for example, if a new sonar instrument installed in 2006 originally measured an obstacle to be exactly 40 meters away, it would now measure that same obstacle to be at a distance of about 40.17 meters in 2023.

However, it is typical for sonar systems which critically rely on accurate sound speed to operate an on-board independent sound speed sensor in order to measure the exact local oceanic sound speed. We can assume that the possibility of a vessel's sonar navigational system to spend multiple years without recalibration is extremely unlikely.

Additionally, in comparison to the predicted long-term condition changes, currently there is an average variation of ± 2.763 °C and ± 0.193 ppt in the ocean throughout a given year. This implies that there is currently a higher yearly variability of 0.52% in an instrument's accuracy than what is pre-

[†]The sourced data¹² measures salinity in PSU, which is interchangeable with ppt. Calculations will reference salinity in ppt with no note for the change from PSU.

dicted by change over time.

Efficacy

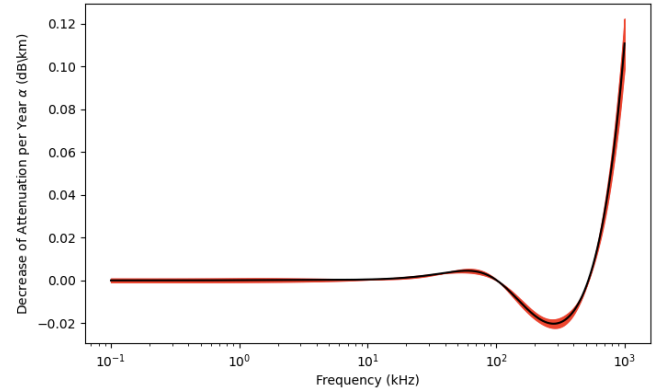


Figure 1. 11-order polynomial regression of the decrease in attenuation per year based on frequency. The red area denotes the error of the curve fit in addition to the 10% uncertainty of the absorption coefficient equation¹¹.

The seawater absorption coefficient α of transmission loss TL_a was approximated to be decreasing by an 11th order polynomial fit to Equation 5:

$$\begin{aligned} \alpha(f) = & (-7.55 \cdot 10^{-31})f^{11} + (4.34 \cdot 10^{-27})f^{10} - (1.09 \cdot 10^{-23})f^9 \\ & + (1.55 \cdot 10^{-20})f^8 - (1.38 \cdot 10^{-17})f^7 + (7.92 \cdot 10^{-15})f^6 \\ & - (2.91 \cdot 10^{-12})f^5 + (6.52 \cdot 10^{-10})f^4 - (7.51 \cdot 10^{-8})f^3 \\ & + (2.20 \cdot 10^{-6})f^2 + (1.14 \cdot 10^{-4})f - 8.65 \cdot 10^{-4} \end{aligned} \quad (7)$$

pertaining to the decrease in attenuation each year for frequencies between 100 Hz and 1 MHz, where $\alpha(f)$ is in dB/km and f is in kHz.

It can be seen for mid-range frequencies between 100 kHz and 500 kHz that attenuation will increase (Figure 1). This is the range in which the largest effect on attenuation is determined from contributions of magnesium sulphate¹⁰. Below that frequency range, the decrease of attenuation remains relatively stable around 10^{-3} dB/km where the largest contributor is boric acid⁹. In the highest frequency range, there is an exponential increase in attenuation loss due to viscous absorption¹¹.

The percentage change in attenuation represents the inverse percentage change in maximum detection distance, seen by how a decrease in seawater transmission loss leads to an increase of *SNR* at a minimum detectable level for a longer distance. And so, determining the average effects on each of these three ranges separately, the maximum operating ranges would theoretically be increasing by 0.06% for low-frequency sonar (100 Hz – 100 kHz), decreasing by 0.19% for mid-frequency sonar (100 kHz – 500 kHz), and increasing by 0.71% for high-frequency sonar (>500 kHz) every year, if the ambient noise level in the ocean did not change as well. However, the increase of all underwater sound propagation would be another factor to consider for determining the overall impact on the long-term changes to the maximum range of sonar at different frequencies.

Discussion

The results from this analysis can be compared to those found by Possenti et al. (2023)¹⁷ in their examination of the wider topic of the effects of climate change on underwater sound propagation. They concluded that while there is a future projected (2094 to 2098) global increase in underwater sound

speed, the North Atlantic Ocean and Norwegian Sea would uniquely see a decrease in sound speed by as much as 40 m/s from 2022. This is almost double the predicted decrease in sound speed in this analysis, which was determined to be closer to a 27 m/s drop in speed by 2094.

This discrepancy could possibly be attributed to the different methods of future projection modelling, where Possenti et al. took just four years of past data and projected it to four years of future data using the SSP5-8.5 future scenario. They also use a 6th order polynomial approximation of the speed of sound in water model given by¹⁸

$$c_{s,bous} = \sqrt{\frac{-\rho_0 g}{\frac{\partial r_0}{\partial z} - \frac{1}{z_u} \frac{\partial r}{\partial \zeta}}} \quad (8)$$

where ρ_0 is a constant reference density, z_u is a reference depth, $r_0(z)$ is a vertical reference profile, $r(S_A, \Theta, z)$ is a residual function, and $\zeta = -\frac{z}{z_u}$. In regards to the effective operating range of sonar detection and the decrease in attenuation, Possenti et al. find that there will be an increase in noise level NL by 7 dB by the end of the century. They come to the conclusion that propagation of ship noise in water will increase in the future, however they only examine single frequency at 125 Hz to find a total change in absorption coefficient of 0.0016 dB/km by 2094. Using our $\alpha(f)$ function, we calculate a decrease of $3 \cdot 10^{-6} \pm 0.0008$ dB/km per year. The uncertainty is beyond 2σ , which implies that our result does not have sufficient confidence.

Regardless, determining a frequency-dependent function for the decrease in seawater absorption coefficient per year allows for application in all ranges of sonar, from low-frequency naval operations to fishfinding and seabed mapping.

It should also be noted that this analysis was limited to a depth of 5 m below sea level, at which there is more variability in biomarkers over shorter time frames.

Conclusions

We conclude based on the isolated analysis conducted on changing oceanic temperature, salinity, and acidity in the upper European continental shelf, that the decrease in oceanic sound speed and subsequent decrease in accuracy in sonar navigation may be negligible when compared to the normal yearly fluctuations, and while it was quantitatively found that the change in transmission loss is frequency-dependent, the overall change in range of sonar detection is unknown due to the potential counter-effect of increases in ambient oceanic noise level.

Future research on this topic could include further analysis with the higher-order speed of sound model (Equation 8), as well as consider different depths in order to create a more comprehensive four-dimensional model of future conditions. Finally, analysis could be expanded to different areas of ocean to compare trends and put results into the global context.

Acknowledgements

This research was made possible from the teachings and encouragement of Prof. Yi Huang, as well as the aid from Qiurun Yu as a Teaching Assistant.

References

1. Medwin, H. Speed of sound in water: A simple equation for realistic parameters. *J. Acoust. Soc. Am.* **58**, 1318–1319 (1975). <https://doi.org/10.1121/1.380790>
2. Urick, R. J. *Principles of Underwater Sound* (Peninsula Publishing, 1984).
3. Luo, J., Koselj, K., Zsebok, S., Siemers, B. M. & Goerlitz, H. R. Global warming alters sound transmission: differential impact on the prey detection ability of echolocating bats. *J. R. Soc. Interface* **11**, 20130961 (2013). <https://doi.org/10.1098/rsif.2013.0961>
4. Chiang, A. M. & Broadstone, S. R. Sonar beamforming system (2005). US Patent 6,842,401.
5. Yan, L., Meng, Z., Chen, Y., Zhou, Z. & Chen, M. Vertical correlation and array gain analysis for vertical line array in deep water. *Appl. Sci.* **10**, 4709 (2020). <https://doi.org/10.3390/app10144709>
6. Attenborough, K. in *Springer Handbook of Acoustics* (ed Rossing, T. D.) 117–155 (Springer, 1979).
7. Adam, O. et al. New acoustic model for humpback whale sound production. *Appl. Acoust.* **74**, 1182–1190 (2013). <https://doi.org/10.1016/j.apacoust.2013.04.007>
8. Leroy, E. C., Royer, J. Y., Bonnel, J. & Samaran, F. Long-term and seasonal changes of large whale call frequency in the southern Indian Ocean. *J. Geophys. Res.* **123**, 8568–8580 (2018). <https://doi.org/10.1029/2018JC014352>
9. Francois, R. E. & Garrison, G. R. Sound absorption based on ocean measurements. Part II: Boric acid contribution and equation for total absorption. *J. Acoust. Soc. Am.* **72**, 1879–1890 (1982). <https://doi.org/10.1121/1.388673>
10. Francois, R. E. & Garrison, G. R. Sound absorption based on ocean measurements: Part I: Pure water and magnesium sulfate contributions. *J. Acoust. Soc. Am.* **72**, 896–907 (1982). <https://doi.org/10.1121/1.388170>
11. Ainslie, M. A. & McColm, J. G. A simplified formula for viscous and chemical absorption in sea water. *J. Acoust. Soc. Am.* **103**, 1671–1672 (1998). <https://doi.org/10.1121/1.421258>
12. Kay, S., Clark, J., Hall, A., Marsh, J. & Fernandes, J. Marine biogeochemistry data for the Northwest European Shelf and Mediterranean Sea from 2006 up to 2100 derived from climate projections. *Copernicus Climate Change Service (C3S) Climate Data Store (CDS)* <https://doi.org/10.24381/cds.dcc9295c> (2020).
13. Junlin, R., Chao, N., Wang, Z., Wu, T., Li, C., et al. Quantifying the contribution of temperature, salinity, and climate change to sea level rise in the Pacific Ocean: 2005–2019. *Front. Mar. Sci.* **10**, 1200883 (2023). <https://doi.org/10.3389/fmars.2023.1200883>
14. Bagnell, A. & DeVries, T. Global mean sea level rise inferred From ocean salinity and temperature changes. *Geophys. Res. Lett.* **50**, e2022GL101004 (2023). <https://doi.org/10.1029/2022GL101004>
15. Kim, Y. H., Min, S. K., Gillett, N. P., Notz, D. & Malinina, E. Observationally-constrained projections of an ice-free Arctic even under a low emission scenario. *Nat. Commun.* **14**, 3139 (2023). <https://doi.org/10.1038/s41467-023-38511-8>
16. Doney, S. C., Fabry, V. J., Feely, R. A. & Kleypas, J. A. Ocean acidification: the other CO2 problem. *Ann. Rev. Mar. Sci.* **1**, 169–192 (2009). <https://doi.org/10.1146/annurev.marine.010908.163834>
17. Possenti, L. et al. Predicting the contribution of climate change on North Atlantic underwater sound propagation. *PeerJ* **11**, e16208 (2023). <https://doi.org/10.7717/peerj.16208>
18. Roquet, F., Madec, G., McDougall, T. J. & Barker, P. M. Accurate polynomial expressions for the density and specific volume of seawater using the TEOS-10 standard. *Ocean Model.* **90**, 29–43 (2015). <https://doi.org/10.1016/j.ocemod.2015.04.002>

Table 1. Average values for seawater temperature, salinity, and acidity in 2006, 2023, and predicted 2072 values, as well as the average change over 65 years (Figure 4).

Year	One-Year Average		
	\bar{T}	\bar{S}	\bar{pH}
2006	15.91 °C	36.10 PSU	8.175
2023	16.19 °C	36.17 PSU	8.165
2072	17.48 °C	35.89 PSU	8.134
Yearly Change in Average (2006–2072)	+0.021 °C	-0.0065 PSU	-0.00072

Table 2. Yearly variation of seawater temperature, salinity, and acidity in 2006, 2023, and predicted 2072 values, as well as the change in variation over 65 years (Figure 4).

Year	One-Year Variation		
	σ_T	σ_S	σ_{pH}
2006	±2.757 °C	±0.196 PSU	±4.670
2023	±2.763 °C	±0.193 PSU	±2.618
2072	±3.072 °C	±0.207 PSU	±3.086
Yearly Change in Variation (2006–2072)	+0.003 °C	+0.0002 PSU	-0.00006

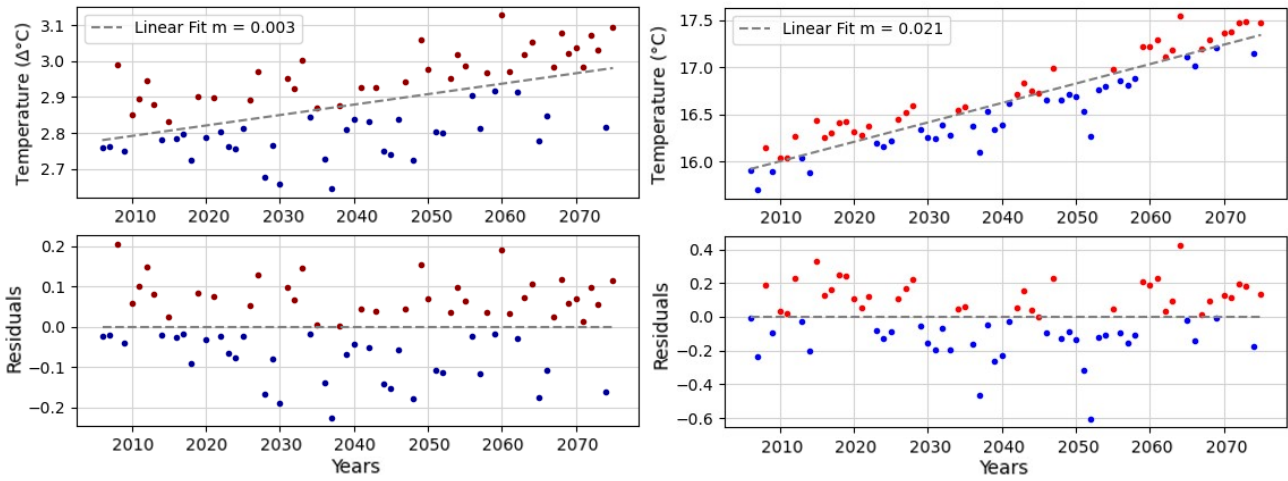


Figure 2. Linear regressions and residuals of yearly sea water potential temperature ($^{\circ}\text{C}$) and fluctuation of sea water potential temperature ($\Delta^{\circ}\text{C}$) in the European Shelf at a depth of 5 meters, from 2006 to 2072.

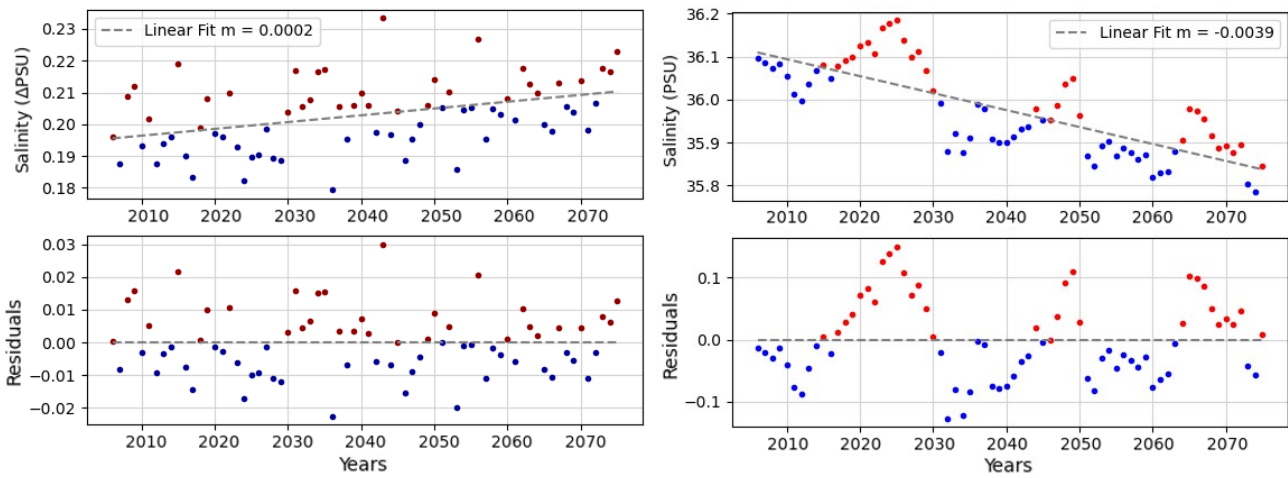


Figure 3. Linear regressions and residuals of yearly sea water salinity (PSU) and fluctuation of sea water salinity (ΔPSU) in the European Shelf at a depth of 5 meters, from 2006 to 2072.

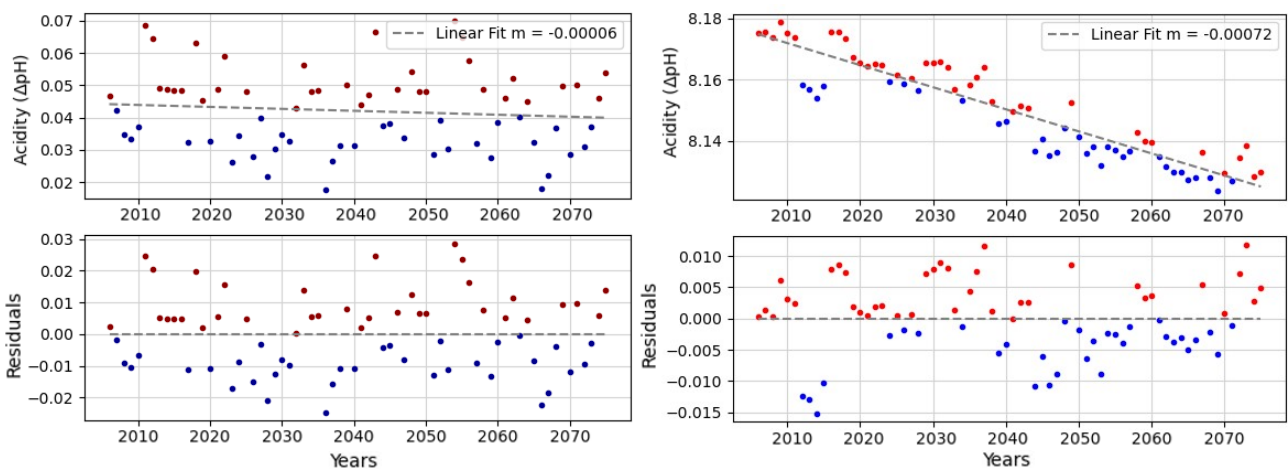


Figure 4. Linear regressions and residuals of yearly sea water acidity (pH) and fluctuation of sea water acidity (ΔpH) in the European Shelf at a depth of 5 meters, from 2006 to 2072.

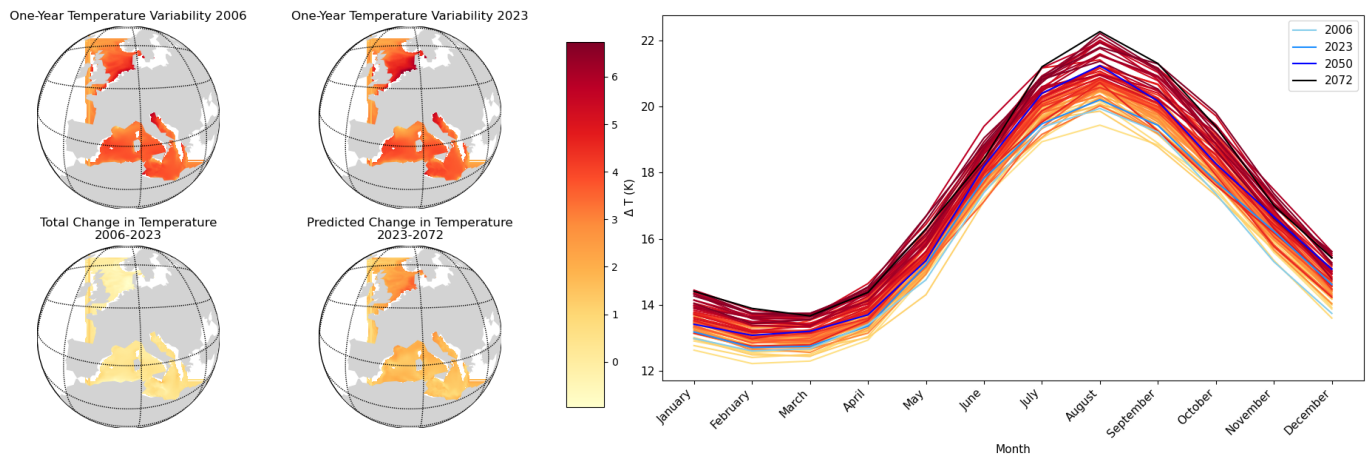


Figure 5. Geographical and yearly line trends of sea water potential temperature ($^{\circ}\text{C}$) in the European Shelf at a depth of 5 meters, from 2006 to 2072.

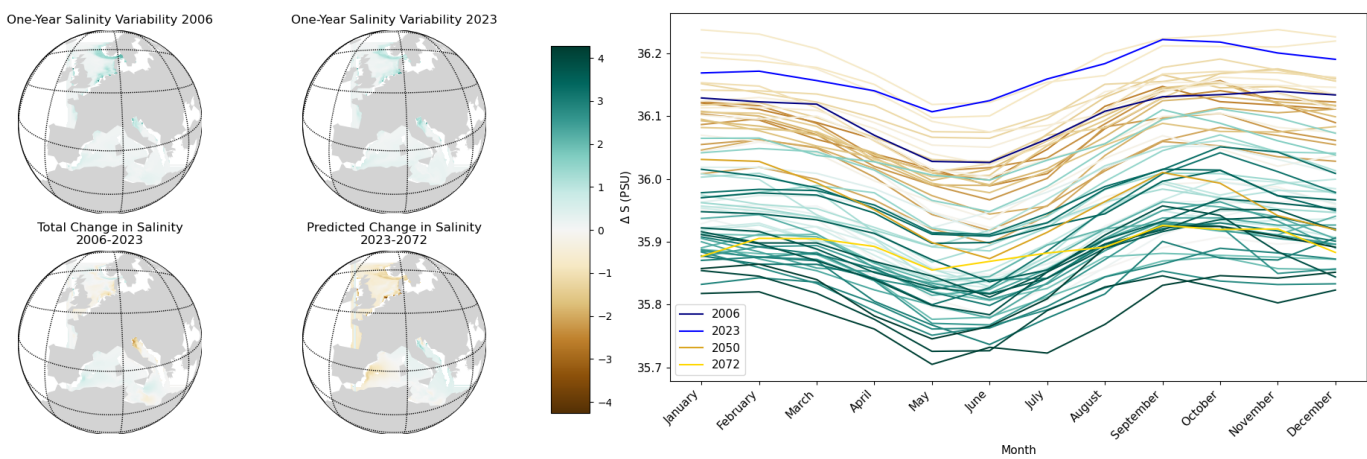


Figure 6. Geographical and yearly line trends of in sea water salinity (PSU) in the European Shelf at a depth of 5 meters, from 2006 to 2072.

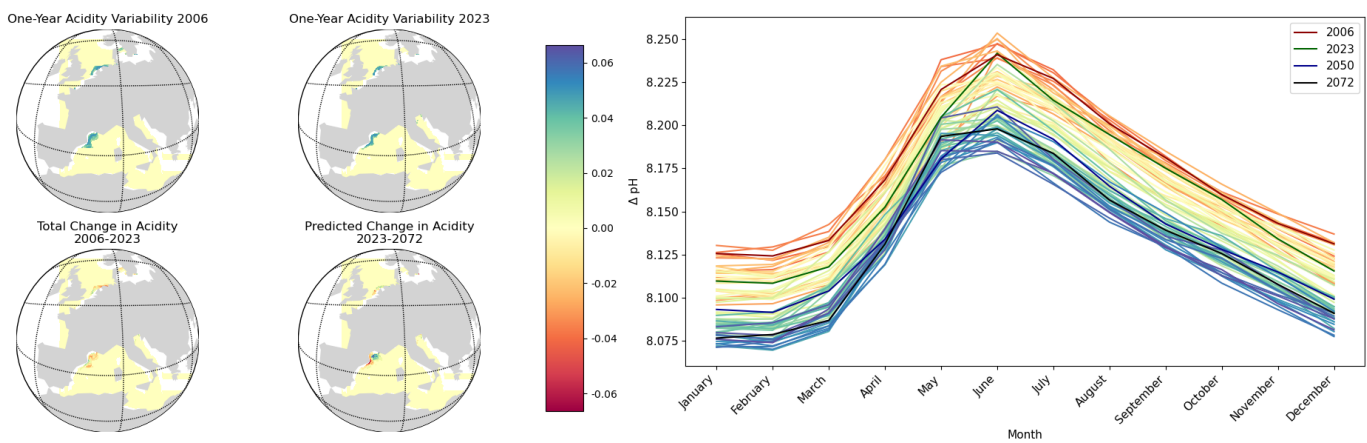


Figure 7. Geographical and yearly line trends of sea water acidity (pH) in the European Shelf at a depth of 5 meters, from 2006 to 2072.

Research Article

¹Graduate Program in Biotechnology Engineering, SupBiotech, Villejuif, France

²Food Engineering Laboratory (LRPIA), SupBiotech, Villejuif, France

³CellTechs Laboratory, SupBiotech, Villejuif, France

⁴Service d'Etude des Prions et des Infections Atypiques (SEPIA), Institut Français Jacob, Commissariat à l'Energie Atomique et aux Energies Alternatives (CEA), Université Paris Saclay, Fontenay-aux-Roses, France

⁵Teaching Laboratories, SupBiotech, Villejuif, France

Keywords

Aspergillosis, *Aspergillus oryzae*, *Origanum compactum*, *Cinnamomum cassia*, essential oils.

Email Correspondence

agnes.saint-pol@supbiotech.fr

<https://doi.org/10.26443/msurj.v19i1.239>

©The Authors. This article is published under a CC-BY license: <https://creativecommons.org/licenses/by/4.0/>

Manon Leclercq¹, Isciane Commenge¹, Marylou Bouriot¹, Floricia Crusset¹, Patrick Gonzalez², Julien Grimaud^{3,4}, Frank Yates^{3,4}, Jacqueline Sarfati-Bert⁵, Agnès Saint-Pol²

Cinnamomum cassia and *Origanum compactum* Essential Oils as Antifungal Candidates for the Treatment of Aspergillosis

Abstract

Aspergillosis is a disease that usually affects the respiratory system. While most patients develop mild symptoms, aspergillosis can become a serious health threat in immunocompromised populations and patients with pre-existing respiratory conditions. Aspergillosis is caused by fungi of the *Aspergillus* genus. Existing treatments include drugs such as azoles, ergosterol interfering agents (Amphotericin B), and echinocandins (Caspofungin), which usually come with various drawbacks. Numerous studies have shown the antifungal properties of certain essential oils (EOs), which represent potential alternative treatments against fungal infections. Here, we screened the antifungal properties of five EOs against *Aspergillus oryzae*: *Melaleuca alternifolia*, *Mentha x piperita*, *Thymus zygis*, *Origanum compactum*, and *Cinnamomum cassia*. Of the five EOs, two demonstrated antifungal activity: *Origanum compactum* acted as a fungistatic, while *Cinnamomum cassia* showed both fungistatic and fungicidal effects against *A. oryzae*. Therefore, both EOs represent potential alternative treatments against Aspergillosis.

Introduction

Aspergillosis is an infection of the respiratory tract caused by members of the genus *Aspergillus*. Their infectious abilities reside in their asexual spores, also known as conidia (singular: conidium). *Aspergillus* conidia are found everywhere in the environment (such as air, soil, plants, and water) as well as inside houses and hospitals. Patients become infected by inhaling fungi, which then grow inside the lungs^{1,2}.

Depending on the state of the host's immune system, aspergillosis may cause various complications. For instance, in immunocompromised patients, it usually leads to a lung disease named invasive pulmonary aspergillosis, which is the most common cause of death by aspergillosis. Other aspergillosis related pathologies exist, such as allergic bronchopulmonary aspergillosis (ABPA), which occurs in atopic patients^{2,3}.

While many species of the genus *Aspergillus* may cause aspergillosis, one of the most reported pathogens is *Aspergillus fumigatus*^{1,2}. *A. fumigatus* is a Class 2 pathogenic agent⁴. Therefore, scientists who wish to study it

must gain access to research facilities of an equivalent biosafety level. While *A. fumigatus* is the main cause of aspergillosis, other fungi of the genus *Aspergillus* can also cause it. For example, the presence of *Aspergillus oryzae* is often reported in cases of ABPA^{5,6}. *A. oryzae* is classified as a Class 1 pathogenic agent⁷, which means it may be handled in any research facility of a minimal biosafety level.

Various *Aspergillus* genomes, including that of *A. oryzae*, share a high degree of similarity with *A. fumigatus*. This suggests that they are phylogenetically very close to each other⁸. In addition, the similarity between *A. fumigatus* and other *Aspergillus* species such as *A. flavus*, *A. niger*, *A. oryzae* and *A. nidulans* has been studied at the amino acid level. In brief, researchers calculated their percentage of similarity from an alignment of 2753 orthologous proteins. Based on this alignment, researchers found a 78% similarity between *A. fumigatus* and *A. oryzae* — a result on par with the other reported *Aspergillus* species⁹ (Table 1). It is worth noting that some studies suggest that both *A. fumigatus* and *A. oryzae* may be able to reproduce asexually¹⁰, although this last point is subject to debate¹¹. Finally, many studies have shown the antifungal effect of our EO panel against other members

of the genus *Aspergillus*, including *A. fumigatus*^{12–18}, which suggests shared mechanisms of action across many *Aspergillus* species. Therefore, *A. oryzae* represents a good alternative model to *A. fumigatus* for scientists who wish to study aspergillosis agents with no access to high biosafety level facilities.

Table 1. Percentage of similarity from an alignment of 2753 orthologous proteins across *Aspergillus* genomes. *A. oryzae* and *A. fumigatus* show the highest percentage of alignment. Adapted from Rokas and Galagan, 2007⁹.

	<i>A. flavus</i>	<i>A. niger</i>	<i>A. oryzae</i>	<i>A. nidulans</i>
<i>A. fumigatus</i>	77.5%	76.6%	78%	73.9%

Nowadays, aspergillosis is treated with antifungal drugs, which usually consist of azoles, ergosterol interfering agents (Amphotericin B[®]) and echinocandins (Caspofungin[®])². However, these drugs suffer from numerous drawbacks, which limits their efficacy and practicability. For instance, azoles have been shown to interact with numerous other drugs. In addition, recent studies have noted an increase in the prevalence of azole resistance in *A. fumigatus*. Ergosterol interfering agents have serious side effects such as renal toxicity leading to renal insufficiency, and may cause allergic reactions (e.g., skin rashes, bruising, and troubled breathing). Finally, echinocandins are typically delivered through parenteral injections, which limit their use outside of the hospital. Therefore, there is a need for alternative treatments to aspergillosis that are less toxic to patients, more convenient to deliver, and more effective^{2,5,19}.

Our goal was to identify new candidate drugs against aspergillosis. Previous studies have investigated the antifungal properties of certain essential oils (EOs), which are aromatic extracts usually obtained through the steam distillation of plants^{3,12–16,20}. Therefore, we decided to test five EOs against *A. oryzae*: *Mentha x piperita*, *Melaleuca alternifolia*, *Thymus zygis*, *Origanum compactum*, *Cinnamomum cassia*. Most of these EOs have known activity against *Aspergillus* strains. For instance, *Mentha x piperita* appeared effective against *A. flavus* and *A. parasiticus*¹². *Melaleuca alternifolia* showed antifungal activity against *A. niger*¹³. *Thymus zygis* and *Origanum compactum* revealed antifungal properties against both *A. flavus* and *A. niger*¹⁴. *Origanum compactum* contains a phenolic compound called carvacrol which could explain its inhibiting activity on some *Aspergillus* strains^{14,15}. Finally, *Cinnamomum cassia* also showed a high antifungal activity against *A. niger*, probably because it contains cinnamaldehyde, an antifungal molecule¹⁶.

In this paper, we investigate the antifungal activity of these five EOs at various concentrations against *A. oryzae*. We further evaluate both the fungistatic (ability to prevent fungal growth) and fungicidal (ability to kill fungi) activity of two EO that showed promising antifungal activity at low concentrations. Overall, *Cinnamomum cassia* appears to be the best candidate, as it exhibits both fungistatic and fungicidal activities against *A. oryzae*.

Methods

Fungal Strain and Preculture

Aspergillus oryzae var. *oryzae* CBS 816.2 was purchased from the CBS-KNAW Fungal Biodiversity Centre (Netherlands).

Prior to the experiments, we prepared fungal precultures as follows: we seeded *A. oryzae* into a Czapek Agar medium (0.01 g/L ferrous sulfate, 0.5 g/L magnesium sulfate, 0.5 g/L potassium chloride, 1 g/L potassium phosphate, 3 g/L sodium nitrate, 30 g/L D-sucrose, 12 g/L agar) containing 1 M of KCl. The preparation was incubated at 30 °C for 6 days. We then collected the fungi with 0.05% Tween-20[®] (ref. P1379, Sigma Aldrich, Burlington MA, USA). Finally, the fungal concentration was adjusted to 10⁵ conidia/mL.

dia/mL.

Essential Oil Safety

All essential oils used in this study have been graded as “GRAS” (Generally Recognized As Safe) by the Flavor Extract Manufacturers Association. In addition, we manipulated essential oils following safe laboratory practices and all manufacturer’s recommendations. Nevertheless, all EOs, even when graded as GRAS and commercially available, may bear toxic effects at high doses, which includes sensitization, dermatitis, as well as digestive and neurotoxic effects²¹.

Antifungal Screening

We first screened the five EOs for their antifungal abilities. We prepared a stock Sabouraud medium (10 g/L peptone, 20 g/L glucose) containing 0.05% Tween-20[®]. For each EO, we then prepared an initial dilution consisting of a weighted amount of the EO added to the stock medium. Further dilutions were obtained through serial dilutions. Below are the resulting EO concentrations, as well as the concentration for the controls *Ocimum basilicum* (an EO with no known antifungal properties) and Amphotericin B[®]:

- *Melaleuca alternifolia* (EAN 5420008503917, Pranarôm, Ghislenghien, Belgium): 1 mg/mL; 2 mg/mL; 3 mg/mL; 4 mg/mL.
- *Mentha x piperita* (EAN 3401560104783, PurEssentiel, Bruxelles, Belgium): 1 mg/mL; 2 mg/mL; 3 mg/mL; 4 mg/mL.
- *Thymus zygis* (EAN 3401599455122, Pranarôm, Ghislenghien, Belgium): 0.5 mg/mL; 1 mg/mL; 2 mg/mL; 3 mg/mL.
- *Origanum compactum* (EAN 3401599454002, PurEssentiel, Bruxelles, Belgium): 500 µg/mL; 600 µg/mL; 700 µg/mL; 1000 µg/mL.
- *Cinnamomum cassia* (EAN 5420008506826, Pranarôm, Ghislenghien, Belgium): 5 µm/mL; 20 µm/mL; 30 µm/mL; 50 µm/mL; 200 µm/mL; 500 µm/mL.
- *Ocimum basilicum* (EAN 3701056802378, PurEssentiel, Bruxelles, Belgium): 1 mg/mL.
- Amphotericin B[®] (ref. Y0000005, Sigma Aldrich, Burlington MA, USA): 2 µm/mL.

After we attained our desired EO dilutions, we added *A. oryzae* (final working concentration in each well: 10⁴ conidia/mL). The mixtures of EO and fungus were then poured in a single well each of a 24-well plate (final volume: 1 ml per well). As additional controls, wells containing only the Sabouraud medium and the Sabouraud medium with 0.05% Tween-20[®] were also seeded with 10⁴ conidia/mL to verify the viability of the *A. oryzae* strain and to ensure that any observed effects were not due to potential antifungal properties of the growth medium (final volume: 1 ml per well) (Table 2, rows 1 to 4).

The wells were then incubated for 48h at 30 °C. The results were observed with an inverted microscope (ref. AE31E, Motic).

Fungicidal and Fungistatic Test

After the initial screening of the five EOs, we further investigated two EOs with promising profiles. We first prepared a stock solution of solid Sabouraud medium (10 g/L of peptone, 20 g/L glucose, 20 g/L agar). For each EO chosen for the fungicidal/fungistatic test, we then prepared an initial dilution by weighting the EO and adding it to the stock medium. Subsequent dilutions were obtained through serial dilutions. Below are the final EO concentrations, as well as concentration for the controls *Ocimum basilicum* and Amphotericin B[®]:

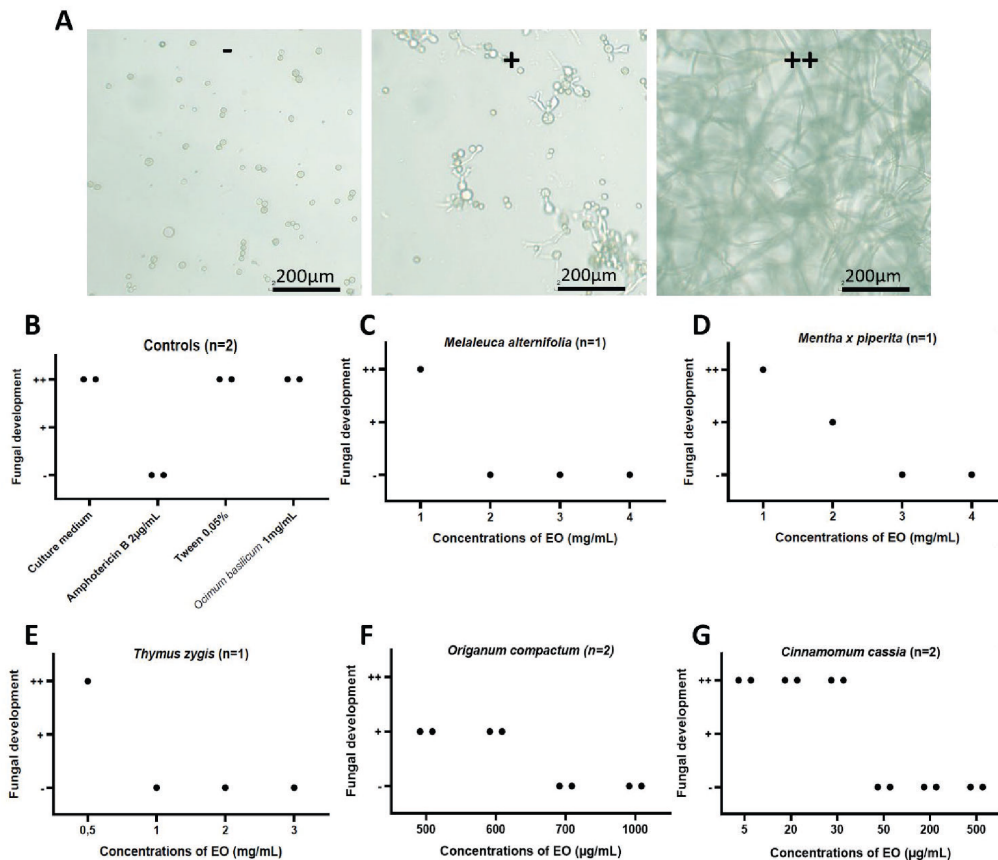


Figure 1. Discrimination criteria of *A. oryzae* growth after 48h incubation with EOs or control treatments. For all panels, the fungal development will be scored as follows: (-) no development, (+) start of germination, (++) network formation.

- *Origanum compactum*: 700 µg/mL, 800 µg/mL, 900 µg/mL.
- *Cinnamomum cassia*: 20 µg/mL, 30 µg/mL, 50 µg/mL.
- *Ocimum basilicum*: 1 mg/mL.
- Amphotericin B[®]: 2 µg/mL.

We poured the media into Petri dishes (diameter 55 mm, Sarstedt). As additional controls, Petri dishes containing only the solid Sabouraud medium and the Sabouraud medium with 0.05% Tween-20[®] were also prepared.

A 6 mm diameter cellulose disk (Merck) was then soaked in a preculture of 10⁴ conidia/mL of *A. oryzae* and laid at the center of each Petri dish. The dishes were incubated for either 48h or 72h. After this first incubation, each diffusion disk was moved onto the center of a new Petri dish containing fresh Sabouraud solid medium and incubated for 48h.

We measured the diameter of the growth disk using a ruler at various times: end of first incubation, 24h after the start of the second incubation, and end of second incubation. All measurements of 6 mm or less were considered as an absence of fungal growth, as 6 mm was the diameter of the cellulose disk alone.

Results

Antifungal Screening

To screen which EOs had antifungal activity, we incubated *A. oryzae* spores in the presence of the EOs *Melaleuca alternifolia*, *Mentha x piperita*, *Thy-*

mus zygis, *Origanum compactum*, and *Cinnamomum cassia* at various concentrations for 48h (Figure 1, Table 2). *A. oryzae* germinates and forms a hyphal network in only 24h²². Therefore, for a given EO, if the growth medium was free of hyphae after 48h, we concluded that the EO was a potential inhibitor of *A. oryzae* development. On the contrary, if germination began or a network started to form after 48h, we concluded that the EO had no observable antifungal activity against our strain of interest (Figure 1). The results, including controls, are in Table 2.

The control results are in rows 1 to 4. As expected, the control well containing the growth medium with no EO had fungus that formed networks

Table 2. Screening of candidate EOs inhibiting *A. oryzae* growth. The rows show the different conditions we tested (EOs and controls), while the columns represent the concentrations in mg/ml (n.a.: not applicable). For each condition, the fungal development is scored as follows: (-) no development, (+) start of germination, (++) network formation (see Figure 1). Conditions that were not tested appear as gray crossed out cells. The four first rows report the control conditions (culture medium alone; Amphotericin B; *Ocimum basilicum*; Tween-20), while the other rows show the results of our EO test screenings. To the right of each condition, n gives the number of replicates. For conditions with n greater than 1, the results of all replicates were always identical, hence we did not distinguish them in this table.

	(n.a.)	0.002	0.005	0.02	0.03	0.05	0.2	0.5	0.6	0.7	1	2	3	4
Culture medium (n=2)	++													
Amphotericin B (n=2)	-													
Tween 0.05% (n=2)	++													
Ocimum basilicum (n=2)											++			
Melaleuca alternifolia (n=1)											++	-	-	-
Mentha x piperita (n=1)											++	+	-	-
Thymus zygis (n=1)								++			-	-	-	-
Origanum compactum (n=2)								+	+	-	-	-	-	-
Cinnamomum cassia (n=2)		++	++	++	-	-	-	-	-	-	-	-	-	-

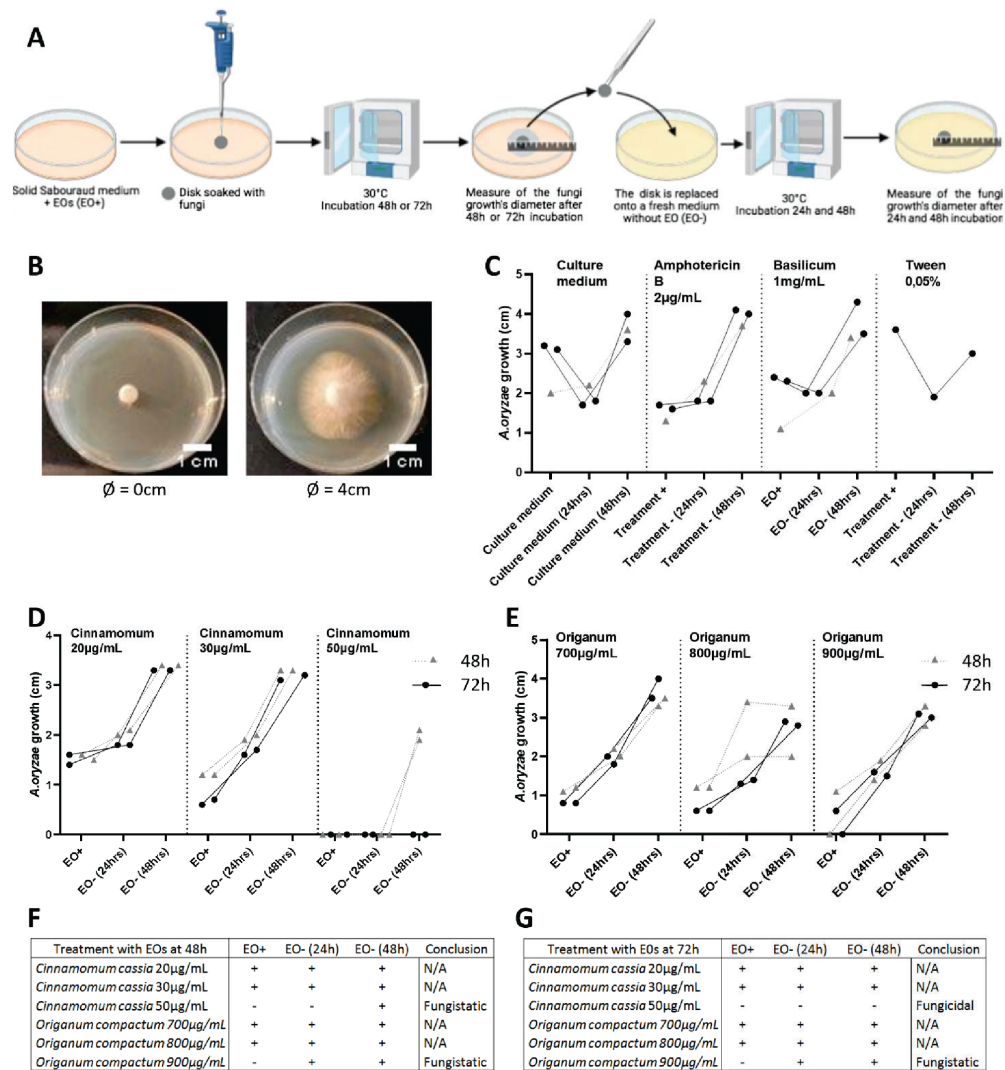


Figure 2. Fungicidal and fungistatic effects of EOs on *A. oryzae*. **(A)** Experimental approach. A cellulose disk saturated with *A. oryzae* is placed in a Petri dish containing solid Sabouraud medium with the EO of interest (EO+). The dish is incubated for 48 to 72h, after which fungal growth is measured. Then the disk is transferred in a new dish with EO-free medium (EO-). The fungal growth is measured at 24 and 48h of incubation. Fungicidal EOs would prevent growth in both EO+ and EO- conditions, while fungistatic EOs would prevent fungal growth in the EO+ condition only. **(B)** Exemplar growth disks. Left: no apparent growth. Right: 4 cm growth. We measured fungal growth as the diameter of the disk after incubation. All diameters of 6 mm or less were considered as an absence of fungal growth, as 6 mm was the diameter of the cellulose disk alone. **(C)** Control conditions (culture medium alone; Amphotericin B; *Ocimum basilicum*; Tween-20). For all graphs: all dots corresponding to the same cellulose disk are connected with a line. Grey triangles and dotted lines: the disks were left 48h in the EO+ medium. Black circles and solid lines: the EO+ incubation lasted 72h. **(D), (E)** Fungal growth in EO+ and EO- conditions. In **(D)**, the EO+ medium contained *Cinnamomum cassia*, while it contained *Origanum compactum* in **(E)**. **(F), (G)** Summary table of the measurements obtained from disks incubated for 48h **(F)** or 72h **(G)** in the EO+ condition. For all tables: (-) means an absence of fungal growth, while (+) represents an apparent growth.

inside the wells. This also confirmed the viability of the *A. oryzae* strain. The well containing Amphotericin B, a well-known antifungal drug²³, prevented the development of *A. oryzae*. Finally, the well containing *Ocimum basilicum*, an EO with no known antifungal activity¹⁹, did not prevent fungal growth, as expected.

The results of screening the five EOs at various concentrations are in rows 5 to 9. Three EOs (*Melaleuca alternifolia*, *Mentha x piperita*, and *Thymus zygis*) showed antifungal activity only at concentrations higher than 1 mg/mL. Two, *Origanum compactum* and *Cinnamomum cassia*, showed antifungal activity at concentrations as low as 700 µg/mL and 50 µg/mL, respectively.

Having identified *Origanum compactum* and *Cinnamomum cassia* as two promising EO candidates with antifungal activity at relatively low concentrations, we then decided to further investigate their antifungal properties.

Fungistatic or Fungicidal Properties of Selected EOs

We performed fungicidal and fungistatic tests with *Cinnamomum cassia* and *Origanum compactum* against *A. oryzae* (Figure 2). Briefly, we placed a small cellulose disk saturated with a solution of *A. oryzae* spores in a Petri dish containing a layer of solid Sabouraud medium mixed with the EO of interest (EO+). The Petri dish was incubated for 48 to 72h, after which we measured the diameter of fungal growth. Then, we transferred the same paper disk in a new Petri dish with fresh, EO-free medium (EO-) and measured, once again, the fungal growth after 24 and 48h of incubation (Figure 2A, 2B). Fungicidal substances would prevent fungal growth in both EO+ and EO- conditions, while fungistatic compounds would prevent fungal growth in the EO+ condition only.

Prior to this, we conducted another series of control tests (Figure 2C). As before, we examined the viability of our fungus strain: *A. oryzae* success-

fully formed a growth disk both prior to and after transfer to a new Petri dish. In addition, we confirmed the fungistatic effect of Amphotericin B²³, and the lack of antifungal activity from both *Ocimum basilicum*¹⁹ and the culture medium (with and without Tween-20).

The results of the tests on *Cinnamomum cassia* and *Origanum compactum* are in Figure 2D-2G. Both EOs inhibited the growth of *A. oryzae* in the EO+ condition at the highest concentration tested (*Cinnamomum cassia*: 50 µg/mL; *Origanum compactum*: 900 µg/mL), which confirmed the antifungal activity previously observed. Furthermore, the disks transferred from the EO+ to the EO- condition after 48h of incubation displayed sizeable growth, indicative of a fungistatic effect from both *Cinnamomum cassia* and *Origanum compactum* (Figure 2D-2F).

However, after 72h of incubation in the EO+ condition, the two EOs showed different results. While we noted a fungistatic effect from *Origanum compactum*, the disk taken from *Cinnamomum cassia* EO+ medium developed no growth disk, indicating a fungicidal effect (Figure 2D, 2E, 2G).

To conclude, we confirmed that both *Cinnamomum cassia* and *Origanum compactum* have antifungal properties against *A. oryzae*. We also detected a fungistatic effect from *Origanum compactum*, and both a fungistatic and fungicidal effect from *Cinnamomum cassia* depending on the duration of the incubation in contact with the EO.

Discussion

Cinnamomum cassia, a Fungicidal EO Against *A. oryzae*

While all EOs exhibited some antifungal activity, *Origanum compactum* and *Cinnamomum cassia* were most effective, exhibiting antifungal activity at concentrations of 700 µg/mL and 50 µg/mL, respectively (Figure 1, Table 2). Both EOs exhibited fungistatic activity. Interestingly, when the fungus was in contact with the EO for 72h, *Cinnamomum cassia* also acted as a fungicidal agent.

The main antifungal ingredient of *Cinnamomum cassia* is cinnamaldehyde¹⁶⁻¹⁸. Cinnamaldehyde acts by impairing two essential biological processes: it disrupts ATPase activity and inhibits the synthesis of fungal cell walls^{17,18}. Other varieties of cinnamon-based EOs exist, such as *Cinnamomum zeylanicum* (bark), which also contains cinnamaldehyde. A previous study found that *Cinnamomum cassia* was slightly better at inhibiting *A. niger* growth than *Cinnamomum zeylanicum*¹⁶. This is not surprising, considering the composition of these EOs: *Cinnamomum cassia* contains about 66% of cinnamaldehyde, while *Cinnamomum zeylanicum* contains 64%¹⁶. Therefore, one would expect *Cinnamomum cassia* to also show greater antifungal activity against *A. oryzae* than *Cinnamomum zeylanicum*. This hypothesis is open for testing.

Cinnamomum cassia, a Non-Toxic Potential Alternative to Current Aspergillosis Treatment

We showed that *Cinnamomum cassia* is an effective fungicidal agent against *A. oryzae* at concentrations as low as 50 µg/mL *in vitro*. Interestingly, *in vitro* studies suggest that *Cinnamomum cassia* is non mutagenic²⁴. Furthermore, rats subjected to daily oral doses of this EO showed signs of potential toxicity only at very high doses (2 g/kg/day)²⁴. Therefore, it may be possible to deliver a treatment containing *Cinnamomum cassia* orally. Another delivery route is directly to the lungs, using an inhaler – although this method is yet to be proven safe and should be tested *in vivo*. In addition, promising innovative approaches aimed at delivering volatile drugs, such as nanoemulsion, nanopreparations, and nanocarriers, are currently under investigation²⁵⁻²⁷. If proven effective, they may be suitable for *Cinnamo-*

mum cassia.

A recent study found that *Cinnamomum zeylanicum* and *Rosmarinus officinalis*, when combined, had a synergic effect against fungi developing on pears, meaning that the antifungal effect of the EO mix was greater than the sum of the antifungal activities measured separately²⁸. As a future avenue, it would be interesting to test the potential synergic effect of *Cinnamomum cassia* and *Origanum compactum*.

Conclusion

Aspergillosis is a nosocomial infection of the respiratory system caused by *Aspergillus*, a genus of fungi found pervasively in the environment both indoors and outdoors^{1,2}. Conventional treatments consist of antifungal drugs, namely ergosterol interfering agents (Amphotericin B), echinocandins (Caspofungin), and azoles. However, these drugs have numerous drawbacks^{2,5,19}. In addition, certain studies suggest that *Aspergillus* may still grow in the presence of these drugs^{2,19}. Therefore, there is a need for alternative treatments against *Aspergillus*.

Several research teams have reported on the antifungal potential of essential oils against *Aspergillus* strains^{3,12-16,20}. Therefore, we decided to characterize the antifungal activity of five essential oils against *Aspergillus oryzae*, a species known to cause specific forms of aspergillosis. These were *Melaleuca alternifolia*, *Mentha x piperita*, *Thymus zygis*, *Origanum compactum*, and *Cinnamomum cassia*. These EOs were already known for their antifungal activity against some members of the genus *Aspergillus*¹²⁻¹⁸. However, to our knowledge, no past study has assessed the effect of these EOs against *A. oryzae* specifically.

Two essential oils stood out from our initial screening: *Origanum compactum* and *Cinnamomum cassia*. Both EOs showed strong fungistatic activity against *Aspergillus oryzae*. In addition, when left in contact with the fungus for 72h, *Cinnamomum cassia* showed a clear fungicidal effect against *Aspergillus oryzae* at concentrations as low as 50 µg/ml. Therefore, *Cinnamomum cassia* may represent a valuable alternative to conventional treatments against aspergillosis. Its potential as a drug treatment should be assessed next through *in vivo* studies.

Author Contribution

M.L., I.C., M.B., F.C., J.S.-B., and A.S.-P. designed the experiments. M.L., I.C., M.B., and F.C. performed the experiments, under the supervision of J.S.-B. and with precious advice from P.G. and F.Y. The first draft of the manuscript was written by M.L., I.C., M.B., and F.C. The manuscript was revised by J.G., J.S.-B., and A.S.-P. These experiments were conducted through the “Projets Fil Rouges” (Applied Transversal Projects), a student-led research program directed by F.Y. at Sup’Biotech.

References

1. Sugui, J., Kwon-Chung, K., Juvvadi, P., Latge, J.-P. & Steinbach, W. *Aspergillus fumigatus* and Related Species. *Cold Spring Harb. Perspect. Med.* **5**, 019786–019786 (2015). <http://doi.org/10.1101/cshperspect.a019786>
2. Latgé, J.-P. & Chamilos, G. *Aspergillus fumigatus* and Aspergillosis in 2019. *Clin. Microbiol. Rev.* **33**, e00140–181 (2019). <http://doi.org/10.1128/CMR.00140-18>

3. El-Baba, F., Gao, Y. & Soubani, A. Pulmonary Aspergillosis: What the Generalist Needs to Know. *Am. J. Med.* **133**, 668–674 (2020). <http://doi.org/10.1016/j.amjmed.2020.02.025>
4. Advisory Committee on Dangerous Pathogens. *The Approved List of Biological Agents* tech. rep. (Health and Safety Executive, 2021).
5. Greenberger, P. et al. Allergic Bronchopulmonary Aspergillosis. *J. Allergy Clin. Immunol. Pract.* **2**, 703–708 (2014). <http://doi.org/10.1016/j.jaip.2014.08.007>
6. Akiyama, K. et al. Allergic Bronchopulmonary Aspergillosis due to *Aspergillus oryzae*. *Chest* **91**, 285–286 (1987). <http://doi.org/10.1378/chest.91.2.285>
7. *Final Risk Assessment of Aspergillus oryzae* tech. rep. (United States Environmental Protection Agency, 1997).
8. Ronning, C. et al. Genomics of *Aspergillus fumigatus*. *Rev. Iberoam. Micol.* **22**, 223–228 (2005). [http://doi.org/10.1016/S1130-1406\(05\)70047-4](http://doi.org/10.1016/S1130-1406(05)70047-4)
9. Rokas, A. & Galagan, J. *Aspergillus nidulans Genome and a Comparative Analysis of Genome Evolution in Aspergillus* (eds Goldman, G. & Osmani, S.) 43–55 (CRC Press, 2007).
10. Galagan, J. et al. Sequencing of *Aspergillus nidulans* and comparative analysis with *A. fumigatus* and *A. oryzae*. *Nature* **438**, 1105–1115 (2005). <http://doi.org/10.1038/nature04341>
11. Watarai, N., Yamamoto, N., Sawada, K. & Yamada, T. Evolution of *Aspergillus oryzae* before and after domestication inferred by large-scale comparative genomic analysis. *DNA Res.* **26**, 465–472 (2019). <http://doi.org/10.1093/dnares/dsz024>
12. Silva, F. et al. Evaluation of antifungal activity of essential oils against potentially mycotoxigenic *Aspergillus flavus* and *Aspergillus parasiticus*. *Rev. Bras. Farmacogn.* **22**, 1002–1010 (2012). <http://doi.org/10.1590/S0102-695X2012005000052>
13. Hammer, K., Carson, C. & Riley, T. Antifungal activity of the components of *Melaleuca alternifolia* (tea tree) oil. *J. Appl. Microbiol.* **95**, 853–860 (2003). <http://doi.org/10.1046/j.1365-2672.2003.02059.x>
14. Paster, N., Menasherov, M., Ravid, U. & Juven, B. Antifungal Activity of Oregano and Thyme Essential Oils Applied as Fumigants Against Fungi Attacking Stored Grain. *J. Food Prot.* **58**, 81–85 (1995). <http://doi.org/10.4315/0362-028X-58.1.81>
15. Duan, W.-Y. et al. Antifungal effects of carvacrol, the main volatile compound in *Origanum vulgare* L. essential oil, against *Aspergillus flavus* in postharvest wheat. *Int. J. Food Microbiol.* **410**, 110514 (2024). <http://doi.org/10.1016/j.ijfoodmicro.2023.110514>
16. Pawar, V. & Thaker, V. In vitro efficacy of 75 essential oils against *Aspergillus niger*. *Mycoses* **49**, 316–323 (2006). <http://doi.org/10.1111/j.1439-0507.2006.01241.x>
17. D'Agostino, M. et al. In vitro antifungal effect of a plant-based product, CIN-102, on antifungal resistant filamentous fungi and their biofilms. *J. Med. Microbiol.* **70**, 285–294 (2021). <http://doi.org/10.1099/jmm.0.001399>
18. D'Agostino, M. et al. Characterisation of the antifungal effects of a plant-based compound, CIN-102, on the main septal filamentous fungi involved in human pathology. *J. Glob. Antimicrob. Resist.* **25**, 171–180 (2021). <http://doi.org/10.1016/j.jgar.2021.03.017>
19. Hamill, R. Amphotericin B Formulations: A Comparative Review of Efficacy and Toxicity. *Drugs* **73**, 919–934 (2013). <http://doi.org/10.1007/s40265-013-0069-4>
20. Zabka, M. & Pavela, R. Antifungal efficacy of some natural phenolic compounds against significant pathogenic and toxigenic filamentous fungi. *Chemosphere* **93**, 1051–1056 (2013). <http://doi.org/10.1016/j.chemosphere.2013.05.076>
21. Vostinaru, O., Heghes, S. C. & Filip, L. in *Essential Oils — Bioactive Compounds, New Perspectives and Applications* (eds) 1–13 (IntechOpen, 2020). <http://doi.org/10.5772/intechopen.91363>
22. Malvessi, E. & Silveira, M. Influence of medium composition and pH on the production of polygalacturonases by *Aspergillus oryzae*. *Brazilian Arch. Biol. Technol.* **47**, 693–702 (2004). <http://doi.org/10.1590/S1516-89132004000500004>
23. Al-Saigh, R. et al. Single-Dose Pharmacodynamics of Amphotericin B against *Aspergillus* Species in an In Vitro Pharmacokinetic/Pharmacodynamic Model. *Antimicrob. Agents Chemother.* **57**, 3713–3718 (2013). <http://doi.org/10.1128/AAC.02484-12>
24. Yun, J.-W. In vitro and in vivo safety studies of cinnamon extract (*Cinnamomum cassia*) on general and genetic toxicology. *Regul. Toxicol. Pharmacol.* **95**, 115–123 (2018). <http://doi.org/10.1016/j.yrtph.2018.02.017>
25. Ye, Z.-W. et al. Progress of nanopreparation technology applied to volatile oil drug delivery systems. *Heliyon* **10**, E24302 (2024). <http://doi.org/10.1016/j.heliyon.2024.e24302>
26. Kothapalli, P. & Vasanthan, M. Lipid-based nanocarriers for enhanced delivery of plant-derived bioactive molecules: a comprehensive review. *Ther. Deliv.* **15**, 135–155 (2024). <http://doi.org/10.4155/tde-2023-0116>
27. Garcia, C. et al. Nanoemulsion delivery systems for enhanced efficacy of antimicrobials and essential oils. *Biomater. Sci.* **10**, 633–653 (2022). <http://doi.org/10.1039/d1bm01537k>
28. Nikkhah, M., Hashemi, M., Habibi Najafi, M. & Farhoosh, R. Synergistic effects of some essential oils against fungal spoilage on pear fruit. *Int. J. Food Microbiol.* **257**, 285–294 (2017). <http://doi.org/10.1016/j.ijfoodmicro.2017.06.021>

Research Article

¹Department of Chemical Engineering, University of Minnesota Duluth, Duluth, MN, USA

Keywords

Ixodes scapularis, artificial membrane feeding, attachment rate, membrane contact, attractant

Email Correspondence

breit172@umn.edu

<https://doi.org/10.26443/msurj.v19i1.219>

©The Authors. This article is published under a CC-BY license: <https://creativecommons.org/licenses/by/4.0/>

Elizabeth Breitbach¹, Victor Lai¹

Elevated Ambient Carbon Dioxide Levels Induce Attraction but Not Attachment of Adult *Ixodes scapularis* in Artificial Membrane Feeding

Abstract

Numerous feeding studies on tick species have explored disease transmission, vector interactions, and acaricide testing. Traditionally, these studies used animals for feeding. However, artificial membrane feeding offers several advantages including increased standardization of experiments, decreased costs, and improved animal welfare. *In vitro* conditions must closely mimic natural environments to promote successful feeding attachment. Kairomones produced by the host are strong stimulants that encourage attachment. An important kairomone detected by ticks is carbon dioxide (CO₂). Previous studies have shown elevated CO₂ levels stimulate host identification and attraction and potentially improve artificial feeding rates in some tick species. The objective of this study was to use an artificial membrane feeding chamber prototype to explore the effects of ambient CO₂ in inducing *Ixodes scapularis* attachment. Differences in attachment rate were explored at an air-typical ambient CO₂ level of 0.04% and an elevated CO₂ level of 4.0%. Tick attachment was not detected in either ambient CO₂ condition during the incubation period, indicating ambient CO₂ does not impact the attachment rate under the presented condition. However, *I. scapularis* contact with the artificial membrane occurred at an increased rate of 0.014 female ticks in contact with the membrane per hour in the elevated CO₂ condition (4%) compared with a rate of 0.01 ticks per hour in the air-typical CO₂ condition (0.04%) ($p=0.048$) suggesting that the ambient CO₂ level affects attraction to the blood but does not directly stimulate attachment of *I. scapularis*.

Introduction

Ticks are responsible for over 95% of vector-borne disease cases in the United States¹. The most prevalent, Lyme disease, is caused by the spirochete bacterium *Borrelia burgdorferi*. When transmitted to humans, *B. burgdorferi* induce inflammatory responses causing systemic symptoms^{2,3}. Most cases of Lyme disease can be treated with antibiotics. However, as a result of late diagnosis or failed antibiotic therapy, chronic manifestations of Lyme disease have been documented^{4,5}. Bacterial dissemination denotes late disease and is characterized by persistent pain and impaired cognitive function⁶.

The black-legged tick, *Ixodes scapularis*, is the vector of several human pathogens, including those causing Lyme disease⁷. The life cycle of *I. scapularis* is approximately two to four years⁸. During this time, ticks cycle through four stages: egg, larva, nymph, and adult. *I. scapularis* are three-host ticks, requiring a blood meal at each life stage⁹. Although literature often states a low risk of transmission for infected adult ticks removed before 72 hours, experimental data using animal models has indicated the transmission time for *B. burgdorferi* is frequently less than 24 hours¹⁰. Expansion of the geographic range of *I. scapularis* and subsequent increase in incidents of Lyme disease over the past two decades makes this an increasing public health concern⁷. As temperatures warm due to climate change, the range of appropriate tick habitat and active periods are expanding¹¹.

Numerous studies on tick species explored disease transmission, vector interactions, and acaricide testing. Traditionally, these studies used animals for feeding. Currently, animal-derived or artificial membranes have replaced these methods and increased standardization of experiments, de-

creased costs, and improved animal welfare¹². Early studies used membranes constructed from thin slices of cattle, rabbit, or mouse skin. However, these membranes were prone to rapid degradation¹². The first report of voluntary feeding of ixodid ticks on an artificial membrane was the use of modified Baudruche membrane made from processed animal intestine to study the feeding activity of *Rhipicephalus microplus* ticks¹³. A comparison on feeding and survival of *R. microplus* on cattle versus through a Baudruche membrane showed that membrane conditions were capable of facilitating feeding outcomes comparable to natural conditions¹⁴. Another study demonstrated efficient artificial feeding of the *Ornithodoros coriaceus* tick through a Parafilm membrane using various stimulants, including covering the membrane with animal hair and an optimal feeding temperature of 37-39 °C. Bovine red blood cells, fetal calf serum, and glutathione solutions promoted high engorgement rates¹⁵.

Many current studies involving artificial tick feeding find success with silicone membranes. However, *in vitro* conditions must incorporate critical stimuli present in natural environments to promote attachment and subsequent feeding¹⁶. Attractants continue to be explored for optimization of successful feeding using membranes. Host hair is an important stimulus as it provides both olfactory and tactile stimuli¹⁶. Volatiles and glandular secretions also assist in recognition of the host. These cues are unique to different tick species and their choice of hosts. For example, *I. scapularis* were found to exhibit an arrestant response to secretions associated with the glands of the white-tailed deer¹⁷. Ticks also release pheromones to facilitate aggregation (when ticks gather on a host in large numbers) and mating. Multiple reproductive pheromones have been identified in metastriate ticks, such as *Amblyomma* and *Dermacentor* species, which engage in on-host aggregative mating¹⁸. For example, attraction-aggregation-attachment

pheromone (AAAP) is produced by male *Amblyomma* ticks to attract unfed males and females¹⁹. Prostriate ticks, including *I. scapularis*, use nest-based mating strategies, with no consistent identification of volatile sex pheromones¹⁸. However, evidence of assembly pheromones have been documented in *I. scapularis*²⁰.

Haller's organ, a chemosensory structure located on the front legs of ticks, serves as a primary means of receiving host cues including heat, odors, and CO₂²¹. Due to the ability of ticks to detect radiant heat, accepted optimal membranes temperature tends to be 37 °C, the typical body temperature of hosts. Kairomones produced by the host are strong attractants that encourage attachment. An important kairomone detected by ticks is CO₂. In the 1950s, several studies found CO₂ to be a stimulant or attractant for bloodsucking arthropods such as mosquitoes, mites, and fleas²²⁻²⁴. In the following decade, similar responses were shown for certain tick species²⁵. CO₂ generated from dry ice has since been used to attract and subsequently capture ticks. Increased CO₂ concentrations have been found to stimulate behavioral responses in tick species *A. americanum* and *D. variabilis* at rates as low as 9 ppm above the average ambient level²⁶. Elevated CO₂ levels have also been shown to improve feeding success in some tick species. For example, Krull et al. found a significant increase in engorgement mass and fertility of female *D. reticulatus* ticks at 5% CO₂ compared to ambient CO₂ levels²⁷. Recent research has indicated that CO₂ activates *I. scapularis* and initiates responses that resemble host-seeking²⁸. This study found that *I. scapularis* responded to CO₂ stimuli even with a disabled Haller's organ. Further research is needed to understand the relationship between CO₂ and *I. scapularis* behavior, attraction, and attachment.

The objective of this study was to use an artificial membrane feeding chamber prototype to explore the effects of ambient and elevated CO₂ levels as a stimulant to induce *I. scapularis* attachment. Optimizing feeding chamber parameters to allow for successful artificial feeding is required to set the stage for further experiments exploring the transmission of *B. burgdorferi* in these settings.

Methods

Membrane Optimization

The artificial membrane feeding technique used in this study was modified from Oliver et al. (2015) and based on methods developed by Kröber and Guerin (2007)^{29,30}. Microscope lens paper (Fisher Scientific, Waltham, MA) was infiltrated with silicone rubber to produce a membrane mimicking the epithelial layer of skin. Lens paper was taped on a smooth sheet of Saran® wrap. Parts A and B of Ecoflex 00-30 (Smooth-On, Macungie, PA) were mixed in a 1:1 ratio to a total volume of 10 mL. Hexane was added to the silicone to temporarily thin the solution and ease the spread over the lens paper. The solution was mixed vigorously for three minutes per the manufacturer's instructions. The silicone solution was evenly spread over the lens paper and allowed to fully saturate the paper. Excess silicone was scraped off with a plastic kitchen scraper and membranes were allowed to cure for 24 hours. Each lens paper produced membranes for six chambers (Figure 1A).

Membrane thickness was measured using two different points on each membrane with a micrometer. Optimal membrane thickness is between 50 and 100 µm for adult *I. scapularis* as this allows for successful access of the hypostome to the blood through the membrane²⁹. Ecoflex silicone is available in different shore hardness (00-XX, where XX represents the shore hardness), which indicates the resistance to indentation. Silicone with higher shore hardness produces thicker membranes, while those with lower shore hardness produce thinner membranes. Ecoflex 00-20 resulted in membranes with thickness consistently less than 50 µm, while Ecoflex

00-30 produced membranes typically between 50 and 100 µm. Several factors were investigated to reduce variation in membrane thickness, including shore hardness of the silicone, saturation time, and amount of hexane added to solution.

A two factorial design was conducted to determine if the saturation time (8, 12 min) and the amount of hexane added to the silicone to thin the solution (1.5, 1.75, 2.0 mL) would reduce variation in membrane thickness while still producing membranes in the optimized thickness range. One lens paper was used for each condition. All conditions used Ecoflex 00-30. Each membrane was cut into six equivalent squares signified in Figure 1A as the "Region." The thickness of the membrane was measured at two points in the center of the square.

Damaged membranes and membranes with thickness below or above the optimal range were discarded. Before using these membranes to construct the feeding chambers, they were pressed with hands to reduce tackiness.

Chamber Assembly

Feeding chambers were constructed by cutting a 1.5-inch section of transparent vinyl tubing (outer diameter = 1.5 inches, inner diameter = 1.25 inches) and placing them in individual wells of a 6-well plate. A rubber band encircling the tubing determined the depth at which the feed chamber would be submerged in the blood. This prevented the chamber from being flush against the bottom of the well plate, limiting access to blood (Figure 1B). Chambers were attached to the membranes using All Purpose Crazy Glue®. The adhesive was applied to the end of the chamber and the membrane was centered over the chamber. Tweezers were pressed along the edge to ensure a constant seal around the entire edge of the chamber. The chambers were allowed to dry for 24 hours. Excess membrane was carefully removed using a scalpel. Chambers were tested for damage by adding a 5 mL solution of water and food coloring. Chambers that demonstrated leaks were discarded.

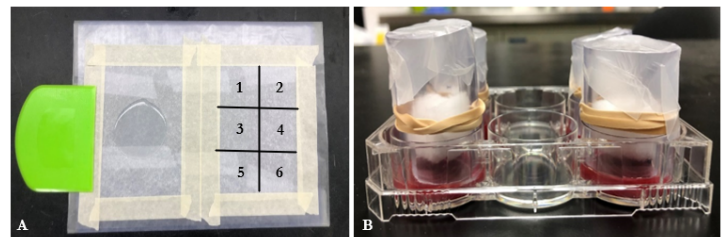


Figure 1. Infiltration of microscope lens paper with silicone (A) and artificial feeding chamber set-up (B). Cotton wool was placed in the chamber for clarity in the image and was not used during the testing process.

I. scapularis Maintenance and Feeding

Four mL of sterile, mechanically defibrinated bovine blood (Hemostat Laboratories, Dixon, CA) and 90 µL of ampicillin/streptomycin solution (Gibco, Thermo Fisher Scientific Inc, Waltham, MA) was added to the four wells of a six well plate. The major component of the aggregation attachment pheromone, 2-nitrophenol (Sigma-Aldrich, Merck KGaA, Darmstadt, Germany), was dissolved in hexane to a final concentration of 10 mM³¹. Each well was supplemented with 4.5 µL of the 2-nitrophenol solution to encourage attachment. Additional attractants described in literature such as tick frass or deer hair extract were not used due to resource constraints.

Feeding chambers were placed into the wells to ensure direct contact between the membrane and blood. The well plate was placed in the NAPCO Automatic CO₂ Incubator (Series 5400 11V Model) set at 37 °C and the

designated ambient CO₂ level. The humidity in the incubator was approximately 100%. Attachment rate was evaluated at an assumed air-typical ambient CO₂ level of 0.04% and an elevated ambient CO₂ level of 4.0%. Four female and four male ticks were placed in each feeding chamber for the air typical CO₂ condition and five female and five male ticks were placed in each feeding chamber for the elevated CO₂ condition. New ticks were used for each treatment. *I. scapularis* adults, obtained from Atlanta CDC, were unfed, free of known human pathogens, and approximately 4 months post-molted. Ticks were held in air equilibrated with saturated K₂HPO₄ with relative humidity around 96% before transfer to the feeding chambers. Two sheets of parafilm sealed the top of the chamber to prevent ticks from escaping. A photoperiod of 16:8 (light:darkness) hours was implemented in the incubator to mimic outdoor conditions.

Feeding chambers were removed every 8 hours to check for evidence of attachment. Attachment was detected through visual assessment of the hypostome piercing the membrane and supported by a subsequent increase in body diameter as feeding occurred. Images of membranes were taken using the Nikon D 7500 digital camera with the AF-S DX Micro NIKKOR 40 mm lens (Nikon, Tokyo, Japan). *I. scapularis* that climbed up the sides of the chambers were returned to the surface of the membrane. Every 12 hours, feeding chambers were removed, rinsed with Milli-q water, and submerged in amphotericin B (Cytiva, Thermo Fisher Scientific Inc, Waltham, MA) for three minutes to prevent fungal contamination. Chambers were placed in new six well plates with fresh blood. Trials were conducted for 48 hours or until membrane failure (i.e., when tears or leakage occurred).

Results

Membrane Optimization

Great variation in thickness was seen in different lens papers and even in different membranes on the same lens paper. Therefore, saturation time and amount of hexane added to thin the solution were explored as potential parameters to reliably produce membranes in the optimized thickness range of 50 to 100 μm. A two-way ANOVA was performed to analyze the effect of saturation time (8, 12 min) and amount of hexane added to the silicone (1.5, 1.75, 2.0 mL) on membrane thickness. There was not a statistically significant interaction between the effects of saturation time and amount of hexane ($F(2, 15)=0.6672, p=0.53$). Simple main effects analysis showed that saturation time did not have a statistically significant effect on membrane thickness ($p=0.58$). Simple main effects analysis showed that amount of hexane did have a statistically significant effect on membrane thickness ($p=0.0009$). Upon further analysis, adding 1.75 mL hexane to the solution more reliably produces membranes below 50 μm (Mean, $\bar{x} = 26.67 \mu\text{m} \pm 5.27 \mu\text{m}$ for 8 minutes, $\bar{x} = 36.83 \mu\text{m} \pm 3.50 \mu\text{m}$ for 12 minutes) when compared to 1.5 mL hexane added ($\bar{x} = 67.31 \mu\text{m} \pm 19.06 \mu\text{m}$ for 8 minutes, $\bar{x} = 75.78 \mu\text{m} \pm 24.65 \mu\text{m}$ for 12 minutes) and 2.0 mL hexane added ($\bar{x} = 70.70 \mu\text{m} \pm 30.16 \mu\text{m}$ for 8 minutes, $\bar{x} = 63.50 \mu\text{m} \pm 27.96 \mu\text{m}$ for 12 minutes).

I. scapularis Attachment Rate

Differences in attachment rate were explored at an air-typical ambient CO₂ level of 0.04% and an elevated CO₂ level of 4%. Neither ambient CO₂ condition induced visible attachment of *I. scapularis* during the 48-hour incubation period. However, a direct relationship was seen between percent of female *I. scapularis* in contact with the membrane (i.e., on the membrane surface and not on the chamber walls) and incubation time in both CO₂ conditions (Figure 2 and Figure 3). A t-test comparing the slopes of the two regression lines in Figure 3 was statistically significant ($t_{(10)}=2.25, p=0.048$).

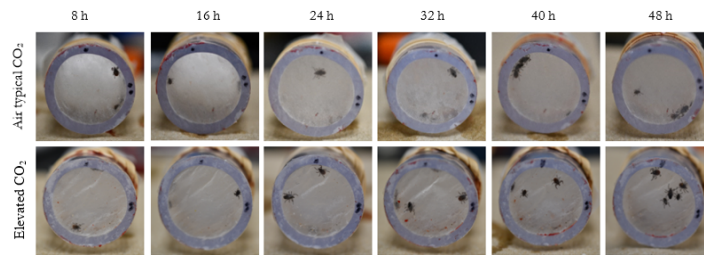


Figure 2. Progression of *I. scapularis* in contact with the membrane over the incubation period at 8, 16, 24, 32, 40, and 48 hour intervals (left to right) in a singular feeding chamber. Air typical CO₂ condition (top) and elevated CO₂ condition (bottom) are shown.

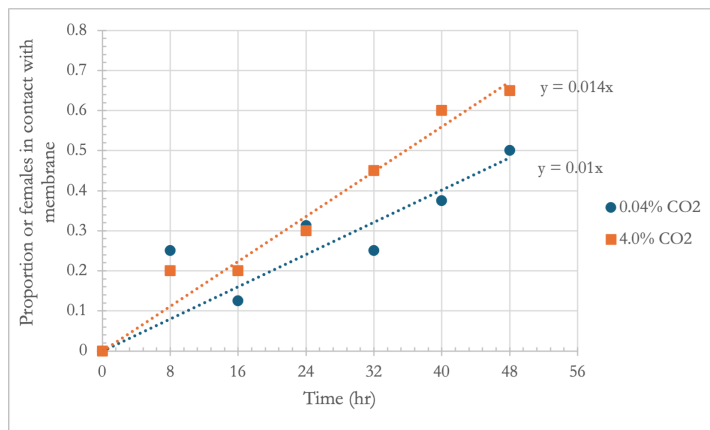


Figure 3. Proportion of females in contact with the membrane over a 48-hour incubation period for both air-typical CO₂ levels (0.04%) and elevated ambient CO₂ levels (4.0%). $n=20$ females at each CO₂ level from pooling all female ticks from chambers at the same CO₂ level. A significant difference between the slopes suggests that an elevated CO₂ level promoted tick contact with the membrane over time.

Discussion

Membrane Optimization

Membrane thickness must be between 50 and 100 μm for adult *I. scapularis* to successfully access the blood through the membrane via the hypostome. Consistency in membrane thickness is thus essential in standardizing experiments. Saturation time (8, 12 min) and the amount of hexane added to thin the silicone solution (1.5, 1.75, 2.0 mL) were explored as potential factors to reduce variability. The amount of hexane was shown to have a statistically significant effect on membrane thickness. Specifically, adding 1.75 mL hexane to the solution more reliably produces membranes below 50 μm. Adding 1.5 and 2.0 mL hexane produced thicker membranes with greater variability. Therefore, 1.75 mL of hexane appears to be the optimal volume to achieve the required membrane thickness and consistency. The saturation time was not found to have a statistically significant effect on membrane thickness either alone or in conjunction with hexane volume.

I. scapularis Attachment Rate

I. scapularis attachment to the artificial membrane was not detected in either ambient CO₂ condition during the incubation period, indicating ambient CO₂ does not impact the attachment rate under the presented condition. However, *I. scapularis* contact with the artificial membrane occurred at an increased rate of 0.014 female ticks in contact with the membrane per hour in the elevated CO₂ condition (4%) compared with a rate of 0.01 ticks per hour in the air-typical CO₂ condition (0.04%) ($p=0.048$) suggesting that the ambient CO₂ level affects attraction to the blood but does not directly stimulate attachment of *I. scapularis*. This phenomenon is consistent with

several previous studies in various arachnids species that demonstrate the ability of ticks to sense and react to CO₂ output from potential hosts. For example, adult *A. americanum* and *D. variabilis* demonstrated behavioral responses including questing, initial movement, and activity rate, to CO₂ concentrations as low as 9 ppm above the average ambient background²⁶. Another study found CO₂ to consistently attract the highest number of host-seeking ticks (*A. americanum* and *D. variabilis*) when compared to several semiochemicals³². There has also been some suggestion that CO₂ must be present in combination with certain pheromones for successful attraction of ticks to the host. Maranga et al. studied the response of *A. variegatum* ticks to AAAP at various distances in the presence or absence of elevated CO₂. A significant majority (up to 90%) of ticks released were attracted to AAAP in the presence of CO₂ while CO₂ alone was unattractive³³. Although, the effects of CO₂ on metastriate ticks are well documented, these findings cannot be applied to the *Ixodes* genus where less is known about stimulants that encourage aggregation, mating, and feeding. Recent research has shown CO₂ is a potent stimulant for *I. scapularis* in regard to walking behavior²⁸. In this study, there was no clear concentration preference. Ultimately, the presence of CO₂ has been shown to be essential in the tick life cycle from questing to feeding. However, the exact mechanism is not entirely understood.

Male ticks did not appear to engage in attachment or attraction. This is unsurprising as the genus *Ixodes* are prostriate ticks in which copulation can occur off the host and unfed females can be inseminated prior to host attachment³⁴. Although males can be found on hosts, they do not require an adult bloodmeal³⁵. Therefore, they were not the focus of our study. It is also important to note that our results are limited to snapshots at different time points throughout the experiment. Whether the ticks moved about randomly in between data collection or were more arrested on the membrane over time is unclear and warrants further study using a camera with live-recording capabilities. Another consideration is that the effects of CO₂ were explored in an ambient setting rather than emitted directly from the blood. This suggests that increased ambient CO₂ levels facilitate attraction to the blood via an indirect mechanism.

Possible explanations for the lack of attachment include the following. The rapid failure of the membrane, resulting in leakage of blood into the chamber, and contamination with fungal growth only allowed for potential attachment and feeding window of 48 hours. It is also possible that attachment was accomplished but substantial feeding with an increase in body diameter was not yet achieved. This prospect is supported by previous studies that have established several days are required for *I. scapularis* attachment and feeding to reach fulfillment. For example, a study on in vitro feeding of *I. scapularis* adults found 45% attachment rate with 19 of the 49 attached ticks engorged after 13 days³⁶. Oliver et al. revealed a minimum of three days were required for *I. scapularis* nymph to reach engorgement²⁹. In that study, between 30-50% of female adult *I. scapularis* and approximately 50% of nymphs completed engorgement when given seven days to feed²⁹. Another concern is the small number of ticks used in the study, as well as the limitation of a single trial. As noted above, a substantial proportion of ticks fail to successfully feed using artificial membrane techniques. This phenomenon may be compounded by a low sample size. Therefore, our results require careful interpretation and should be reanalyzed with an increased number of ticks and trials. Nonetheless, these results show a promising prototype of an artificial membrane feeding chamber to study tick attachment and feeding behavior under different conditions once further improvements to the design and fabrication of the chambers are successfully created to allow the experiments to proceed beyond 48 hours. Ideally, chambers would function for over one week in order to visualize attachment and subsequent feeding of ticks.

In conclusion, *I. scapularis* attachment to the artificial membrane was not affected by ambient CO₂ concentrations. However, ambient carbon dioxide levels appeared to affect attraction to the blood as suggested by an in-

crease in tick contact with the membrane over the incubation period as well as a higher percentage of ticks in contact with the membrane in the elevated CO₂ condition compared with the air-typical CO₂ condition. Multiple studies have successfully implemented membrane feeding through additives to the blood, as well as stimulants present on the membrane. Potential factors that could be added to our experimental set-up include incorporating tactile and olfactory stimuli such as the addition of cow hair extract, deer hair extract, or tick frass extract to the membrane^{29,30,37}. Further research should be conducted to explore the stimulants which promote attachment and feeding in *I. scapularis*.

Acknowledgements

This work was funded by the University of Minnesota Undergraduate Research Opportunities Program (UROP). The authors thank Dr. Benjamin Clarke, Dr. David Schimpf, Shannon RedBrook, and Dr. Jonathan Oliver for their support and advice during the entirety of the project.

References

- Rochlin, I. & Toledo, A. Emerging tick-borne pathogens of public health importance: a mini-review. *J. Med. Microbiol.* **69**, 473–518 (2020). <https://doi.org/10.1099/jmm.0.001206>
- Coburn, J. et al. Lyme disease pathogenesis. *Curr. Issues. Mol. Biol.* **42**, 473–518 (2021). <https://doi.org/10.21775/cimb.042.473>
- Murray, T. S. & Shapiro, E. D. Lyme disease. *Clin. Lab. Med.* **30**, 311–328 (2010). <https://doi.org/10.1016/j.cl.2010.01.003>
- Centers for Disease Control and Prevention. Chronic Symptoms and Lyme disease (2010); <https://www.cdc.gov/lyme/postlds/index.html>
- Shor, S. et al. Chronic Lyme disease: An evidence-based definition by the ILADS Working Group. *J. Antibiot.* **8**, 269 (2019). <https://doi.org/10.3390/antibiotics80402693>
- Maloney, E. L. Controversies in persistent (chronic) Lyme disease. *J. Infus. Nurs.* **39**, 369–375 (2016). <https://doi.org/10.1097/nan.0000000000000195>
- Eisen, R. J. & Eisen, L. The blacklegged tick, *Ixodes scapularis*: An increasing public health concern. *Trends. Parasitol.* **34**, 295–309 (2018). <https://doi.org/10.1016/j.pt.2017.12.006>
- Gulia-Nuss, M. et al. Genomic insights into the *Ixodes scapularis* tick vector of Lyme disease. *Nat. Commun.* **7**, 10507 (2016). <https://doi.org/10.1038/ncomms10507>
- Tilly, K., Rosa, P. A. & Stewart, P. E. Biology of infection with *Borrelia burgdorferi*. *Infect. Dis. Clin. North.* **22**, 217–234 (2016). <https://doi.org/10.1016/j.idc.2007.12.013>
- Cook, M. J. Lyme borreliosis: a review of data on transmission time after tick attachment. *Int. J. Gen. Med.* **18**, 1–8 (2014). <https://doi.org/10.2147/IJGM.S73791>
- United State Environmental Protection Agency. Climate change indicators: Lyme disease (2021); <https://www.epa.gov/climate-indicators/climate-change-indicators-lyme-disease>
- Waladde, S. M., Young, A. S. & Morzaria, S. P. Artificial feeding of ixodid ticks. *Parasitol. Today* **12**, 272–278 (1996). [https://doi.org/10.1016/0169-4758\(96\)10027-2](https://doi.org/10.1016/0169-4758(96)10027-2)
- Waladde, S. M., Kemp, D. H. & Rice, M. J. Feeding electrograms and fluid uptake measurements of cattle tick *Boophilus Microplus* attached on artificial membranes. *Int. J. Parasitol.* **9**, 89–95 (1978). [https://doi.org/10.1016/0020-7519\(79\)90096-1](https://doi.org/10.1016/0020-7519(79)90096-1)

14. Kemp, D. H., Agdebe, R. I. S., Johnston, L. A. Y. & Gough, J. M. Immunization of cattle against *Boophilus microplus* using extracts derived from adult female ticks: feeding and survival of the parasite on vaccinated cattle. *Int. J. Parasitol.* **16**, 115–20 (1986). [https://doi.org/10.1016/0020-7519\(86\)90096-2](https://doi.org/10.1016/0020-7519(86)90096-2)
15. Hokama, Y., Lane, R. S. & Howarth, J. A. Maintenance of adult and nymphal *Ornithodoros coriaceus* (Acari: Argasidae) by artificial feeding through a parafilm membrane. *J. Med. Entomol.* **24**, 319–323 (1987). <https://doi.org/10.1093/jmedent/24.3.319>
16. González, J., Bickerton, M. & Toledo, A. Applications of artificial membrane feeding for ixodid ticks. *Acta Trop.* **215**, 105818 (2021). <https://doi.org/10.1016/j.actatropica.2020.105818>
17. Carroll, J. F., Mills, G. D. & Schmidtman, E. T. Field and laboratory responses of adult *Ixodes scapularis* (Acari: Ixodidae) to kairomones produced by white-tailed deer. *J. Med. Entomol.* **33**, 640–644 (1996). <https://doi.org/10.1093/jmedent/33.4.640>
18. Carr, A. L., Sonenshine, D. E., Strider Jr, J. B. & Roe, R. M. Evidence of female sex pheromones and characterization of the cuticular lipids of unfed, adult male versus female blacklegged ticks, *Ixodes scapularis*. *Exp. Appl. Acarol.* **68**, 519–538 (2016). <https://doi.org/10.1007/s10493-015-0009-y>
19. Sonenshine, D. E. Tick pheromones and their use in tick control. *Annu. Rev. Entomol.* **51**, 557–580 (2006). <https://doi.org/10.1146/annurev.ento.51.110104.151150>
20. Allan, S. A. & Sonenshine, D. E. Evidence of an assembly pheromone in the black-legged deer tick, *Ixodes scapularis*. *J. Chem. Ecol.* **28**, 15–27 (2002). <https://doi.org/10.1023/A:1013554517148>
21. Carr, A. L. & Salgado, V. L. Ticks home in on body heat: A new understanding of Haller's organ and repellent action. *PLoS One.* **14**, e0221659 (2019). <https://doi.org/10.1371/journal.pone.0221659>
22. Brown, A. W. A. Studies of the responses of the female *Aedes* mosquito. Part IV. Field experiments on Canadian species. *Bull. Entomol.* **42**, 575–582 (1951). <https://doi.org/10.1017/S0007485300028984>
23. Sasa, M. & Wakasugi, M. Studies on the Effect of Carbon Dioxide as the Stimulant on the Tropical Rat Mite, *Bdellonyssus bacoti* (Hirst, 1913). *Jpn. J. Exp. Med.* **27**, 207–215 (1957).
24. Sasa, M. Notes on the effect of carbon dioxide in the breath as the stimulant on the flea *Ctenocephalides canis* (Curtis, 1826). *Jpn. J. Exp. Med.* **27**, 401–410 (1957).
25. Garcia, R. Carbon Dioxide as an Attractant for Certain Ticks (Acarina: Argasidae and Ixodidae). *Ann. Entomol. Soc. Am.* **55**, 605–606 (1962). <https://doi.org/10.1093/aesa/55.5.6054>
26. Perritt, D. W., Couger, G. & Barker, R. W. Computer-controlled olfactometer system for studying behavioral responses of ticks to carbon dioxide. *J. Med. Entomol.* **30**, 571–578 (1993). <https://doi.org/10.1093/jmedent/30.3.571>
27. Krull, C., Bohme, B., Clausen, P. H. & Nijhof, A. M. Optimization of an artificial tick feeding assay for *Dermacentor reticulatus*. *Parasites & Vectors* **10**, 60–67 (1993). <https://doi.org/10.1186/s13071-017-2000-4>
28. Städele, C. The black-legged tick *Ixodes scapularis* detects CO₂ without the Haller's organ. *J. Exp. Biol.*, jeb.246874 (2024). <https://doi.org/10.1242/jeb.246874>
29. Oliver, D. J. et al. Infection of immature *Ixodes scapularis* by membrane feeding. *J. Med. Entomol.* **53**, 409–415 (2016). <https://doi.org/10.1093/jme/tjv241>
30. Kröber, T. & Guerin, P. M. An in vitro feeding assay to test acaricides for control of hard ticks. *Pest. Manag. Sci.* **63**, 17–22 (2007). <https://doi.org/10.1002/ps.1293>
31. Soares, S. F. & Borges, L. M. F. Electrophysiological responses of the olfactory receptors of the tick *Amblyomma cajennense* to host-related and tick pheromone-related synthetic compounds. *Acta Trop.* **124**, 192–198 (2012). <https://doi.org/10.1016/j.actatropica.2012.08.007>
32. Carr, A. L. et al. Responses of *Amblyomma americanum* and *Dermacentor variabilis* to odorants that attract haematophagous insects. *Med. Vet. Entomol.* **27**, 86–95 (2013). <https://doi.org/10.1111/j.1365-2915.2012.01024.x>
33. Maranga, R. O., Hassanali, A., Kaaya, G. P. & Mueke, J. M. Attraction of *Amblyomma variegatum* (ticks) to the attraction-aggregation-attachment-pheromone with or without carbon dioxide. *Exp. Appl. Acarol.* **29**, 121–130 (2003). <https://doi.org/10.1023/a:1024265529030>
34. Kiszewski, A. E., Matuschka, F.-R. & Spielman, A. Mating strategies and spermiogenesis in Ixodid ticks. *Annu. Rev. Entomol.* **46**, 167–182 (2001). <https://doi.org/10.1146/annurev.ento.46.1.167>
35. Ioffe-Uspensky, I. & Uspensky, I. The influence of preprandial insemination on feeding and oviposition of *Ixodes persulcatus* females (Acari: Ixodidae) and some thoughts concerning mating strategies in ticks of the genus *Ixodes*. *Ticks Tick Borne Dis.* **8**, 866–871 (2017). <https://doi.org/10.1016/j.ttbdis.2017.07.003>
36. Andrade, J. J., Xu, G. & Rich, S. M. A silicone membrane for in vitro feeding of *Ixodes scapularis* (Ixodida: Ixodidae). *J. Med. Entomol.* **51**, 878–879 (2017). <https://doi.org/10.1603/ME13180>
37. Koci, J., Bernard, Q., Yang, X. & Pal, U. *Borrelia burgdorferi* surface protein Lmp1 facilitates pathogen dissemination through ticks as studied by an artificial membrane feeding system. *Sci. Rep.* **51**, 1990 (2018). <https://doi.org/10.1038/s41598-018-20208-4>

A Replication Study to Evaluate the Effects of Awe on Humility

Research Article

¹Department of Psychology,
McGill University, Montréal,
QC, Canada

Keywords

Replication, humility, awe,
depression

Email Correspondence

alexandra.bertrand@mail.mcgill.ca

<https://doi.org/10.26443/msurj.v19i1.231>

©The Authors. This article is
published under a CC-BY license:
<https://creativecommons.org/licenses/by/4.0/>

Abstract

This paper replicates Stellar and colleagues' 2018 study involving an experimental manipulation of awe using standardized video induction, as well as proposing and testing out an additional hypothesis. The previous study hypothesized that watching an awe-inducing video would lead participants to disclose fewer strengths when writing about their self-perceived strengths and weaknesses. In addition to the replication, we hypothesized that participants with higher scores of depressive symptomatology (DS) would list fewer strengths due to diminished self-concept and self-efficacy. Ninety-four undergraduate psychology students were recruited from McGill University ranging from 18 to 35 years of age. Participants were randomly assigned to either the awe-inducing or neutral video condition and then filled out measures of humility, emotional reactions, and DS. In contradiction with the original study, participants in the awe condition and the neutral condition did not significantly differ in their ratio of disclosed strengths to weaknesses, therefore no significant correlations were found between awe and humility or humility and depression. Additionally, results indicated that participants with greater DS did not list fewer strengths than those scoring lower on the Center for Epidemiologic Studies Depression Scale (CES-D). We were unable to directly replicate the original study and thus rejected our alternate hypothesis. This study had various potential limitations, among which are the possibilities of self-report bias, issues regarding convenience sampling, and bias due to time constraints. The current study advances the literature by examining depression as it relates to awe and humility. Further research is needed to differentiate lab-induced awe from natural experiences of awe and to identify possible moderating factors on humility.

Introduction

According to Lee & Ashton (2005, in Stellar et al., 2018), humility involves a stable, sincere, and non-restrictive view of one's self, in conjunction with a recognition of the value of things external to the self¹. Humility is a foundational virtue that acts as a counterforce to self-centered tendencies like entitlement, arrogance, and narcissism, and is essential to living in social groups¹. Despite this significance, little is known about how this virtue can be bolstered¹. To address this gap, Stellar and colleagues posited that humility could be influenced by experiences of awe, such as encounters with forces or situations that are immeasurable and cerebrally profound. And through this encounter, awe has the capacity to induce a dramatic shift in an individual's self-concept, characterized by a reduced sense of self¹. In other words, experiencing awe would generate greater humility. Across five studies, Stellar and colleagues aimed to explore the connection between awe and humility, assessing whether momentary experience of awe could promote humility by using an appraisal-tendency framework to clarify the underlying process behind this effect¹.

This paper focuses on a replication of Stellar and colleagues' third study, which involved an experimental manipulation of awe using standardized video induction, as well as proposing and testing out a new additional hypothesis¹. In the original study, humility was evaluated as a behavioural measure, such that greater humility was operationalized as a more balanced presentation of one's own strengths and weaknesses to other people, such as less bragging or self-promotion¹. Furthermore, the hypothesis for this investigation posited that, in contrast to a neutral control condition (i.e., a video about fence building), momentary experiences of awe induced by a video illustrating the universe expanding would lead to a more equitable disclosure of personal strengths and weaknesses¹. This hypothesis is important as it could be a first step towards eventually using inductions of

awe to promote humility in people.

In alignment with their aforementioned hypothesis, the induction of awe prompted participants to exhibit greater humility, as manifested in their disclosure of fewer personal strengths than participants in the neutral condition¹. However, there was no effect of condition on the number of weaknesses listed by participants¹. Given that the experimental condition evoked more happiness and awe, a multiple regression analysis was conducted using awe and happiness as predictors of humility¹. The original results revealed that neither awe nor happiness were significant predictors, indicating the inability to establish the distinctive impact of awe, as self-reports of this emotion did not forecast levels of humility¹.

Additional Hypothesis

A recent systematic review found that the mean prevalence of depression in university students to be 30.6%, higher than the mean of 9% found in the general population (SD=3%). Thus, due to the inconclusive findings of the original study, as well as the results from the systematic review regarding our participant sample, we hypothesize that depression levels might mediate humility (more so than awe). Accordingly, we consider the possibility that depression, as a potential confound, could have influenced participants' written self-evaluation, since having a negative view of oneself, or a negative self-schema, has been reliably linked with depressive symptomatology (DS)²⁻⁵. Hence, our proposed alternative hypothesis is that participants with greater depressive symptomatology, as measured by higher scores on the Center for Epidemiologic Studies Depression Scale (CES-D), will report fewer strengths and thus greater humility than participants with less DS, in both control and experimental conditions. To test this alternate hypothesis, we first replicated the original third study by Stellar and col-

leagues and then had participants fill out the CES-D. Finally, our hypothesis is relevant to the original conclusions of Stellar et al. since we believe listing fewer strengths may be mediated by self-diminishment that is linked to participants' DS rather than humility, since self-diminishment in depression is thought to be related to negative self-concept, whereas humility is usually concerned with a more neutral view of yourself, a lack of pride, or not considering yourself to be "better than others".

Methods

Participants

We attempted to recruit 104 participants for the study, as the original study we were replicating, Study 3 of Stellar et al. (2018), had 104 participants recruited online, with a final sample of 85 participants. Recruitment was conducted through Sona Systems, a research platform affiliated with McGill University in which participants were presented with a general outline of the study and its various requirements. Due to limitations in the student study pool, our participant sample consisted of 94 undergraduate psychology students recruited from McGill University ranging from 18 to 35 years of age. Participant gender and age were not self-reported during the study procedure, so we are unable to make any inferences about differences between ours and the original study's demographic samples. The participants voluntarily chose to participate for 0.5% psychology course credit as an incentive, which could be applied towards a psychology course that they were registered in. We were one of two research teams concurrently replicating the Stellar et al. (2018) study, therefore participation restrictions were implemented as participants who took part in this study could not participate in the other replication of the original study, and vice versa, to reduce validity issues.

Procedure

Data was collected from November 2nd to November 17th, 2023. Participants arrived at the lab and were provided with brief instructions on where to sit and how to proceed with the study. Using a between-subjects post-test experimental design, participants were randomly assigned to either the experimental (awe) or control (neutral) conditions. Participants in the awe condition watched a two-minute video meant to depict the expansiveness of the universe as it slowly zoomed out from planet Earth and exposed more and more of the universe. Participants in the neutral condition watched a two-minute instructional video on how to build a fence. In previous mood-induction-based studies, this video was not shown to elicit strong emotions in participants other than relaxation and calm⁶.

Measures

Participants were instructed to watch a two-minute video viewed on a desktop computer screen in a university computer laboratory. As multiple participants completed the study in the lab at the same time, alternating computers were used to seat participants, allowing for a minimum distance of 2 meters between them. Participants were also provided with headphones to hear the audio from the video. The same videos from YouTube used by the original study were used in this replication study. Once the video ended, they were automatically directed to a new page of the survey where they were instructed to write about their strengths, followed by their weaknesses, for two minutes. They were instructed to write as though they were discussing their qualities with a person they just met, to standardize the response type across participants as well as augment the interactive nature of the online setting to be more in line with the other 4 studies of the original paper, all of which were conducted in-person¹. A timer was visible to

participants to show them how much time they had left. Once the timer ended, the survey automatically advanced to a new page where the participants were instructed to report how much awe, happiness, fear, wonder, and amazement they felt while watching the video. They scored their feelings on a scale of 1 (not at all) to 7 (very much). They were then asked questions meant to address their comprehension and completion of this portion of the study, such as explaining what the video was about, what they believed the study to be about, and if the video loaded properly and played all the way through.

Participants were then prompted to complete the Center for Epidemiologic Studies Depression Scale (CES-D) to measure their level of depressive symptomatology over the last week. The CES-D is a self-report scale measuring depressive symptoms that is meant to be used in the general population. The measure consists of questions selected to identify how often participants experienced depressive symptoms in the past week⁷. Participants were presented with statements such as "I felt fearful", "I was happy", "I was bothered by things that usually don't bother me", and "I enjoyed life" and were asked to indicate how often they felt such a way in the last week using a Likert Scale from *Rarely or none of the time (less than 1 day)* to *Most or all of the time (3-4 days)*. Higher scores on the measure indicated more depressive symptoms, with scores of 16 or higher being indicative of a risk for clinical depression⁷. Though various shortened versions exist (for example, a 10-item version), the complete 20-item scale was used on participants (See Appendix A) as it only requires an average of five minutes to complete by the general population who do not suffer from cognitive impairments⁸.

Consistent with Stellar et al., once data was collected, two coders were assigned to read participants' responses and count the number of strengths and weaknesses stated¹. The original study did not make any mention of what coding rules were followed by raters during the analysis. Thus, prior to the start of coding, a codebook was established. Various ideas and issues were established prior to coding and subsequently translated into formal rules that coders were to follow while rating the number of strengths and weaknesses written by participants (See Appendix B). Coders were strictly informed not to communicate once coding began. Discussion about participants' listed strengths and weaknesses was to be avoided both between and within groups of raters to ensure no rater influenced another and biased the results. The average of the two coders was taken and considered as the number of strengths and weaknesses listed by participants. Since participant strengths and weaknesses were written free-form and coded by rater pairs, interrater reliability was examined for each rater pair on raw strength and weakness counts. Intraclass correlation coefficients measuring agreement between rater pairs showed excellent reliability or acceptable agreement for all examined response pairs save one, with the divergent pair showing moderate reliability and tentatively acceptable agreement, per generally accepted threshold values. Further examination of the divergent response pair showed one problematic observation. As there was no theoretical or pre-registered reason for modifying these observations per the code book or previous literature, all data were retained for analysis. See Appendix C for reliability ratings.

Results

Ninety-four participants completed the study. It is important to note that a significant number of participants listed zero weaknesses, which led to them being excluded from certain computations due to missingness resulting from subsequent log-transformations. This participant attrition resulting from analysis may impact the validity of our original study and is discussed further in the next section. Similar to the replicated study, participants described several strengths and weaknesses that were positively skewed, so these variables were log transformed. Per the procedure of the

previous study, the number of strengths was divided by the number of weaknesses to arrive at a humility score for each participant¹. The resulting scores were also not normally distributed; therefore, they too were log transformed. All available participant data was used to run the analyses.

The analyses showed that participants in the awe and the neutral condition did not significantly differ in their balance between strengths and weaknesses disclosed (i.e., their humility score, $t(69) = -0.34, p = 0.438$); see Appendix D for more information. This contradicts the original study, where a significant difference was found, $t(84) = 2.38, p = 0.02$.

Next, strengths and weaknesses were examined individually, which is where the original study found that participants in the awe condition reported significantly fewer strengths and a similar number of weaknesses. In the current study, participants in the awe condition reported slightly more strengths ($t(91) = 0.85, p = 0.397$) and slightly more weaknesses ($t(82) = 0.50, p = 0.618$), and both those differences were not significant when compared to the neutral condition; see Appendix E for more information. To determine the overall effect of the awe manipulation on the variable of humility, the log-transformed variable of humility was regressed on reported feelings of awe. There was no significant difference between awe and neutral groups, $F(1, 69) = 0.11, p = 0.738$.

To ensure that the manipulation was successful in inducing awe in the participants in the experimental condition, participant-reported feelings of awe were regressed onto their condition. Results indicate that the experimental condition was a significant positive predictor of awe scores, $b_1 = 2.85, t(91) = 8.80, p < 0.001$. The average reported awe for participants in the neutral condition was 2.13, $t(91) = 9.33, p < 0.001$. Participant condition accounted for $R^2_{\text{adjusted}} = 45.4\%$ of the variance in reported awe. Similar results were found when the same calculations were performed with a composite of awe that included reported feelings of awe, amazement, fear, and wonder. Experimental condition was a significant predictor of this awe composite score, $b_1 = 2.55, t(91) = 12.10, p < 0.001$, and participant condition accounted for $R^2_{\text{adjusted}} = 61.25\%$ of the variance. These results confirm that awe was significantly different between conditions and disprove the manipulation failure as a potential explanation for a failure to replicate the results of the original study. See Appendix F for a figure of these results.

In addition to the replication, it was alternatively hypothesized that participants with higher scores of DS would list fewer strengths due to a diminished but non-negative self-concept and self-efficacy. Appendix G shows a figure with respondents plotted by their total score on the CES-D and the number of strengths reported. Participants wrote 4.8 strengths on average, and depression scores were 22.6, with a standard deviation of 10.7, which is noteworthy in that the average participant would score as being at moderate risk of DS per the approved cutoffs. Greater DS, as indicated by higher CES-D scores, did not significantly predict the number of strengths reported, $b_1 = -0.01, t(91) = -0.73, p = 0.470$, and CES-D scores accounted for $R^2_{\text{adjusted}} < 0.1\%$ of the variance.

Discussion

Stellar et al. conducted a study to investigate if there was an association between the feeling of awe and humility¹. The study investigated whether the feeling of awe would lead to humility through watching a video and then listing personal strengths and weaknesses. They hypothesized that watching an awe-inducing video would lead participants to write fewer strengths before writing their weaknesses. Their results demonstrated that their hypothesis was correct, and they found a significant association between awe and humility. This led the researchers to conclude that awe does in fact induce humility¹.

The goal of the current study was to determine whether these findings could be replicated or if there was potentially another factor that could have affected their results. We conducted a direct replication of the original study and included a potential confound of depression¹. We speculated that the original study's findings, wherein the participants in the experimental group listed fewer strengths but the same number of weaknesses, could have been mediated by depression levels. Beck's cognitive model of depression has found that depressive symptoms are a result of the negative cognitive triad, meaning that people with depression are more prone to negative self-schemas and negative self-thought². Due to the original study's operationalization of humility as listing strengths and weaknesses, we hypothesized that listing fewer strengths could have been related to negative self-schemas, as depressed individuals often find it hard to see the positive in life, in our case, perhaps their own strengths. However, based on our findings, no significant correlations were found between awe and humility, or depression and humility, leading to both the rejection of our alternate hypothesis and the failure to directly replicate the original study. Specifically, our results show that participants with greater DS did not list fewer strengths compared to those who scored lower on the CES-D. Therefore, our study's findings seem inconsistent with existing literature on depression and Beck's cognitive triad, as having a negative view of oneself, or negative self-schema, has been reliably linked with DS²⁻⁵. Another study that evaluated depression in adolescents found that those with a more positive self-concept appeared to have less DS⁹. Therefore, according to this myriad of studies, the written self-evaluations used to measure humility should have been affected negatively in those that had higher depression. According to a systematic review, depression is a highly prevalent problem in university students that causes a decrease in self-esteem¹⁰, demonstrating once again that our results should have shown a decrease in strengths in participants with a higher score for depression.

Moreover, our study has not found any mediating effects in the original study's association between awe and humility. In our study, the additional confound of depression was not found to explain the association, directly or as a mediating variable, between awe and humility per the results from the replicated study.

Limitations

The study we conducted was limited with regards to the internal validity of its conclusions, the external validity, and the power of the study's entirety. First, awe is an extremely vast and abstract concept, often considered to be a rare and intense emotion¹¹, therefore our manipulation of evoking it through a short YouTube video should be more closely examined. The post-test-only measure of awe induction in participants allows for the possibility that the difference observed between the experimental and control groups could be explained by lower levels of awe in the control group, rather than the assumed heightened levels in the experimental group. The neutral fence-building video used in the control group was assessed in the original study for emotions elicited by the video as outlined in our methods, but not whether it diminished other emotions¹. This allows for the possibility that the control video had an effect, such as lowering levels of awe, wonder, or amazement, rather than being truly neutral. This potential confound could mean that the experimental video did not induce awe in the first place, impacting the validity of our conclusions. To fix this manipulation issue in the future, we could either pre- and post-test the neutral video to observe potential awe-depleting effects, or simply use a more valid and reliable awe-induction technique as our manipulation, discussed later in the future directions section. Similarly, the original study did not test the validity of their operationalization of humility as a ratio of self-reported strengths to weaknesses¹. Thus, we cannot be confident in the construct validity of the results gathered through these measures, both subjectively (face and content validity) and objectively (criterion, convergent, and discriminant validity).

It is possible there were order effects in both humility and awe induction measurements. This would be due to all participants being told to list strengths before moving on to weaknesses, as well as the induced emotion questionnaire always beginning with self-reported awe. The two-minute time limit appeared to have caused issues with a proportion of the participants, as some were cut off either before or while they listed weaknesses. These issues skewed the resulting ratios and potentially impacted the measure's ability to capture humility. If one were to conduct this study again, they would benefit from using a combination of measurements; for example, adding reliable physiological measurements of awe such as skin conductance and pupil diameter¹², among other self-report measures of humility¹³. The combination of self-report and physiological assessment has been found to have higher validity than either one alone¹¹. If the self-report measure of humility was retained, we could reduce order effects by removing the timer and by counterbalancing the order of strengths & weaknesses across participants, as well as randomizing the order of the emotions listed in the awe-induction questionnaire. Similarly, we could use a different measure to record awe induction, such as the Situational Awe Scale, a valid and reliable measure of awe induction in the lab¹⁴, rather than having participants self-report the level of awe and other emotions they felt, as this method is vulnerable to diverse biases.

A limitation concerning the external validity of our study was selection bias, given our convenience sample of younger-skewing undergraduate psychology students. Our sample consisting solely of psychology students presents a serious limitation, as this population is taught about the use of deception in psychological experiments and thus may be more suspicious and critical of studies in which they participate, as demonstrated through the insightful correct guesses of our hypothesis from some participants. This could have led to demand characteristic biases, wherein participants distort their responses, whether consciously or unconsciously, in accordance with the presumed hypothesis. Thus, viewing the experimental awe video and then immediately being asked to report awe levels may have had a suggestive effect on the participants' responses and led to biased responses. Another possible validity issue is the presence of self-report bias due to social desirability effects, reflected in higher-than-average levels of trait agreeableness in psychology undergraduates who volunteer for studies¹⁵. Self-report answers can be strongly influenced (consciously or not) by how participants want others to perceive them, leading to biased responses; in this case potentially leading participants to list more strengths than they would have had it been a completely anonymous online study, like the original. The computer-based and single-session nature of the current study could have protected against this marginally, but it nonetheless may have had an effect. Reactivity bias, due to the presence of researchers, poses another potential validity issue. All these biases can limit the generalizability of conclusions, as the results are not necessarily representative of the broader population in real-life situations. Going forward, we would attempt to increase our external validity by using a more representative sample, which could potentially reduce threats such as demand characteristics and volunteer bias, and hopefully increase the generalizability of results.

The suggestions presented for reducing order effect bias, such as randomization and counterbalancing, could potentially reduce demand characteristics as well, as the study's focus would be less obvious to participants. To reduce reactivity bias, we could move the study online, although that would impact the potential of using physiological measurements. However, to reduce the risk of confounds, we intentionally placed participants at computers with a space between each participant, when space permitted.

Another limitation of our study is the small sample size: coupled with the small and statistically insignificant effects we found, it is likely that the study had low power, increasing the likelihood of making an error regarding the conclusions of the study—in this case failing to reject the null hypothesis.

Lastly, since certain participants failed to report weaknesses, but not

strengths, the number of excluded observations varied across calculations. Computations including ratios or multiple log transformations specifically required that more observations be excluded from the analyses, because mathematically, dividing by zero is undefined. This represented an important mathematical limitation, leading our statistical analyses to be prejudiced against participants who did not write weaknesses for several reasons such as time limit, reactivity, etc. It is conceivable that taking those participants out of the analyses could have skewed the data in a problematic way. In future research, listing no weaknesses would be added to the exclusion criteria and considered as a failure to follow instructions to help minimize variability in sample size across calculations. We would also recruit a sufficient sample size with responses of both strengths and weaknesses to obtain enough power to detect small effects. Furthermore, developing, validating, and assessing participants with a measure of assessing humility by self-report of strengths and weaknesses that does not exclude participants who report no strengths or weaknesses will be important in strengthening the validity of studies that measure this construct, through reduced attrition of participants.

Future Directions

The study of awe and humility comes with many unanswered questions that future directions of exploration may help to answer. One study, for example, discovered a potential mediating effect of dispositional humility on DS, as a self-regulating mechanism involved in self-differentiation¹⁶. Thus, there does seem to be a correlation between depression and humility, although perhaps more complex than we believed and not directly related to negative self-image, possibly explaining why we did not find a significant correlation between DS and fewer strengths being listed in our additional hypothesis. Another study found that humility in university students was positively associated with conscientiousness, openness, love of life, happiness, and self-efficacy, but negatively associated with agreeableness, neuroticism, and depression¹⁷. However, as stated previously, university students who volunteer for psychology studies tend to have relatively higher levels of agreeableness¹⁵, which correlates negatively with humility. Another study found a negative correlation between humility, specifically the H dimension of the HEXACO personality model, and a wide array of Machiavellian behaviours such as criminal activity and power-seeking tendencies, potentially hinting at a protective social benefit related to humility¹⁸ in the form of stronger hierarchical structures¹⁹. Namely, leaders with higher state and/or trait humility are less likely to make decisions that are self-serving at the expense of the group¹⁸, and this reinforces follower humility while acting as a protective factor against Machiavellianism in followers. This would, in turn, reduce their potentially detrimental power-seeking tendencies.¹⁹ Cross-cultural studies are of interest, as recent investigations into the reproducibility of the Humility-honesty dimension as a personality factor has not shown successful retrieval by Exploratory Structural Equation Modeling across all cross-cultural groups²⁰. Research by Ion and colleagues (2017) was unable to reproduce a model that included additional predictive validity from a 6th facet of personality from the HEXACO model²⁰, Humility-honesty, compared to the five-factor model by Costa and McCrae²¹, for certain cultural groups. Examining differences in the experience and expression of humility based on cultural differences, such as socioeconomic status, previous experience with awe, or predominance of differing majority religions, may help us understand the etiology of humility within specific cultures. Future research could attempt to clarify the tangled relationships between experiences of awe, trait and state humility, self-schema, DS, as well as potential moderation through demographic factors and personality traits.

One final avenue of future research involves studying how lab-induced awe differs from natural experiences of awe in the real world, and whether humility is more reliably induced by authentic experiences of awe. Chirico et al. (2017) found that since awe is such a complex emotion, with experi-

ences described as meaningful and profound, the level of awe induced in the lab is heavily dependent on the immersive quality of the induction¹¹. The results of their study concluded that immersive videos, considered to be the most realistic form of virtual reality (VR), significantly enhanced self-reported (subjective) and physiological (objective) measurements of awe when compared to 2D screen videos, like the one we used in our study¹¹. VR accessibility and quality are rapidly increasing with each passing year of technological advancements, proposing an immensely exciting solution to the future of experimental research, in our case specifically relating to stronger and more reliable manipulation of awe in laboratory settings.

Conclusion

While our results fail to reproduce the findings of the previous paper¹, the future directions and conceptual replications of this group of studies will further examine the link between awe and humility and how they contribute to a uniquely human condition. To this end, this field of research remains invaluable in examining experiences that until recently have been the purvey of only philosophy and religion.

Acknowledgements

We want to thank Dr. Eric Hehman, Assistant Professor at McGill University, for his guidance and support throughout the project's development, execution, and final paper composition.

References

1. Stellar, J. E. & et al. Awe and humility. *J. Pers. Soc. Psychol.* **114**, 258–269 (2018). <https://doi.org/10.1037/pspi0000109>
2. Beck, A. T. & et al. Levels of hopelessness in DSM-III disorders: A partial test of content specificity in depression. *Cognitive Ther. Res.* **12**, 459–469 (1988). <https://doi.org/10.1007/BF01173413>
3. Mahali, S. C., Beshai, S., Feeney, J. R. & Mishra, S. Associations of negative cognitions, emotional regulation, and depression symptoms across four continents: international support for the cognitive model of depression. *B.M.C. Psychiatry* **10**, 18 (2020). <https://doi.org/10.1186/s12888-019-2423-x>
4. Phillips, W. J., Hine, D. W. & Thorsteinsson, E. B. Implicit cognition and depression: a meta-analysis. *Clin. Psychol. Rev.* **30**, 691–709 (2010). <https://doi.org/10.1016/j.cpr.2010.05.002>
5. Sowislo, J. F. & Orth, U. Does low self-esteem predict depression and anxiety? A meta-analysis of longitudinal studies. *Psychol. Bull.* **139**, 213–240 (2013). <https://doi.org/10.1037/a0028931>
6. Stellar, J. E., Manzo, V. M., Kraus, M. W. & Keltner, D. Class and compassion: socioeconomic factors predict responses to suffering. *Emotion* **12**, 449–459 (2012). <http://dx.doi.org/10.1037/a0026508>
7. Radloff, L. S. The CES-D scale: A self-report depression scale for research in the general population. *Appl. Psychol. Meas.* **1**, 385–401 (1977). <https://doi.org/10.1177/014662167700100306>
8. Shaffer, K. in *Encyclopedia of Quality of Life and Well-Being Research* (ed Michalos, A. C.) 637–640 (Springer Netherlands, 2014).
9. Hards, E. et al. Self-evaluation and depression in adolescents with a chronic illness: a systematic review. *Clin. Child Psychol. Psychiatry* **28**, 382–397 (2023). <https://doi-org/10.1177/13591045221115287>
10. Ibrahim, A. K., Kelly, S. J., Adams, C. E. & Glazebrook, C. A. A systematic review of studies of depression prevalence in university students. *J. Psychiatr. Res.* **47**, 391–400 (2013). <https://doi.org/10.1016/j.jpsychires.2012.11.015>
11. Chirico, A. & et al. Effectiveness of immersive videos in inducing awe: an experimental study. *Sci. Rep.* **7**, 1218 (2017). <https://doi.org/10.1038/s41598-017-01242-0>
12. Takano, R. & Nomura, M. A closer look at the time course of bodily responses to awe experiences. *Sci. Rep.* **13**, 22506 (2023). <https://doi.org/10.1038/s41598-023-49681-2>
13. Nielson, R. & Marrone, J. Humility: our current understanding of the construct and its role in organizations. *Int. J. Manag. Rev.* **20** (2018). <https://doi.org/10.1111/ijmr.12160>
14. Krenzer, W. L. D., Krogh-Jespersen, S., Greenslit, J., Price, C. A. & Quinn, K. A. Assessing the experience of awe: validating the situational awe scale. Preprint at: <https://doi.org/10.31234/osf.io/dsytn> (2020).
15. Dollinger, S. J. & Leong, F. T. L. volunteer bias and the five-factor model. *J. Psychol.* **127**, 29–36 (1993). <https://doi.org/10.1080/00223980.1993.9915540>
16. Jankowski, P. J., Sandage, S. J. & Hill, P. C. Differentiation-based models of forgivingness, mental health and social justice commitment: mediator effects for differentiation of self and humility. *J. Posit. Psychol.* **8**, 412–424 (2013). <https://doi.org/10.1080/17439760.2013.820337>
17. Ross, L. T. & Wright, J. C. Humility, personality, and psychological functioning. *Psychol. Rep.* **126**, 688–711 (2023). <https://doi.org/10.1177/003329412111062819>
18. Ashton, M. C. & Lee, K. The HEXACO model of personality structure and the importance of the H factor. *Soc. Personal. Psychol.* **2**, 1952–1962 (2008). <https://doi.org/10.1111/j.1751-9004.2008.00134.x>
19. Shu-Chen, C., Wen-Qian, Z. & Na-Ting, L. Leader humility and machiavellianism: investigating the effects on followers' self-interested and prosocial behaviors. *Front. Psychol.* **13**, 742546 (2022). <https://doi.org/10.3389/fpsyg.2022.742546>
20. Ion, A. & et al. A cross-cultural analysis of personality structure through the lens of the HEXACO model. *J. Pers. Assess.* **99**, 25–34 (2017). <https://doi.org/10.1080/00223891.2016.1187155>
21. McCrae, R. R. & John, O. P. An introduction to the five-factor model and its applications. *J. Pers.* **60**, 175–215 (1992). <https://doi-org.proxy3.library.mcgill.ca/10.1111/j.1467-6494.1992.tb00970.x>
22. Krippendorff, K. *Content Analysis: An Introduction to its Methodology* (Sage publications, 2018).

Appendix A

Table 1. Center for Epidemiologic Studies Depression (CES-D) Scale. Instructions: Please read each question carefully, then circle one of the numbers to the right to indicate how you felt or behaved during the past week, including today⁷. Note: scores range from 0 to 60. Higher scores indicate more depressive symptomatology.

During the past week:	Rarely or none of the time (less than 1 day)	Some or a little of the time (1-2 days)	Occasionally or a moderate amount of the time (3-4 days)	Most or all of the time (5-7 days)
1) I was bothered by things that usually don't bother me	0	1	2	3
2) I did not feel like eating; my appetite was poor	0	1	2	3
3) I felt that I could not shake off the blues even with help from my family and friends	0	1	2	3
4) I felt that I was just as good as other people	3	2	1	0
5) I had trouble keeping my mind on what I was doing	0	1	2	3
6) I felt depressed	0	1	2	3
7) I felt that everything I did was an effort	0	1	2	3
8) I felt hopeful about the future	3	2	1	0
9) I thought my life been a failure	0	1	2	3
10) I felt fearful	0	1	2	3
11) My sleep was restless	0	1	2	3
12) I was happy	3	2	1	0
13) I talked less than usual	0	1	2	3
14) I felt lonely	0	1	2	3
15) People were unfriendly	0	1	2	3
16) I enjoyed life	3	2	1	0
17) I had crying spells	0	1	2	3
18) I felt sad	0	1	2	3
19) I felt that people disliked me	0	1	2	3
20) I could not get "going"	0	1	2	3

Appendix B

Codebook Instructions for Counting Participant-Reported Strengths and Weaknesses

A codebook was established prior to the start of coding. If participants specifically stated a trait as a strength/weakness, coders were to count them as such regardless of how the coder viewed the trait. Some participants may follow a trait by a description of such a trait. This was only to be counted as one strength/weakness. Raters were to assign participants positive integers with no decimal values. If a participant listed strengths/weaknesses that may seem similar to the rater, they were to be counted as separate traits. As a time limit was set for participants while writing their strengths and weaknesses, it is possible that they may have been cut off while writing as the survey moved on to the next section. Raters were to count these partially stated traits provided that they made sense but were not to assume the rest of the sentence.

Appendix C

Table 2. Table of Interrater Reliability Analyses by Rater Pairs. ICC refers to interrater reliability calculated through two-way mixed effect average measure intraclass correlation coefficient measuring absolute agreement. α -Reliability refers to Krippendorff's alpha, a coefficient designed to measure agreement between observers. All analyses were performed using R Statistical Software version 4.3.1 (R Core Team 2023) via the irr R package v0.84.1. ICC scores of 0.5 to 0.75 (*) and greater than 0.9 (**) are indicative of moderate and excellent reliability, respectively²². Alpha scores between 0.66 and 0.80 (*) and between 0.81 and 0.99 (**) indicate tentatively acceptable and acceptable agreement, respectively⁷

Rater Pair	n Observations	Variable	ICC	α -Reliability
Pair 1	29	Strengths	0.72*	0.69*
		Weaknesses	0.91**	0.94**
Pair 2	32	Strengths	0.97**	0.94**
		Weaknesses	0.98**	0.99**
Pair 3	32	Strengths	0.97**	0.95**
		Weaknesses	0.95**	0.97**

Appendix D

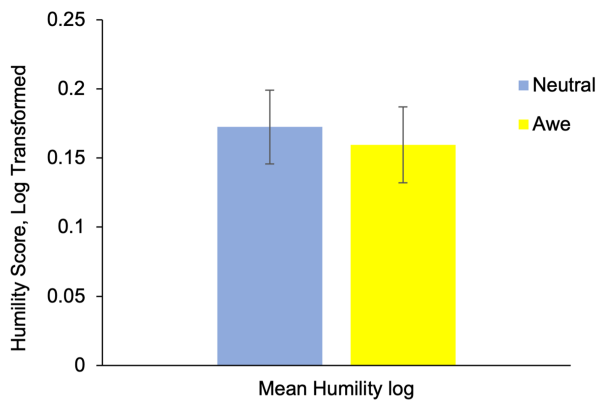


Figure 1. Calculated Humility Scores by Condition. Humility is calculated by dividing log-transformed average strength scores by log transformed weakness scores (error bars show standard errors). Humility scores in the awe condition ($M = 0.16$, $SD = 0.16$) when compared to the neutral condition ($M = 0.17$, $SD = 0.16$) were not significantly different $t(69) = -0.34$, $p = 0.438$.

Appendix E

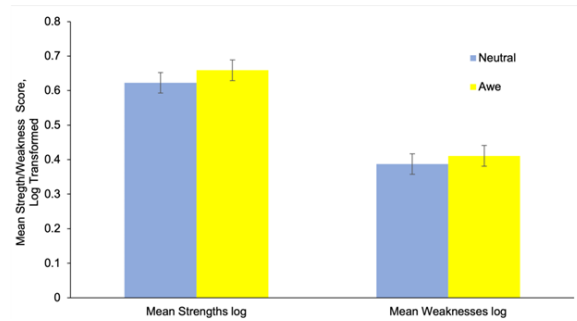


Figure 2. Average Log-Transformed Strength and Weakness Scores by Condition. The number of strengths and weaknesses that participants reported was positively skewed; therefore, we log transformed them. There was no significant difference between log-strength scores for the awe ($M = 0.66$, $SD = 0.18$) and neutral ($M = 0.62$, $SD = 0.23$) conditions $t(91) = 0.85$, $p = 0.397$. There was no significant difference between log-weakness scores for the awe ($M = 0.41$, $SD = 0.24$) and neutral ($M = 0.39$, $SD = 0.19$) conditions $t(82) = 0.50$, $p = 0.618$. Error bars show standard errors.

Appendix F

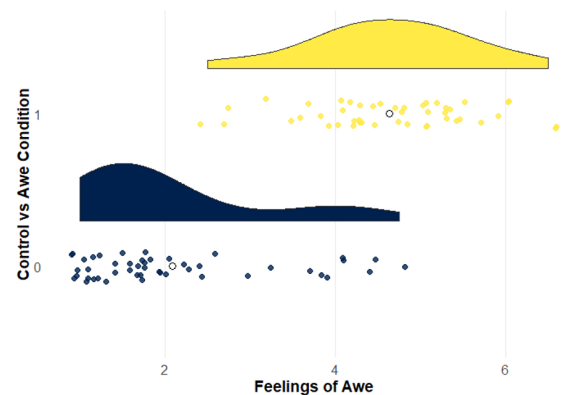


Figure 3. Differences in Reported Feelings of Awe Between Conditions. 0 = Neutral (control) condition participants in blue, 1 = awe condition participants in yellow. Results indicate that the experimental condition was a significant positive predictor of awe scores, $b_1 = 2.85$, $t(91) = 8.80$, $p < 0.001$. The average reported awe for participants in the neutral condition was 2.13, $t(91) = 9.33$, $p < 0.001$. Participant condition accounted for $R^2_{\text{adjusted}} = 45.4\%$ of the variance in reported awe.

Appendix G

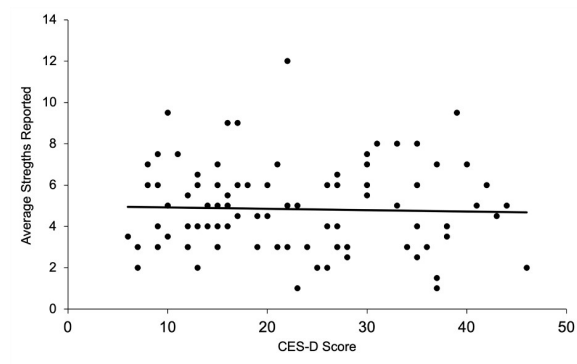


Figure 4. Changes in Reported Strengths as a Function of Depression Score. This figure shows the relationship between the number of participant-reported personal strengths, averaged between two raters, and their total score on the Center for Epidemiological Studies – Depression Scale (CES-D).

Antimicrobial Resistance Mechanisms of Gram-Positive and Gram-Negative Bacteria

Review Article

¹Department of Life Sciences,
Imperial College London,
London, England, UK

Abstract

The discovery of antibiotics has long helped humans in the battle against bacteria. However, the misuse of antibiotics in industries and medical systems has unintentionally provided an ideal environment for bacteria to develop resistance mechanisms through mutations and gene transfer, resulting in the emergence of antimicrobial-resistant bacteria. This has proven to be an urgent and pressing issue in the global healthcare system, resulting in increased mortality. Therefore, increasing resources are invested to study their different resistance mechanisms and develop corresponding novel drugs and treatment methods. This review briefly introduces several key resistance mechanisms with examples from both Gram-negative and Gram-positive bacteria, the current and novel methods for treating multiple drug-resistant bacteria as well as the potential actions that could be done to improve the situation.

Keywords

Antimicrobial resistance,
antibiotics, gram-positive,
gram-negative

Email Correspondence

zhiwen.xiao20@imperial.ac.uk

<https://doi.org/10.26443/msurj.v19i1.238>

©The Authors. This article is
published under a CC-BY license:
<https://creativecommons.org/licenses/by/4.0/>

Introduction

The discovery of penicillin in 1928 spearheaded the continuous discovery and development of antibiotics, resulting in various families of antibiotics¹. Being a crucial and effective method to treat bacterial infections, antibiotics have been widely used in healthcare and the husbandry of livestock, saving countless lives and preventing dramatic economic loss. However, increasing cases of antibiotic misuse contribute to the occurrence of antimicrobial resistance (AMR) in bacterial pathogens through a process of selective evolution^{2,3}. Mutations in the genetic material can occur spontaneously during processes like DNA replication in asexual reproduction, at times resulting in AMR in bacteria which is then selected in their respective environments. Once resistant strains occur, the spreading of the resistance can be vertically and horizontally transmitted to other bacteria^{2,3}. The infections of these AMR bacteria are difficult to treat and have become worldwide medical issues, with an annual approximate of 700,000 deaths and a predicted increasing trend, reaching 10 million annual deaths by 2050⁴. One infamous multiple drug resistant (MDR) bacteria strain, methicillin-resistant *Staphylococcus aureus* (MRSA) has resulted in more than 100,000 deaths in 2019⁵. Together with other MDR bacteria, they are also known as “superbugs”. To date, the six most threatening AMR bacterial pathogens identified by the World Health Organization (WHO) are *Enterococcus faecium*, *Staphylococcus aureus*, *Klebsiella pneumoniae*, *Acinetobacter baumannii*, *Pseudomonas aeruginosa*, and *Enterobacter* species, which together are referred as “ESKAPE”.

Additionally, an article published by the WHO⁶ included 12 of the most troublesome bacteria in hospitals classified into 3 priority levels (critical, high and medium) according to the therapeutic difficulty and the urgency of the need to develop effective antibiotics against these bacteria. In Table 1, other pathogens are included in addition to the “ESKAPE.” By classifying them based on Gram staining, it is apparent that there are more Gram-negative bacteria than Gram-positive bacteria. This classification represents structural differences; there is an additional outer membrane enveloping the cell wall in the Gram-negative bacteria.

When treating infections caused by these MDR strains, clinicians often have no options but to administer a combination of less effective antibiotics or repurpose previous drugs with suboptimal efficacy or toxicity⁷. The reasons behind this may not only be because of the lack of financial support but may also be the difficulties and challenges that are accompanied by new antibiotic development⁵. Therefore, the development of new antibiotic drugs has become less attractive to pharmaceutical companies, leading to a decline in antibiotic options when treating MDR bacterial infections.

More importantly, the study of the underlying AMR mechanisms is vital when trying to overcome resistance. Understanding the factors that contribute to the AMR phenotype in the bacteria can aid in guiding the development of antimicrobial drugs. This review aims to briefly cover the main mechanisms and strategies that some of the Gram-positive and Gram-negative bacteria use to survive upon antibiotic treatment.

Common Antimicrobial Resistance Mechanisms

To ensure their survival, bacteria evolved several resistance mechanisms to antibiotics categorized into 3 main types: intrinsic, acquired and adaptive resistance. Intrinsic resistance refers to the cellular and genetic regulation of expression of some antibiotic-inactivating enzymes, cell permeability and efflux of drugs^{2,3}. Acquired and adaptive resistance require external assistance or stimuli; the former includes horizontal gene transfer from other species as well as genetic mutations whereas the latter refers to the gradual change of bacterial protein expression and phenotypes over continuous exposure to antibiotics or other environmental stress factors⁸. Despite the structural differences between Gram-positive and Gram-negative bacteria, some of their resistance mechanisms are common (Figure 1): both can degrade or modify antibiotics, or reduce the affinity or susceptibility of the drug target via enzymatic activities. The genes encoding the resistant enzymes can also exist in a plasmid which are transferred from other bacteria via conjugation, transformation or transduction⁸. Additionally, the porins on the outer membrane proteins of Gram-negative allow the passive pas-

Table 1. A prioritised summary of antibiotic-resistant pathogens proposed by the World Health Organisation^{2,6}.

Priority	Gram-Positive	Gram-Negative
Critical	None	Carbapenem-resistant <i>A. baumannii</i>
		Carbapenem-resistant <i>P. aeruginosa</i>
		Carbapenem-resistant <i>Enterobacteriaceae</i>
High	Vancomycin-resistant <i>E. faecium</i>	Clarithromycin-resistant <i>Helicobacter pylori</i>
	MRSA/VISA [*] /VRSA [†]	Fluoroquinolone-resistant <i>Campylobacter spp.</i>
		Fluoroquinolone-resistant <i>Salmonellae</i>
		Cephalosporin/Fluoroquinolone-resistant <i>Neisseria gonorrhoeae</i>
Medium	Penicillin-non-susceptible <i>Streptococcus pneumoniae</i>	Ampicillin-resistant <i>Haemophilus influenzae</i>
		Fluoroquinolone-resistant <i>Shigella spp.</i>

^{*} VISA: vancomycin-intermediate *S. aureus*.

[†] VRSA: vancomycin-resistant *S. aureus*.

sage of small molecules which may be the potential entrance for hydrophilic antibiotics. In other words, mutations or downregulation of porins lead to AMR⁹. Although there is no such restrictive permeability barrier in Gram-positive bacteria, other strategies exist such as the thickening of their peptidoglycan cell wall to block antibiotics or producing enzymes that can degrade antibiotics⁸. Interestingly, a group of complex bacterial machinery, efflux pumps, are present in both types of bacteria to actively extrude antibiotics or other drugs specifically or broadly. Bacterial signalling molecules like autoinducers can also be transported via efflux pumps to regulate responses to antibiotics and facilitate defence actions². According to their protein sequences, energy source and substrate range, they are categorized into five superfamilies, including the major facilitator superfamily (MFS), the resistance nodulation division superfamily (RND), the multidrug and toxic compound extrusion family, the small multidrug resistance family and the ATP-binding cassette (ABC) transporters. All efflux pumps except ABC use proton or sodium gradients as energy sources, while ABC pumps rely on ATP hydrolysis. For MDR Gram-positive bacteria, such as *S. pneumoniae* and *S. pyogenes*, MFS transporters are crucial for the extrusion of macrolide-family antibiotics. Additionally, RND transporters are primarily found in Gram-negative bacteria and contribute to their MDR, while members of this superfamily also exist in other organisms. For instance, RND transporters extrude tetracyclines in *Enterobacteriaceae* and *P. aeruginosa*. Moreover, genes encoding RND pumps are identified in genomes of various clinical isolates of pathogenic Gram-negative bacteria, indicating their importance in the bacterial intrinsic AMR. Different from efflux pumps in Gram-positive bacteria, a model RND transporter in Gram-negative bacteria spans across the periplasm and consists of a transporter on the inner membrane, periplasmic linker proteins and a protein channel on the outer membrane¹⁰.

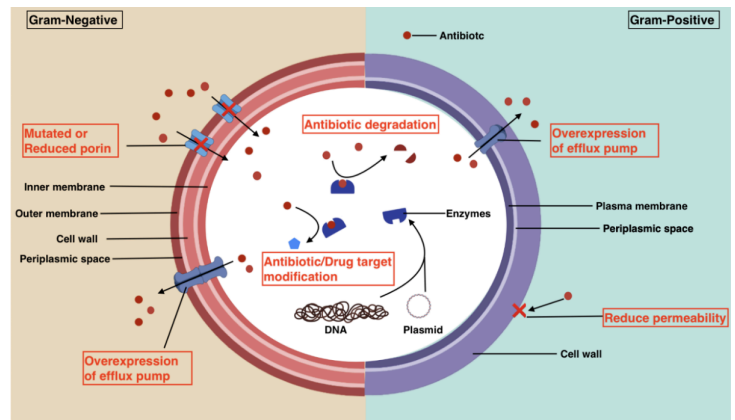


Figure 1. The schematic diagram of Gram-positive (right) and Gram-negative (left) bacteria and their antibiotic resistance mechanisms. Key AMR mechanisms are highlighted in red. Created with BioRender.com.

AMR of ESKAPE Pathogens

Gram-Positive Bacteria

Among the priority list of bacterial pathogens, Gram-positive bacteria are only included in the medium and high ranking, which might be due to the lack of an outer membrane that covers the peptidoglycan cell wall and acts as an additional selective barrier in Gram-negative bacteria². Nonetheless, many MDR bacteria are still Gram-positive⁹, and two examples are described below.

S. aureus has multiple resistant strains, including AMR to methicillin, vancomycin and fluoroquinolone. MRSA is resistant to all beta-lactam antibiotics like penams and cepams, and this is mainly due to the penicillin-binding protein (PBP) 2a, which is a transpeptidase that can function in the presence of beta-lactam antibiotics. Therefore, the synthesis of the nascent cell wall is unaffected, allowing bacterial growth¹¹. Moreover, although vancomycin is considered the last resort for treating MRSA, VISAS and VRSA have also emerged independently with different mechanisms. The former thickens its peptidoglycan cell wall that contains decoys of the actual drug target of vancomycin, which are two D-alanine residues. The latter adopted an external gene that allows modification of the target site so that vancomycin cannot function⁹, as in Figure 2. The decoys produced by VISA can sequester vancomycin and therefore reduce the chance of vancomycin binding to the key cell wall synthesis site, but there is still binding of free D-alanine-D-alanine, which can further reduce the drug efficacy¹².

E. faecium, another problematic pathogen, has strains that are resistant to betalactam and vancomycin as well¹³. For the beta-lactam resistance, both mutations and overexpression of low-affinity PBP5 were detected in the resistant *E. faecium* strains. Similarly, the vancomycin resistance in *E. faecium* is contributed by the same modification of the target site, replacing the terminal D-alanine with D-lactate. Additionally, *E. faecium* also are resistant to ribosome-targeting antibiotics, like aminoglycoside (kanamycin, gentamycin) and streptogramins (quinupristin-dalfopristin), by enzymatic modification of antibiotics and drug efflux pumps, respectively¹³.

Gram-Negative Bacteria

Different from Gram-positive bacteria, Gram-negative bacteria have an outer membrane and thinner layer of the peptidoglycan cell wall. The outer membrane is attached with endotoxic lipopolysaccharide (LPS) chains and contains porins for the transportation of small molecules². Most of the bacteria on the list, including all members in the critical priority, are Gram-negative bacteria, as some of them are responsible for severe nosocomial infections and the presence of resistance only worsens the situation².

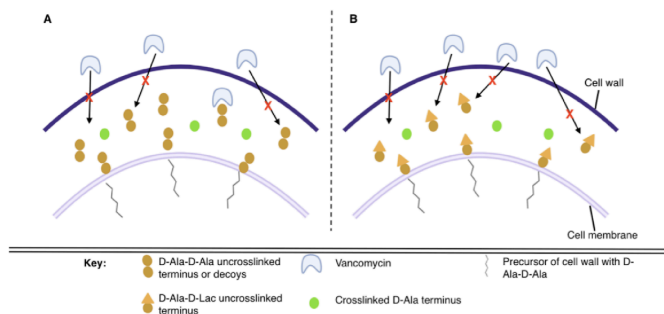


Figure 2. AMR resistance mechanisms with VISA and VRSA. (A) The schematic shows how VISA continuously thicken its cell wall by producing a large amount of many D-Ala-D-Ala terminus. (B) VRSA has a mutated terminus, which becomes D-Ala-D-Lac in its uncrosslinked form, so vancomycin is unable to bind. Created with BioRender.com.

A. baumannii, as a member of ESKAPE, is an aerobic pathogen that is commonly found in hospitals and causes opportunistic infections of the skin, bloodstream and other soft tissues, which contributes to up to 20% of nosocomial infections in critically ill patients in the intensive care units globally^{2,14}. Moreover, epidemiological studies showed that injured soldiers or veterans who returned from the Middle East war zones were infected with *A. baumannii*, and this gave rise to MDR *A. baumannii* in the civilian hospitals of their home countries¹⁵. The AMR of *A. baumannii* is achieved by the expression of: (1) Four classes of beta-lactamases, which are enzymes for breaking the beta-lactam ring of betalactam antibiotics^{10,14}. Although encoded in both Gram-negative and -positive bacteria, beta-lactamase is more commonly associated with AMR of the former¹⁰. There are both narrow- and broad-spectrum beta-lactamases. One of which (PER-1) had also been reported to be a virulent factor with adhesive function¹⁴; (2) Four classes of multidrug efflux pumps except ABC transporters. Studies also demonstrated that overexpression of an efflux pump (AdeFGH) in *A. baumannii* promotes biofilm formation when exposed to subinhibitory antibiotic administration¹⁴; (3) Aminoglycoside-modifying enzymes¹⁴. In addition, *A. baumannii* reduces outer membrane permeability by downregulating porin expression. For instance, the reduced expression of multiple porins such as CarO and several other members in the outer membrane protein family had been shown to relate to AMR towards nalidixic acid, chloramphenicol, aztreonam and imipenem; Antibiotic site alteration is another AMR strategy used by *A. baumannii*, which include chemical modifications in bacterial gyrases, PBPs, 16S rRNA and LPS¹⁴.

Another example is *P. aeruginosa*, which is an opportunistic pus-causing pathogen and commonly found on surfaces of medical equipment. It has been proven to be the fourth most common nosocomial pathogen that is found in monitors, dialysis tubing and ventilator buttons, leading to 10% of nosocomial infections¹⁶. Four classes of betalactamases are identified in *P. aeruginosa*, catalyzing the breakdown of penicillin, cephalosporin and carbapenems. Another enzyme-mediated resistance is against aminoglycosides, as *P. aeruginosa* has enzymes that are responsible for adenylation, phosphorylation and acetylation of the antibiotics¹⁶. The AMR of *P. aeruginosa* involves a complex network of pathways that regulate the expression of well-studied resistance genes in its chromosome, which code for cephalosporinases, porins and multidrug efflux pumps¹⁷.

Novel Therapeutic Approaches

Fortunately, with the growing incidence of MDR bacterial infections, more and more professional studies are involved in the development of novel treatment plans and drug discovery. The current treatment plan for MDR Gram-negative bacteria, which are the most critical “superbugs”, often involves using antibiotics, like polymyxin B and colistin. These antibiotics

are thought to be the last resort and they are reserved for critically ill patients with MDR bacterial infections⁷. In the case of carbapenem-resistant *A. baumannii*, polymyxin and other old or novel antibiotics are administered as the first-line treatment option and different methods of drug delivery are used concomitantly, such as inhalation and intravenous infusion of polymyxin⁷. In addition, MDR treatment can be more effective during early-stage infection so rapid diagnostics that aim to narrow the antimicrobial susceptibility profile are essential⁷.

The need for novel antimicrobials continues to rise as AMR strains are continuously emerging, especially for those antibiotics of the last resort. Moreover, many drugs that are currently effective can be improved or have significant side effects, like neurotoxicity and nephrotoxicity of polymyxin¹⁸. Many different approaches target MDR bacteria, as in Table 2, while they are still in the basic and early stages of research.

One major category is peptide or peptide analogue antibiotics, which can be naturally or artificially synthesized. Darobactin and lugdunin are examples of cyclic natural peptide antibiotics that were discovered to be produced from bacterial symbionts in nematodes¹⁹ and human nasal bacterial commensals (*Staphylococcus lugdunensis*)^{19–21}, respectively. However, the former is ribosomal synthesized and post-translationally modified and inhibits outer membrane formation, while the latter is formed by non-ribosomal peptide synthetases and interferes with bacterial membrane potential^{19–21}. Inspired by natural peptides, researchers developed synthetic compounds that mimic natural antimicrobial peptides named chimeric peptidomimetic antibiotics²². They contain a β -hairpin peptide macrocycle, which is also found in natural antibiotics like polymyxin and colistin²². Another research developed two synthetic peptide-mimicking antibiotics called Pep16 and Pep19, which are cyclic heptapeptide composed of seven pseudo amino acids that structurally resemble amino acids²³. It was reported to be effective against several MDR Gram-negative and Gram-positive bacteria with minimal resistance²³.

With the advancement in CRISPR technologies, modules called antibacterial drones were made to directly act to hinder bacterial viability, growth or AMR mechanisms²⁴. Among the recently discovered drugs, halicin was repurposed by applying machine learning to screen through more than 100 million drugs and was a preclinical thiazole-containing drug for treating diabetes^{25,26}. Furthermore, cloning phage peptidoglycan hydrolases called endolysin allows the construction of recombinant endolysin and its derivatives, which leads to another effective approach to target MDR Gram-positive bacteria²⁷. Bacteriophage therapy is different from traditional antimicrobial molecules, as they can proliferate within bacteria, allowing “auto” dosing within the patients²⁸. The other advantages of using bacteriophages also include low toxicity, low chances of causing microbiome dysbiosis, high bacterial susceptibility, and biofilm clearance potential²⁸. Nonetheless, the current research on this therapy is bottlenecked by several difficulties: (1) do not have many choices that can be used, as some bacteriophages can be inefficient at killing or carrying virulent genes²⁹. (2) too high specificity with a narrow host spectrum, as even different strains of bacteria might require different bacteriophages to eliminate²⁹. (3) ethical issues since they are biological agents with the ability to reproduce inside the patient²⁹.

Social Influences of AMR

The presence of AMR has resulted in severe infections with longer treatment duration. From the patient’s perspective, the treatment against resistant bacterial infections can be time-consuming and ineffective, which may not only result in higher therapeutic costs but also more likely to develop into life-threatening infections³⁰. Additionally, the increasing trend of AMR bacterial infections can be detrimental to the healthcare systems,

Table 2. The summary of novel therapeutic approaches for treating MDR bacteria.

Novel Drugs	Modes of Actions	Target Bacteria	References
Darobactin	Inhibiting the crucial protein (BamA [*]) for assembly and folding outer membrane proteins.	Gram-negative	[19]
Lugdunin	Dissipating membrane potential and stimulating skin cells to produce antimicrobial peptides.	Gram-positive	[20, 21]
Chimaeric peptidomimetic antibiotics	Binding BamA and lipopolysaccharides and disrupting the outer membrane formation.	Gram-negative	[22]
Cyclic heptapeptide	Inducing bacterial membrane permeability and disruption.	None	[23]
Antibacterial drones	CRISPR-Cas9 [†] or CRISPR-dCas9 [†] complexes with bactericidal or virulence-blocking properties respectively.	None	[24]
Halicin	Disrupting electrochemical gradients and pH across bacterial membranes.	None	[25, 26]
Recombinant endolysin	Acting as peptidoglycan hydrolases to lyse bacteria.	None	[27]
Bacteriophages	Infecting and lysing bacteria upon lytic replication cycle.	None	[28, 29]

^{*} BamA, β -barrel assembly machinery A.

[†] CRISPR-(d)Cas9: Clustered regularly interspaced short palindromic repeats and (deactivated) CRISPR-associated protein 9.

since this will require longer hospitalization periods and occupy medical workers and various important facilities and equipment like intensive care units. More importantly, when trying to contain nosocomial outbreaks, all contaminated sectors of a hospital will be secured and closed. This also reduces the maximum hospital capacity, further burdening the system. Lastly, by having more people die of infections and the overloading of hospitals, the economy can be impacted. According to the Centers for Disease Control, the estimated annual cost due to AMR is 55 billion dollars³⁰. Therefore, the control and prevention of AMR are equally important, and the restrictions and policies about the use of antibiotics need to be established and strictly followed by both developed and developing countries. Also, the concept of AMR and other relevant knowledge is worth spreading across different countries for more prudent use of antibiotics.

Conclusion

The emergence of “superbugs” is a detrimental consequence of many factors, including human factors (e.g. antibiotic misuse) and natural factors (e.g. genetic mutations, gene transfer). AMR Gram-positive and Gram-negative bacteria have developed different resistance mechanisms and are detrimental to human society and the economy. Hence, the development of novel therapeutic approaches is vital and should keep up with the pace of the occurrence of MDR bacteria. Meanwhile, all antibiotics must be used with caution, despite being one of the most important medicines in human history.

References

- Gaynes, R. The Discovery of Penicillin—New Insights After More Than 75 Years of Clinical Use. *Emerg. Infect. Dis.* **23**, 849–853 (2017). <https://doi.org/10.3201/eid2305.161556>
- Brejijeh, Z., Jubeh, B. & Karaman, R. Resistance of Gram-Negative Bacteria to Current Antibacterial Agents and Approaches to Resolve It. *Molecules* **25**, 1340 (2020). <https://doi.org/10.3390/molecules25061340>
- Mancuso, G., Midiri, A., Gerace, E. & Biondo, C. Bacterial Antibiotic Resistance: The Most Critical Pathogens. *Pathogens* **10**, 1310 (2021). <https://doi.org/10.3390/pathogens10101310>
- Huemer, M., Mairpady Shambat, S., Brugger, S. D. & Zinkernagel, A. S. Antibiotic resistance and persistence—Implications for human health and treatment perspectives. *EMBO Rep.* **21**, e51034 (2020). <https://doi.org/10.15252/embr.202051034>
- Murray, C. J. et al. Global burden of bacterial antimicrobial resistance in 2019: a systematic analysis. *Lancet* **399**, 629–655 (2022). [https://doi.org/10.1016/S0140-6736\(21\)02724-0](https://doi.org/10.1016/S0140-6736(21)02724-0)
- World Health Organization. WHO publishes list of bacteria for which new antibiotics are urgently needed (2017); <https://www.who.int/news/item/27-02-2017-who-publishes-list-of-bacteria-for-which-new-antibiotics-are-urgently-needed>
- Bassetti, M., Peghin, M., Vena, A. & Giacobbe, D. R. Treatment of Infections Due to MDR Gram-Negative Bacteria. *Front. Med.* **6**, 74 (2019). <https://doi.org/10.3389/fmed.2019.00074>
- Chiş, A. A. e. a. Microbial Resistance to Antibiotics and Effective Antibiotherapy. *Biomedicines* **10**, 1121 (2022). <https://doi.org/10.3390/biomedicines10051121>
- Karaman, R., Jubeh, B. & Breijjeh, Z. Resistance of Gram-Positive Bacteria to Current Antibacterial Agents and Overcoming Approaches. *Molecules* **25**, 2888 (2020). <https://doi.org/10.3390/molecules25122888>
- Munita, J. M. & Arias, C. A. in *Virulence Mechanisms of Bacterial Pathogens* (eds Kudva, I. T. et al.) 481–511 (John Wiley & Sons, 2016).
- David, M. Z. et al. What Is Community-Associated Methicillin-Resistant Staphylococcus aureus? *J. Glob. Infect. Dis.* **197**, 1235–1243 (2008). <https://doi.org/10.1086/533502>
- Appelbaum, P. C. The emergence of vancomycin-intermediate and vancomycin-resistant Staphylococcus aureus. *Clin. Microbiol. Infect.* **12**, 16–23 (2006). <https://doi.org/10.1111/j.1469-0691.2006.01344.x>
- Cattoir, V. & Giard, J.-C. Antibiotic resistance in Enterococcus faecium clinical isolates. *Expert Rev. Anti-infect. Ther.* **12**, 239–248 (2014). <https://doi.org/10.1586/14787210.2014.870886>

14. Lee, C.-R. et al. Biology of *Acinetobacter baumannii*: Pathogenesis, Antibiotic Resistance Mechanisms, and Prospective Treatment Options. *Front. Cell. Infect. Microbiol.* **7**, 55 (2017). <https://doi.org/10.3389/fcimb.2017.00055>
15. Peleg, A. Y., Seifert, H. & Paterson, D. L. *Acinetobacter baumannii*: Emergence of a Successful Pathogen. *Clin. Microbiol. Rev.* **21**, 538–582 (2008). <https://doi.org/10.1128/CMR.00058-07>
16. Pachori, P., Gothwal, R. & Gandhi, P. Emergence of antibiotic resistance *Pseudomonas aeruginosa* in intensive care unit; a critical review. *Genes Dis.* **6**, 109–119 (2019). <https://doi.org/10.1016/j.gendis.2019.04.001>
17. Lister, P. D., Wolter, D. J. & Hanson, N. D. Antibacterial-resistant *Pseudomonas aeruginosa*: clinical impact and complex regulation of chromosomally encoded resistance mechanisms. *Clin. Microbiol. Rev.* **22**, 582–610 (2009). <https://doi.org/10.1128/CMR.00040-09>
18. Wagenlehner, F. et al. Systematic review on estimated rates of nephrotoxicity and neurotoxicity in patients treated with polymyxins. *Clin. Microbiol. Infect.* **27**, 671–686 (2021). <https://doi.org/10.1016/j.cmi.2020.12.009>
19. Imai, Y. et al. A new antibiotic selectively kills Gram-negative pathogens. *Nature* **576**, 459–464 (2019). <https://doi.org/10.1038/s41586-019-1791-1>
20. Luther, A. et al. Chimeric peptidomimetic antibiotics against Gram-negative bacteria. *Nature* **576**, 452–458 (2019). <https://doi.org/10.1038/s41586-019-1665-6>
21. Krauss, S. et al. Secretion of and Self-Resistance to the Novel Fibupeptide Antimicrobial Lugdunin by Distinct ABC Transporters in *Staphylococcus lugdunensis*. *Antimicrob. Agents Chemother.* **65**, e01734–20 (2020). <https://doi.org/10.1128/aac.01734-20>
22. Nicolas, I., Bordeau, V., Bondon, A., Baudy-Floc'h, M. & Felden, B. Novel antibiotics effective against gram-positive and -negative multi-resistant bacteria with limited resistance. *PLOS Biol.* **17**, e3000337 (2019). <https://doi.org/10.1371/journal.pbio.3000337>
23. Ram, G., Ross, H. F., Novick, R. P., Rodriguez-Pagan, I. & Jiang, D. Conversion of staphylococcal pathogenicity islands to CRISPR-carrying antibacterial agents that cure infections in mice. *Nat. Biotechnol.* **36**, 971–976 (2018). <https://doi.org/10.1038/nbt.4203>
24. Stokes, J. M. e. a. A Deep Learning Approach to Antibiotic Discovery. *Cell* **180**, 688–702.e13 (2020). <https://doi.org/10.1016/j.cell.2020.01.021>
25. Booq, R. Y., Tawfik, E. A., Alfassam, H. A., Alfahad, A. J. & Alyamani, E. J. Assessment of the Antibacterial Efficacy of Halicin against Pathogenic Bacteria. *Antibiotics* **10**, 1480 (2021). <https://doi.org/10.3390/antibiotics10121480>
26. Haddad Kashani, H., Schmelcher, M., Sabzalipoor, H., Seyed Hosseini, E. & Moniri, R. Recombinant Endolysins as Potential Therapeutics against Antibiotic-Resistant *Staphylococcus aureus*: Current Status of Research and Novel Delivery Strategies. *Clin. Microbiol. Rev.* **31**, 1 (2018). <https://doi.org/10.1128/cmr.00071-17>
27. Loc-Carrillo, C. & Abedon, S. T. Pros and cons of phage therapy. *Bacteriophage* **1**, 111–114 (2011). <https://doi.org/10.4161/bact.1.2.14590>
28. Salmond, G. P. C. & Fineran, P. C. A century of the phage: past, present and future. *Nat. Rev. Microbiol.* **13**, 777–786 (2015). <https://doi.org/10.1038/nrmicro3564>
29. Zipperer, A. e. a. Human commensals producing a novel antibiotic impair pathogen colonization. *Nature* **535**, 511–516 (2016). <https://doi.org/10.1038/nature18634>
30. Dadgostar, P. Antimicrobial Resistance: Implications and Costs. *Infect. Drug Resist.* **12**, 3903–3910 (2019). <https://doi.org/10.2147/IDR.S234610>

¹Department of Physiology,
McGill University, Montréal,
QC, Canada

Keywords

Tamoxifen, endocrine resistance,
breast cancer, mTOR pathway,
cancer therapy, selective estrogen
receptor modulators, anti-estrogen

Email Correspondence

olivia.dumas@mail.mcgill.ca

<https://doi.org/10.26443/msurj.v19i1.230>

©The Authors. This article is
published under a CC-BY license:
<https://creativecommons.org/licenses/by/4.0/>

Olivia Dumas¹

Endocrine Resistance in Breast Cancer: The Role of mTOR Signaling in Mediating Resistance to Selective Estrogen Receptor Modulators

Abstract

Selective estrogen receptor modulators (SERMs) are chemical compounds that demonstrate agonistic and/or antagonistic effects on estrogen receptors, depending on the specific tissue they target. SERMs that are competitive inhibitors of hormonal estrogens have been widely prescribed and efficacious as a first-line endocrine therapy to treat estrogen receptor (ER)-positive breast cancer. The most widely used SERM in the treatment of breast cancer, tamoxifen, is a prodrug whose active form 4-hydroxytamoxifen (4-OHT) is anti-proliferative in breast tissue. Its widespread use has had a tremendous impact on reducing breast cancer mortality. 4-OHT represses the expression of estrogen-responsive genes involved in cancer growth. The binding of 4-OHT to estrogen receptors prevents the recruitment of coactivators to chromatin. Instead, 4-OHT promotes the recruitment of corepressors and histone deacetylases, thus inhibiting transcriptional activation of target genes. However, the issue of endocrine resistance remains a predominant problem with this therapy. Resistance can arise due to acquired mutations in ER α or dysregulations in the mTOR signaling pathway. By knocking down *YAP/TAZ* or *PSAT1* in the mTOR pathway, we can re-sensitize the breast cancer cells to SERM therapy. Despite this discovery, endocrine resistance remains an issue due to irregularities in additional pathways. Therefore, subsequent research is crucial to identify more targets that, when inactivated, enable re-sensitization of resistant cells, restoring full therapeutic ability of SERMs in afflicted women.

Introduction

The beginning of a woman's reproductive years is marked by the onset of ovulation and menstruation. This transition involves the production of endocrine hormones which stimulate the ovaries to produce a class of female sex hormones known as estrogens, with 17 β -estradiol functioning as the predominant intracellular form. Estrogens play a vital role in the development of the female reproductive system, differentiation of healthy breast epithelium, and maintenance of bone density^{1,2}. This ovarian hormone conducts its physiological effects in its target tissues through stimulation of the estrogen receptor (ER), which exists in two isoforms: ER α and ER β ². Estrogen receptors are nuclear receptors and hormone regulated transcription factors. They control gene expression by binding cognate DNA motifs known as estrogen response elements, located in the regulatory regions of target genes². A functionally relevant region of this receptor is the ligand binding domain (LBD), which is a region with a series of alpha helices that form a hydrophobic pocket enabling ligand binding¹. Within the LBD is located the transcriptional activation function domain 2 (AF-2) which facilitates transcriptional activation of the target genes of the receptor in response to ligand binding by recruiting coactivators to its site¹. As depicted in Figure 1A, following the binding of estrogen to the LBD, the receptor undergoes a conformational change¹. As the estrogen adheres to the hydrophobic binding pocket of its receptor, helix 12 seals the estrogen into place leading to the exposure of the coactivator binding groove, AF-2, which can then recruit coactivator molecules^{1,2}. The dimerization of the receptor then enables the binding of estrogen-response elements to the promoter region of target genes and thus the transcription of these genes^{1,2}. This mechanism enables the transcription of estrogen-responsive genes essential for growth, development, and differentiation in the healthy female.

Although estrogen is an essential hormone for many tissues, the positive effects of estrogen are frequently overshadowed by its negative effects on female health. One of the most detrimental features of estrogen is its promotion of breast cancer. Breast cancer remains the leading cause of death from cancer in women worldwide³. Broadly speaking, breast cancer is pathologically classified into categories: Estrogen Receptor positive (ER+), Progesterone Receptor positive (PR+), Human Epidermal Growth Factor Receptor-2 positive (HER2+) and Triple-Negative, with ER/PR+ breast cancer making up around 70% of all breast cancers diagnosed³. ER+ breast cancers are dependent on active ER signaling which can stimulate proliferation of normal and malignant cells by inducing the activation of growth-regulatory genes. The upregulation of cell proliferation by estrogen increases the number of mistakes made by error-prone DNA repair machinery, resulting in mutation accumulation in the genome, as well as an increase in cancer growth¹. Given this mechanism of cancer growth, ER+ breast cancer tumours are very dependent on estrogen, rendering ER a sought-after therapeutic target. Hormonal therapeutic antagonists of the ER have been successfully used for the last several decades by postoperative patients and by women at high risk of developing ER+ breast cancer to prevent the recurrence of the cancer post surgically, to reduce mortality due to the breast cancer, or to delay the need for chemotherapy².

The predominant treatment strategy for these tumours has been to inhibit aspects of the ER pathway with different pharmacological agents. One of the many endocrine treatment strategies for ER+ breast cancer are SERMs which function as antiestrogens by directly binding to the ER and, consequently, blocking its signaling and activation of downstream target genes². SERMs are chemical compounds that function as agonists or antagonists, or both simultaneously, depending on the target tissue. For instance, ta-

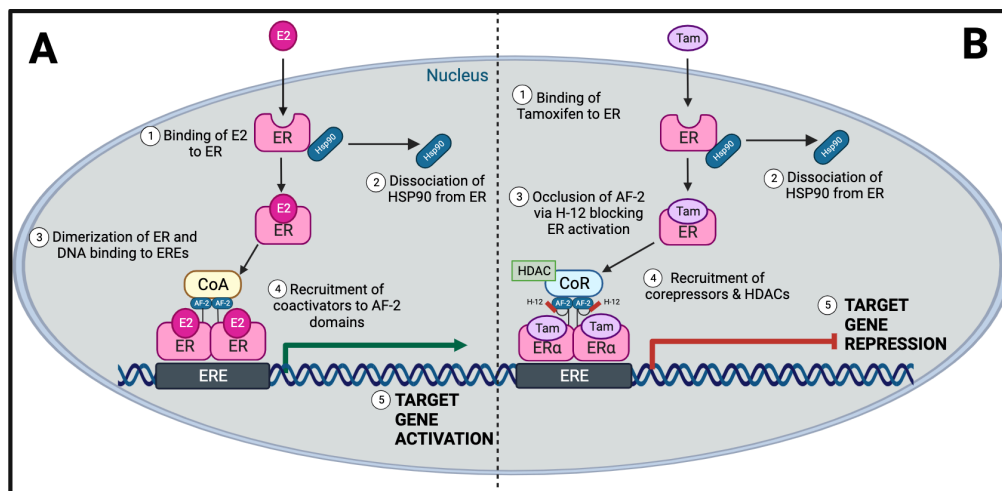


Figure 1. (A) The Mechanism of Action of Estrogen on the Estrogen Receptor¹. Estrogen (E2) diffuses through the plasma membrane and binds to the estrogen receptor (ER). Binding of estrogen to its receptor induces a conformational change, resulting in the dissociation from heat shock protein 90 and dimerization of the receptor. The subsequent complex binds to estrogen-responsive elements (EREs) on the promoter region of estrogen's target genes. One of the ER's domains, AF-2, enables the recruitment of coactivators (CoA) to the transcriptional complex on the estrogen receptor and transcription of the target genes occurs. **(B)** The Antagonistic Action of SERMs in tissues¹. SERMs bind to the estrogen receptor (ER) and confer target gene repression by binding to the estrogen response elements (ERE) on target genes. The SERM will prevent the recruitment of coactivators on the AF-2 domain and instead facilitate the recruitment of corepressors (CoR) and histone deacetylases (HDAC) to the promoter of the genes which will inhibit their transcription.

moxifen was the first relevant SERM discovered for treatment in post-menopausal women suffering from ER+ breast cancer. The active form of this prodrug, 4-hydroxytamoxifen (4-OHT), is anti-proliferative in breast tissue, albeit agonistic in nature in the uterus. Tamoxifen was approved by the FDA in 1977 to treat women with advanced breast cancer following its success in decreasing breast cancer recurrence and the incidence of contralateral secondary tumours by 50% in breast cancer trials¹. Later in 1999, the FDA approved tamoxifen as the first chemo preventative drug to prevent breast cancer in pre- and post-menopausal women¹. While tamoxifen can act as an antiestrogen in the mammary gland, tamoxifen has estrogenic effects in other tissues, notably the uterus⁴. Thus, one of the negative side effects of tamoxifen is an elevated risk of endometrial cancer⁴. This led to the approval and use of another SERM for ER+ breast cancer therapy known as Raloxifene. Raloxifene acts as an antagonist in both breast and uterus tissue eliminating the risk of endometrial cancer^{1,4}. Since then, there have been many SERMs approved for use, all of which differ in their agonist and antagonistic actions depending on the specific tissue they are operating in. Despite the relative efficacy and safety of the application of SERMs in the clinical setting, their successes have been limited by the development of endocrine resistance. Often, when the cancer returns, it may metastasize and become resistant to antiestrogen therapies that were previously effective. It is known that approximately one third of patients with ER+ breast cancer who undergo adjuvant therapy with SERMs develop resistance to the drugs⁴.

As the search for novel targets to re-sensitize the cells to the SERM therapies remains a clinical struggle, this review will concentrate on some of the more recent mechanisms and targets discovered for potential treatment of endocrine resistance. To fully understand cellular resistance to hormonal therapies, the mechanism of action of SERMs in the breast cancer setting, accompanied by experimental evidence, will be provided. The primary focus will be the antagonistic action of tamoxifen on ER+ breast cancer tumours given that its discovery sparked immense research on the use of SERMs in breast cancer therapy.

SERMs and Their Antagonistic Mechanism of Action

SERMs function as antiestrogens by competing with estrogen for binding on the ER, altering its conformation and thus leading to a change in the coregulators that associate with the ER². The binding of the antiestrogen to the ER differs from that of estrogen due to structural differences. Notably, due to the large side chains of the antagonist, helix 12 on the ER is prevented from sealing the ligand into the LBD which would typically occur following estrogen binding. This repositioning of helix 12 occludes the AF-2 coactivator binding groove, preventing the recruitment of coactivators to the site¹. Many early studies on the antagonism of the ER characterized the repositioning of helix 12 following estrogen binding and noted that this is a prerequisite for transcriptional activation, as the repositioning of helix 12 generates a functional AF-2 domain crucial for coactivator recruitment⁵. Occluding the AF-2 domain through a repositioning of helix 12 is the way in which SERMs block the activation of the estrogen receptor^{1,2}.

Additionally, these antiestrogens inhibit the transcription of estrogen-responsive genes by inducing different conformational states of the receptor. These states facilitate the interaction of corepressors with the receptor, which serve to prevent the recruitment of transcriptional machinery to the genes' promoters, and thus represses transcription as portrayed in Figure 1B¹. As previously discussed, the downstream effect of SERMs on ER signaling differs depending on the specific tissues they reside in. Notably, SERMs can act as estrogen agonists in some tissues via the AP-1 tethered pathway¹. This has complicated the field of adjuvant endocrine therapy and has led to a need for more research on these agents. For this review, only the antagonistic ability of SERMs will be examined as the antagonism of SERMs represents a mechanism for impeding breast cancer growth.

Experimental Evidence on the Function of SERMs as Antiestrogens

Both the optimistic and unfavourable discoveries on these endocrine agents have encouraged a vast number of experiments, particularly on tamoxifen. The crystallization of the LBD of the ER α in the presence of estrogen, com-

pared to the domain bound to tamoxifen, provided evidence for side chain interference with the capping over of helix 12. This prevents necessary coactivator recruitment⁶.

Once the structural properties of tamoxifen and its potential as an antiestrogen became of interest, many studies tested the ability of tamoxifen to prevent the transcription of estrogen-responsive genes. In a follow-up study, the effects of estrogen and tamoxifen in breast cancer tumours were supported through evidence of active recruitment of coactivator and corepressor proteins respectively⁷. Researchers used immunofluorescence staining to confirm the colocalization of these proteins with the ER. It was found that the steroid receptor coactivator-1 (SRC-1), which is known to enhance transcription, is expressed with the ER⁶. Additionally, the silencing mediator for retinoid and thyroid hormone receptor (SMRT), a corepressor, was also shown to be expressed with the ER⁶. The recruitment of this corepressor to the estrogen-responsive genes was thought to be the main driver for the antagonist activity of tamoxifen. To examine this, researchers used primary breast tumour cells extracted from patients as well as an MCF-7 breast tumour cell line. Immunoblotting was used to identify the coregulators recruited to the transcriptional DNA complex of the ER on the estrogen-responsive elements (ERE) of genes in the presence of β -estradiol and in the presence of 4-OHT⁶. In the presence of β -estradiol, coactivator SRC-1 expression was increased at the estrogen receptor-ERE complex, whereas there was no expression at the complex in the presence of 4-OHT⁶. In contrast, the expression of corepressor SMRT was increased at the complex in the presence of 4-OHT as compared to control and β -estradiol incubated breast cells⁶. Thus, the recruitment of corepressors was thought to be essential for full antagonistic activity of tamoxifen.

Consistent with many lines of evidence, Fleming et al. suggested that the corepressor proteins recruited to the ER exert their transcriptional silencing effects by recruiting many other regulatory proteins — notably histone deacetylases (HDACs)⁸. Research by Liu et al.⁷ presented this evidence clearly in various experiments. In studying MCF-7 breast cancer cells and using reverse-transcriptase polymerase chain reaction, researchers first confirmed the effect of 4-OHT on the expression of estrogen-responsive genes, notably *pS2* and *C-MYC*⁷. *pS2* protein is a prevailing expressed protein in human ER+ breast cancer and *C-MYC* protein is a master of cell metabolism and proliferation. These characteristics render both genes to be genes of interest in cancer growth research. The repressive ability of 4-OHT on these two estrogen-responsive genes in cancer cells is clearly shown by the reduction of *pS2* and *C-MYC* expression following its addition⁷. It is important to note that this experiment evidently confirmed that the tamoxifen induced recruitment of ER- α and NCoR corepressor to the estrogen-response elements on the promoter regions of *pS2* and *C-MYC* genes. This is consistent with the previously described mechanism of the ER complex binding to estrogen-response elements on target gene promoters. Estrogen-bound estrogen receptors recruit coactivator complexes containing histone acetyltransferases which facilitate the binding of transcription factors leading to gene activation. This raised the possibility that a similar mechanism occurs for tamoxifen-bound ER. Perhaps the previously discovered corepressors like SMRT that are recruited to the ER are also associated with HDACs and it is thanks to their local hypoacetylation on the target genes that tamoxifen functions as an antiestrogen. To explore the nature of this corepressor complex recruited to the tamoxifen-bound ER, researchers exposed MCF-7 breast cancer cells to either estrogen or 4-OHT and isolated the cross-linked chromatin⁷. Using serial chromatin immunoprecipitation and antibodies against two histone deacetylases, HDAC1 and HDAC3, the results demonstrated the following. In the presence of 4-OHT, both HDAC1 and HDAC3 were recruited to the genes' promoters. Furthermore, they found that other components of the NCoR-HDAC3 complex were recruited to the promoters, for instance transducing B-like protein 1 (TBL1)⁷. Further experiments demonstrated similar results for the HDAC1 complex. Histone deacetylases are transcriptional repressors that reduce acetylation

of histones and repress the transcription of genes. Thus, it seems as though the antiestrogen effects of tamoxifen are, in part, due to the recruitment of deacetylases to estrogen-responsive regions⁷.

In summary, the results of this study provide evidence that the silencing effects of tamoxifen on estrogen-responsive genes are thanks to the recruitment of a large transcriptional silencing complex. Their evidence elaborates on the results of the previous study that displayed 4-OHT dependent recruitment of SMRT, as they demonstrated that such corepressors exist in a multiprotein complex containing HDACs and other polypeptides. These HDACs are known to create a repressive chromatin conformation that prevents the interaction of transcription factors and RNA polymerase II — critical molecules for gene expression⁷. In addition, researchers concluded that the promoter-bound OHT-ER is associated with only one of the HDAC complexes at a time; a way to effectively repress target gene transcription via sequential association with the complexes⁷. All in all, it is the transcriptional repression of the ER and its recruited HDACs and corepressors that confers tamoxifen sensitivity to estrogen target genes, such as *MYC*⁹. As more research is undertaken, more ER corepressors are being identified as enhancing the antitumorogenic effects of tamoxifen⁹.

Endocrine Resistance to SERMs: How Can We Resensitize the Cells?

Although the exact mechanism by which cancer recurrence due to endocrine resistance occurs is unknown, over the years, many studies have uncovered several possibilities behind the eventual relapse that most patients face. Importantly, most ER+ breast cancer tumours maintain expression of a functional ER, suggesting mechanisms other than receptor loss³. Several other mechanisms of endocrine resistance include acquired mutations of the ER α , alterations in the ER pathway, amplification of epidermal growth factor receptors, and activation of various growth factor pathways, cell cycle pathways, or apoptosis pathways². This variability has made the battle against endocrine resistance to SERMs a challenging feat. The following analysis will focus on the phosphatidylinositol 3-kinase/activated protein kinase B (PI3K/AKT) signaling pathway and its mediation in conferring estrogen-independent growth properties to ER+ breast cancer cells, leading to endocrine resistance¹⁰. Given that the PI3K/AKT pathway is involved in the promotion of cell proliferation, cell growth, and the inhibition of apoptosis, the pathway has been a predominant therapeutic target for research on re-sensitization mechanisms¹¹.

A way in which ER signaling is altered, and thus endocrine resistance arises, is by ligand-independent ER activation. The PI3K/AKT pathway can protect breast tumour cells from tamoxifen-induced apoptosis since AKT can activate the ER in a ligand-independent manner¹⁰. AKT has been found to inhibit apoptosis and stimulate cell growth, thus contributing highly to the oncogenic transformation of cells¹⁰. The PI3K/AKT pathway functions to upregulate the expression of genes involved in cell proliferation, cell survival, angiogenesis, and tumorigenesis¹². Upon activation of the receptor tyrosine kinase of this pathway by diverse stimuli, the activation of PI3K will occur¹¹. PI3K is highly implicated in cancer and enables the production of phosphatidylinositol (3,4,5)-tris-phosphate (*PIP*₃) which leads to the translocation and binding of AKT to the plasma membrane¹¹. At the membrane, AKT will become partially phosphorylated by phosphoinositide-dependent kinase 1 (PDK1). However, full activation of AKT requires additional phosphorylation from mammalian target of rapamycin (mTOR)^{10,11}. When coupled to its regulatory-associated protein, Raptor, mTOR denoted Raptor, will form the mammalian target of rapamycin complex 1 (mTORC1) which functions to regulate protein synthesis and cell proliferation¹². Protein synthesis is a requirement for cells to be able to divide and grow, thus mTOR signalling is highly implicated in

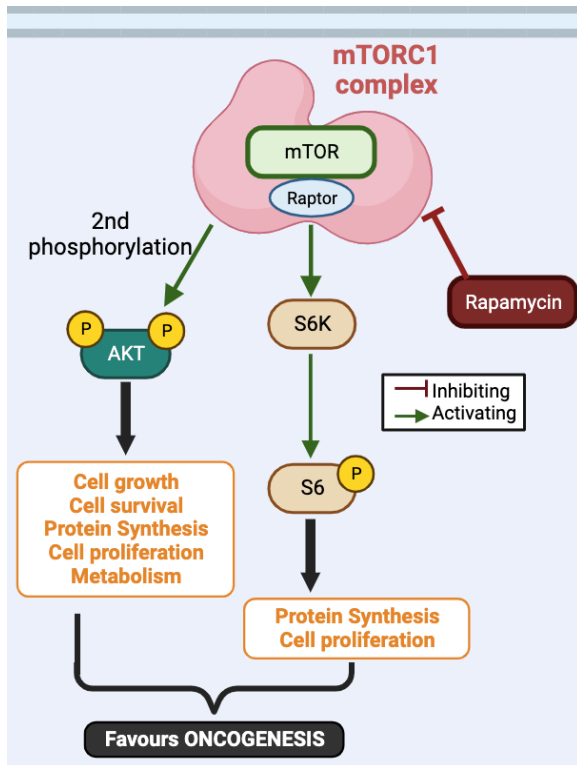


Figure 2. mTORC1 and AKT on the Regulation of Cellular Mechanisms, Favouring Oncogenesis¹¹⁻¹³.

increasing mRNA translation through regulation of its substrates^{11,12}. Notably, mTORC1 will stimulate ribosomal protein S6kinase (S6K), as portrayed in Figure 2, which in turn will phosphorylate ribosomal protein S6 (S6)^{12,13}. These downstream effects on the targets of mTORC1 will promote mRNA translation and cellular proliferation. Once AKT is fully activated by the upstream PI3K and the downstream mTOR, AKT will then go on to phosphorylate many proteins involved in translation, cell growth, proliferation, metabolism, and survival, providing an ideal state for oncogenesis¹¹. Many studies have revealed that high levels of AKT confer resistance to radiotherapy and hormonal therapy and thus survivability to the ER+ breast cancer.

Given that the aberrant signaling of this pathway promotes breast cancer tumorigenesis by inhibiting cell apoptosis, overriding cell cycle control, and upregulating the production of survival factors, preclinical studies have been carried out to study how the inhibition of critical components of this pathway could affect endocrine sensitivity¹⁰. It was consistently found in the field that this inhibition could, in turn, restore hormone sensitivity. Notably, one study by deGraffenried and colleagues explored the effect of the antibiotic rapamycin on inhibiting mTOR to sensitize resistant cancer cells to tamoxifen¹⁰. Rapamycin has been found to induce G1 cell cycle arrest, anti-proliferative effects, and apoptosis in many cancer models with high AKT activity and restore its sensitivity¹⁰. Thus, to elaborate on the implication of rapamycin in breast cancer, the study developed MCF-7 breast cancer cells with high and low AKT activity¹⁰. To explore whether the inhibition of downstream AKT targets with rapamycin could restore sensitivity to tamoxifen in breast cancer cells, researchers treated MCF-7 cells with low and high levels of phosphorylated AKT with increasing amounts of 4-OHT and measured their relative percentage of growth¹⁰. The MCF-7 cells with low expression levels of phosphorylated AKT and the control MCF-7 cells had a dose-dependent decrease to tamoxifen in terms of their growth¹⁰. However, the MCF-7 cells with high AKT activity experienced no growth inhibition indicating resistance to the tamoxifen¹⁰. Next, the researchers cotreated the 3 groups of MCF-7 cells with the mTOR inhibitor rapamycin,

along with 4-OHT. Interestingly, the MCF-7 cells with low AKT activity showed an even greater decrease in growth due to tamoxifen following the addition of the mTOR inhibitor¹⁰. Successfully, the cotreatment of the high AKT activity MCF-7 cells with rapamycin restored sensitivity to tamoxifen as seen by the great reduction in growth percentage¹⁰. This indicates that the mTOR signaling plays an important role in mediating the resistance to tamoxifen and suggests that by inhibiting mTOR signaling with rapamycin, previously resistant breast cancer cells to tamoxifen can be re-sensitized.

Many studies have continued to investigate the role of PI3K/AKT/mTOR pathway in endocrine resistance. In a study from 2022, investigators found that by targeting transcriptional activators that are elevated in tamoxifen-resistant breast cancer cells, the cells can be re-sensitized via a suppression of components of the mTOR pathway⁴. Prior to the execution of this study, it was known that transcriptional regulators Yes-associated protein (YAP) and transcriptional coactivators with PDZ-binding motif (TAZ) are elevated in many cancers. They are known to reprogram the cancer cells into cancer stem cells by inducing expression of target genes involved in cancer initiation, proliferation, and metastasis¹⁴. Thus, they were appealing targets to study in the realm of endocrine resistance. To confirm the elevated levels of YAP and TAZ coactivators in tamoxifen-resistant breast cancer cells, researchers measured growth and cell viability of MCF-7 breast cancer cells and MCF-7 tamoxifen-resistant cells. Using varying doses of 4-OHT, the results showed that the 4-OHT caused a dose-dependent decrease in the viability of the MCF-7 breast cancer cells. However, it had a weak inhibitory effect on the viability of the resistant cells, notably less than a 15% decrease in viability after treatment with 4-OHT, as seen in Figure 3A⁴. To demonstrate that these cells are resistant to cell death, the researchers used the cleavage of poly-ADP ribose polymerase 1 (PARP), a hallmark of cell apoptosis, to measure the cell death induced by 4-OHT⁴. As expected, the resistant MCF-7 breast cancer cells experienced no significant cell death when faced with the SERM, as portrayed in Figure 3B⁴. Given the elevated levels of YAP and TAZ coactivators, the researchers used small interfering RNA machinery to create a knockdown of YAP and TAZ⁴. Using measures for cell viability and apoptosis, they found that this knockdown induced increased PARP cleavage and reduced cell viability in the resistant cells, as seen in Figure 3C when comparing lane 3 to lane 1. This indicates that more cell death of these resistant cells was occurring⁴. When they added 4-OHT to the cells, they found an exacerbation of the previous results, notably there was a larger increase in PARP cleavage and a larger decrease in cell viability⁴. This suggests that by suppressing expression of YAP and TAZ coactivators, the breast cancer cells' sensitivity to tamoxifen increases.

Given that it has been reported that YAP and TAZ induce the expression of an enzyme known as phosphoserine aminotransferase 1 (PSAT1), the next thing researchers wanted to study was whether the knockdown of YAP and TAZ suppresses the expression of PSAT1 in tamoxifen-resistant breast cancer cells⁴. PSAT1 is an enzyme associated with cell proliferation and chemoresistance, thus it was expected to see the elevation of PSAT1 in the tamoxifen-resistant breast cancer cells. Consistent with their predicted outcome, researchers found that the knockdown of YAP and TAZ resulted in a reduction in both the mRNA and protein levels of PSAT1⁴. Furthermore, researchers wished to explore the effects of PSAT1 suppression on the resistant cells' survival. The results from the PSAT1 knockdown showed sensitization of the tamoxifen-resistant cells to tamoxifen given by the reduction in cell viability and increase in cell apoptosis of the MCF-7 resistant cells. Building on the finding of the previous study on the re-sensitization of refractory breast cancer cells to tamoxifen via mTOR inhibition, researchers investigated whether the knockdown of YAP/TAZ or of PSAT1 was resolving the endocrine resistance issue by specifically modulating the mTOR pathway. As previously reported, high AKT activity is proven to be responsible for the cancer growth and is dependent on the phosphorylation by mTOR and PDK1¹⁰. Thus, by inhibiting the activation of mTOR, the AKT should remain partially unphosphorylated and there-

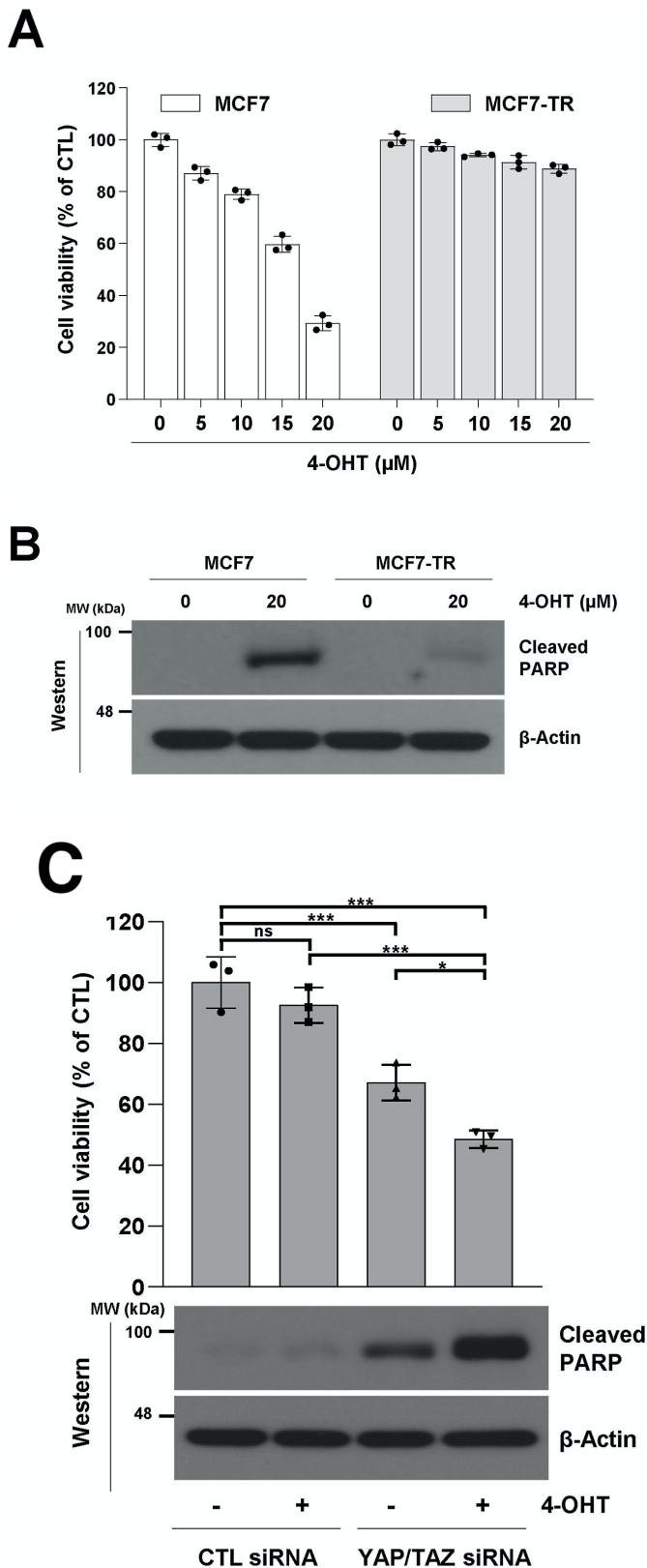


Figure 3. (A) Cell viability of MCF-7 cells and MCF-7 Tamoxifen resistant cells (MCF7-TR) in response to increasing doses of 4-hydroxytamoxifen (4-OHT). Measured using an MTT assay⁴. (B) Assessment of cell death of MCF-7 control cells and MCF-7 tamoxifen resistant cells (MCF7-TR) based on PARP cleavage⁴. (C) Assessment of cell viability and cell death in the control (CTL) siRNA cells and the cells with the YAP/TAZ knockdown (YAP/TAZ siRNA). Additional assessment of the effect of 4-hydroxytamoxifen (4-OHT) treatment to the cells⁴.

fore be unable to induce genes, such as survivin, involved in destructive oncogenic processes. Given the previous results outlined, the researchers speculated that a knockdown in *YAP/TAZ* and *PSAT1* would induce a disruption in mTOR activation, which is characterized by a decrease in S6 and S6K phosphorylation. This speculation was correct as both knockdowns caused a decrease in survivin protein expression following treatment of 4-OHT, which is expected considering a lack of mTOR activation results in less AKT activity and thus less target gene expression. Considering survivin expression is a marker for radiation resistance, these results suggest that by knocking down *YAP/TAZ* or *PSAT1* in resistant breast cancer cells, which in turn reduce the expression of genes involved in endocrine resistance, a re-sensitization to tamoxifen can occur. Re-sensitization through this mechanism may be possible because the knockdowns cause a decrease in mTOR activity and survivin expression which are crucial for cancer progression and endocrine resistance. Both analyzed studies suggest that a downregulation of the components of the PI3K/AKT/mTOR pathway is one mechanism by which tamoxifen-resistant breast cancer cells can be re-sensitized to SERM therapy given that one of the causes is indeed aberrant signaling of this pathway. Follow-up studies on this approach will be necessary to finalize a potential treatment that will be able to conquer this issue.

Conclusion

In summation, SERMs have had a significant impact on breast cancer treatment. While they offer a promising pharmacological profile in reducing breast cancer progression and mortality, many women continue to experience resistance to these agents. In response to this problem, mTOR inhibitors have demonstrated efficacy in restoring sensitivity in resistant cells. However, multiple pathways contribute to endocrine resistance and thus continued research is needed to identify more targets that will counteract this resistance and advance the fight against this formidable disease.

References

- Lewis, J. S. & Jordan, V. C. Selective estrogen receptor modulators (SERMs): Mechanisms of anticarcinogenesis and drug resistance. *Mutat. Res./Fundam. Mol. Mech. Mutagen.* **591**, 247–263 (2005). <https://doi.org/10.1016/j.mrfmmm.2005.02.028>
- Patel, H. K. & Bihani, T. Selective estrogen receptor modulators (SERMs) and selective estrogen receptor degraders (SERDs) in cancer treatment. *Pharmacol. Ther.* **186**, 1–24 (2018). <https://doi.org/10.1016/j.pharmthera.2017.12.012>
- Haque, M. M. & Desai, K. V. Pathways to endocrine therapy resistance in breast cancer. *Front. Endocrinol.* **10**, 448521 (2019). <https://doi.org/10.3389/fendo.2019.00573>
- Kim, Y. J. et al. Knockdown of YAP/TAZ sensitizes tamoxifen-resistant MCF7 breast cancer cells. *Biochem. Biophys. Res. Commun.* **601**, 73–78 (2022). <https://doi.org/10.1016/j.bbrc.2022.02.083>
- Brzozowski, A. M. et al. Molecular basis of agonism and antagonism in the oestrogen receptor. *Nature* **389**, 753–758 (1997). <https://doi.org/10.1038/39645>
- Shiau, A. K. et al. The structural basis of estrogen receptor/coactivator recognition and the antagonism of this interaction by Tamoxifen. *Cell* **95**, 927–937 (1998). [https://doi.org/10.1016/s0092-8674\(00\)81717-1](https://doi.org/10.1016/s0092-8674(00)81717-1)
- Liu, X. & Bagchi, M. Recruitment of distinct chromatin-modifying complexes by tamoxifen-complexed estrogen receptor at natural target gene promoters in vivo. *J. Biol. Chem.* **279**, 15050–15058 (2004). <https://doi.org/10.1074/jbc.m311932200>

8. Fleming, F. J., Hill, A. D., McDermott, E. W., O'Higgins, N. J. & Young, L. S. Differential recruitment of coregulator proteins steroid receptor coactivator-1 and silencing mediator for retinoid and thyroid receptors to the estrogen receptor-estrogen response element by β -estradiol and 4-hydroxytamoxifen in human breast cancer. *J. Clin. Endocrinol. Metab.* **89**, 375–383 (2004). <https://doi.org/10.1210/jc.2003-031048>
9. Légaré, S. & Basik, M. The link between ERA corepressors and histone deacetylases in tamoxifen resistance in breast cancer. *Mol. Endocrinol.* **30**, 965–976 (2016). <https://doi.org/10.1210/me.2016-1072>
10. deGraffenried, L. A. et al. Inhibition of mTOR activity restores tamoxifen response in breast cancer cells with aberrant AKT activity. *Clin. Cancer Res.* **10**, 8059–8067 (2004). <https://doi.org/10.1158/1078-0432.ccr-04-0035>
11. Hasson, S. P., Rubinek, T., Ryvo, L. & Wolf, I. Endocrine resistance in breast cancer: Focus on the phosphatidylinositol 3-kinase/AKT/mammalian target of rapamycin signaling pathway. *Breast Care* **8**, 248–255 (2013). <https://doi.org/10.1159/000354757>
12. Hemmings, B. A. & Restuccia, D. F. PI3K-PKB/Akt pathway. *Cold Spring Harb. Perspect. Biol.* **4**, a011189 (2012). <https://doi.org/10.1101/cshperspect.a011189>
13. Foster, K. G. &ingar, D. C. Mammalian target of rapamycin (mTOR): Conducting the Cellular Signaling Symphony. *J. Biol. Chem.* **285**, 14071–14077 (2010). <https://doi.org/10.1074/jbc.r109.094003>
14. Piccolo, S., Dupont, S. & Cordenonsi, M. The Biology of YAP/TAZ: Hippo Signaling and Beyond. *Physiol. Rev.* **94**, 1287–1312 (2014). <https://doi.org/10.1152/physrev.00005.2014>

¹Department of Microbiology and Immunology, McGill University, Montréal, QC, Canada

Keywords

Leishmania, extracellular vesicles, vaccine platform, SARS-CoV2

Email Correspondence

susan.cai@mail.mcgill.ca

<https://doi.org/10.26443/msurj.v19i1.213>

©The Authors. This article is published under a CC-BY license: <https://creativecommons.org/licenses/by/4.0/>

Susan Cai¹

The Use of *Leishmania*-Derived Extracellular Vesicles as a Vaccine Platform against Emerging Viral Diseases

Abstract

Extracellular vesicles (EVs) are small membrane-bound “vehicles” responsible for transporting biological materials from source cells to target cells. EVs are thus indirectly capable of inducing changes in the physiological state and behavior of target cells once their contents are successfully released or received. Both prokaryotic and eukaryotic species utilize EVs for a variety of purposes. For example, *Leishmania*, a protozoan parasite, has demonstrated the ability to secrete immunomodulatory EVs. Various studies have shown that it is not these EVs in themselves, but rather the contents of these EVs that are directly involved in the parasite’s colonization and replication inside host cells. Although using *Leishmania* as an expression system for recombinant proteins has been explored (investigations have yielded successful and promising results), the use of *Leishmania*-derived EVs is a burgeoning field of research. In fact, considering extant research on EV-based vaccines, substantial potential lies in exploiting *Leishmania*-derived EVs as a novel vaccine platform. Hence, this study aims to discuss the immunomodulatory capabilities of *Leishmania*-derived EVs and their potential application in vaccine development. Lastly, in piecing together the nature of *Leishmania*-derived EVs and the general therapeutic potential of engineered EVs, it is further hypothesized that *Leishmania* may be an effective expression system for EVs that harbour desired viral antigens as a part of more efficient vaccine designs.

Introduction

Over the last 15 years, investigative research in several biological fields of science has developed a great interest in the entities secreted by eukaryotic cells¹. Extracellular vesicles (EVs), in particular, have garnered significant attention as they are extraordinarily diverse cargo carriers heavily enriched in proteins, lipids and nuclear material^{1,2}. Although EVs are involved in various biological processes, these vesicles ultimately mediate regulated cell-to-cell communication for both bacterial and eukaryotic cells². Thus, the communication network created by EVs is seen as highly efficient system for the induction of proximal and distant cellular responses².

It is important to note that EVs are not a homogenous population. There exist many different types of EV; in fact, various classification systems were established to create sub-populations based on their biogenesis, release pathway(s), size content and function². Currently, three main subtypes have been identified: microvesicles (MVs), exosomes and apoptotic bodies. However, despite identifying these three distinct groups, current technological methods still struggle with accurate differentiation³.

Within the growing body of literature on EVs, a select number of studies focus on the production of EVs in pathogenic protozoan parasites. Research has demonstrated that parasites are typically highly sensitized to their environments; as such, they are intrinsically capable of modulating host responses to evade elimination or neutralization tactics⁴. Initial studies proposed that soluble parasite factors were solely responsible for this form of parasite-to-host communication. However, recent evidence has suggested that parasite-derived EVs are key players in mediating these processes. In particular, the immuno-modulatory capabilities of *Leishmania*, a zoonotic protozoan parasite, present a highly unique parasite-to-host dynamic³. Initially demonstrated by Silverman and colleagues in 2008, it has since become well-established that various *Leishmania* species secrete exosomes carrying active proteins and RNAs that may impede macrophage

signalling and anti-microbicidal activities⁴⁻⁶. However, the full role, effects and biotechnological potential of these protozoan EVs remains largely under-appreciated.

On the other hand, other forms of EV research have focused on utilizing them as a delivery mechanism. As described, EVs possess a remarkable ability to transmit large amounts of biological material, therefore making them befitting candidates for drug or vaccine use¹. In fact, success with EV-based therapies has already been documented in anti-cancer research. For example, exosomes derived from tumours have demonstrated the ability to induce anti-tumor responses through the delivery of immuno-stimulatory factors⁷. There exists a high degree of biocompatibility with this line of therapy, as the exosomes are derived from cultured tumours⁷.

Ultimately, the rising interest in EVs stems from their unique therapeutic potential as a safe and biocompatible alternative to other traditional and novel avenues in immunotherapy⁷. Currently, studies have shown that EVs derived from excised tissue samples will not induce any detrimental genotoxic, hematological or immunological effects when re-introduced into the organism of origin^{8,9}. It is important to understand that an EV itself is not inherently immunogenic. As EVs are derived from endogenous tissues, the body is already conditioned to tolerate them. Similarly, pathogen or exogenously derived EVs will typically mimic a host’s tissues to prevent detection⁸. Hence, the introduction of an EV alone (without any alterations) should not trigger inflammation or detrimental consequences⁸. The stimulatory effects of EV-based therapies are truly dependent on the contents of the EV and their regulated release at the appropriate targets⁷. Thus, in the context of vaccines, engineered EVs represent a flexible and safe strategy to create a treatment that is free of attenuated viruses or virus-like particles (VLPs)⁷.

This study aims to conduct a systematic review of the immune-modulatory capabilities of *Leishmania*-derived EVs and their potential use as a novel

vaccine candidate against emerging viral diseases. This will be achieved by summarizing extant research on the molecular mechanisms of *Leishmania*-derived EV immunomodulation and the successes and challenges in EV use. It is rationalized that because *Leishmania*-derived EVs possess unique immunomodulatory capabilities, they promise a solution that may combat overly aggressive immune responses (i.e., Cytokine Response Syndrome) against novel viral diseases. Moreover, due to the inherent biocompatibility of EVs, they may prove to be a highly effective and safer alternative to other vaccine candidates.

Methods

This review was conducted using PubMed and Google Scholar with search terms ('Extracellular vesicles' AND 'Leishmania'), ('Leishmania' AND 'viral vaccin*'), and ('Extracellular vesicle' AND 'viral vaccin*'). Initial searches returned 92 articles which were then screened via their abstracts for relevance to the topic and for providing background information. Priority was given to primary research articles published after 2019, following the last major review on extracellular vesicles by Dong et al. in 2019. The remaining papers were then assessed for relevancy by reading titles and abstracts. For further details on the selection criteria applied during the screening process, see Table 1. Overall, the literature search supporting this review sought to find sources that could address the following questions: "(1) Why might *Leishmania* EVs serve as a better vaccine platform than current vaccine designs? (2) How can *Leishmania* EVs be modified so that they can be used to induce protective immunity against emerging viral diseases?" Ultimately, 25 papers were deemed relevant and included in this review.

Table 1. Screening Criteria for the Selection of Articles

Component	Inclusion criteria	Exclusion criteria
Title	Mentions EVs and/or (more specifically) <i>Leishmania</i> EVs	
	Mentions or implies the use of <i>Leishmania</i> as an expression system	
	Implies the use of <i>Leishmania</i> EVs in a biotechnology capacity/context	
Abstract	Mentions of the subsequent immune response following exposure to <i>Leishmania</i> EVs	
	Mentions of the immunomodulation capacities of <i>Leishmania</i> via their production of EVs	
	Identifies the factors that typically make <i>Leishmania</i> EVs virulent	
	Use of EVs as a (potential) viral vaccine platform	Use of EVs as a diagnostic tool
	Peer-reviewed and published in an academic journal	

Results

Immunomodulation conducted by *Leishmania*-derived EVs

Leishmania possess strategies to evade or subvert the effector mechanisms of macrophages⁸. The inhibition of macrophage activity is largely attributed to the counteractivity of a diverse range of *Leishmania*-derived virulence factors. Various studies have revealed that two key factors, lipophosphoglycan (LPG) and GP63, in particular, are crucial to orchestrating the interaction between the parasite and host (Figure 1)⁸.

LPG is a highly abundant *Leishmania* surface molecule known to inhibit the mounting of robust anti-parasitic responses—thereby promoting parasitic survival within macrophages. Infection studies conducted with LPG-defective species of *Leishmania* revealed a considerable decrease in intracellular parasitic colonization and replication, increased expression of cellular nitric oxide synthase (iNOS) and enhanced Mitogen Activated Protein Kinase (MAPK) activation compared to their wild-type counterparts. Prior work with infection models has clearly established that the activity of iNOS to produce intracellular NO is vital to the elimination of *Leishmania*¹⁰. Authors, Prive and Descoteaux, have hypothesized that LPG preferentially inactivates MAPK to interfere with intracellular signalling, thus resulting in a cascade of effects across the host's ability to resist infection. Although other signal transducers (such as c-JUN N-terminal kinase and ERK 1/2) were identified as targets of LPG, the full extent of the downstream effects remains unclear^{3,9}.

Similarly, GP63 is a Zinc-dependent metalloprotease also expressed at high levels on the surface of the promastigote form of *Leishmania* species¹¹. Classically, it is thought that once the parasite is phagocytosed by a host cell, GP63 would be released and spread across the cytosol of the infected cell. From there, GP63 cleaves several of host cell proteins involved in the regulation of microbicidal functions^{3,11}. Projects such as that of Joshi and colleagues have utilized *L. major* GP63 KO mutants and have observed decreased virulence both *in vitro* and *in vivo*^{10,12}. Interestingly, despite both factors initially being described as surface proteins, proteomic studies conducted within the past decade have revealed that *Leishmania*-derived EVs contain high quantities of both factors^{3,8}. These findings appear to be consistent across a number of *Leishmania* species, including *L. donovani* and *L. braziliensis*¹¹. Besides LPG and GP63, the contents of *Leishmania*-derived EVs also include proteins such as elongation factor-1 α (EF-1 α), fructose-1,6-biphosphate aldolase (FBA), HSP70 and HSP90 as well as small non-coding RNAs (Figure 1)^{8,12}.

Furthermore, it has been observed that infected cells or cells stimulated by parasitic components can also release EVs of their own (Figure 1). These EVs contain messenger RNA (mRNA), small noncoding RNAs, chromosomal DNA, mitochondrial DNA and major histocompatibility complexes (MHC) (Figure 1)⁸. Although much remains unknown about the exact downstream effects of these molecules, it is presumed that they may influence the behavior of proximal leukocytes¹¹. These findings have ultimately contributed to the ever-growing theory that *Leishmania* and their EVs possess highly effective immunomodulatory capabilities that hold great biotechnological potential⁸.

Use of *Leishmania* as an expression system for engineered EVs

Advancements in gene cloning technology over the past couple of decades have made it feasible to express therapeutic proteins and agents in a variety of hosts¹³. However, it remains a considerable challenge to find an appropriate expression system that will produce substantial and quality yields of the protein of interest cost-effectively¹³. Of the various prokaryotic and eukaryotic systems explored, non-pathogenic *Leishmania* species have stood out as candidates with high potential¹³. Among these species, *Leishmania*

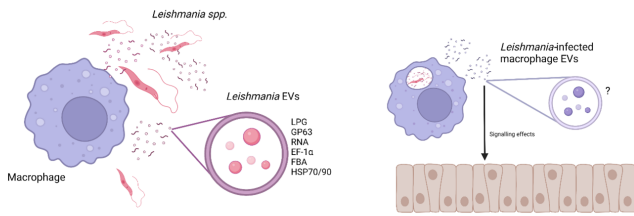


Figure 1. Contents of *Leishmania*-derived EVs contribute to their colonization and replication in macrophages. Proteomic studies of the EVs secreted by various species of *Leishmania* have revealed that they contain molecules such as LPG, GP63, RNAs, elongation factor 1 (EF-1a), and heat shock protein (HSPs). Further investigations of the molecular behavior of LPG and GP63 have demonstrated that they are directly responsible for inhibiting intracellular microbicidal features of the macrophage. Macrophages that have been infected by *Leishmania* are known to also secrete EVs. Contents of these EVs include RNAs, DNA and MHCs. (Adapted from Zauli et al.)¹² (Created with Biorender.com)

tarentolae is one of the more attractive species as it can be cultured in inexpensive media at 26 °C and in large batches with a fairly short generation time (approximately 5–6 hours)^{13–15}. Studies conducted in the late 2000s have shown that *L. tarentolae* can produce high yields of recombinant proteins. Since then, this non-pathogenic species has become widely used for gene manipulation, gene targeting, gene function studies and the generation of live vaccines¹³. The broad range of post-translation modification mechanisms, such as mammalian-type N-glycosylation has made *L. tarentolae* a considerably compatible expression system¹⁵.

It was initially unclear whether *L. tarentolae* was among the species of *Leishmania* that secreted EVs. This uncertainty stemmed partly from the heavy focus on pathogenic species of *Leishmania*, given the widely recognised role of EV secretion in supporting parasitic survival and pathogenesis¹⁴. However, a recent study by Shokouhy and colleagues revealed through electron microscopy-captured images that *L. tarentolae* secretes EVs, and that these EVs contain GP63¹⁴. Moreover, when examining the effects of *L. tarentolae*-derived EVs on THP1 macrophages, the observed increase in pro-inflammatory cytokine levels suggested that despite being non-pathogenic, *L. tarentolae*-derived EVs will still induce an immune response¹⁴.

It should be noted that the current research continues to elucidate the pathways involved in protein sorting and loading for EV secretion¹⁴. Reports indicate that only 5–9% of all proteins present in *Leishmania* EVs contain a signal peptide. Hence, it is speculated that unconventional mechanisms may be involved¹⁴.

EV-based vaccine proposals against novel/(re-)emerging viral diseases

Currently, four major vaccine technologies and platforms are used extensively for the production of antiviral vaccines: (i) RNA vaccines (delivered through lipid-based nanoparticles) (ii) adenovirus-based viral vectors (iii) subunit vaccines (typically produced in eukaryotic expression systems) and (iv) inactivated or attenuated viruses^{15,16}. However, the inherent limitations of these vaccine platforms are exacerbated in the face of novel and complex viruses. Namely, traditional expression or production systems may lack the appropriate post-translation modification mechanisms to enhance the biocompatibility of recombinant protein components. Furthermore, the lifespan of certain vaccinal components may be shorter than what is desired or needed^{16,17}. Additionally, the delivery of immunogenic stimulants and antigens to the appropriate tissues may greatly impact the efficacy of the vaccine¹⁸. Considering these concerns, a new interest in the use of EVs as a vaccine platform has emerged¹⁹. Not only can EVs induce a strong immune response by guiding cell communication, but they can be engineered to display specific viral antigens for the activation of lymphocytes¹⁹.

Moreover, in the context of viral infections, it has been reported that CD63+/CD81+ EVs loaded with viral peptides are released from monocytes to induce the production and release of interferon- γ from CD8+ T cells in an antigen-specific manner¹⁹. As such, research has sought to exploit this biological feature and construct vaccine designs based on antigen-loaded EVs. In two critical studies, Montaner-Tarbes and colleagues demonstrated that CD63+/CD81+ EVs loaded with porcine respiratory and reproductive syndrome virus (PRRSV) antigens were generated during the natural progression of the disease²⁰. Moreover, intramuscular administration of these antigen-loaded EVs into healthy hosts successfully elicited a specific IgG immune response. Further investigations demonstrated that even high doses of these EVs did not trigger clinical symptoms associated with PRRSV²⁰.

However, as not all viruses appear to induce the production of antigen-loaded EVs, ongoing research has proposed EV engineering as an alternative approach. EV engineering involves artificially adding antigens of interest into or onto these vesicles, thus mimicking the previously described antigen-loaded EVs. Currently, greater success has been achieved by directly modifying cells to produce EVs loaded with the antigens of interest¹⁹. This is opposed to the lower degree of success seen amongst attempts to load pre-existing EVs with antigens through methods such as electroporation. When utilizing a cell-based approach, researchers will transduce cells to produce an EV-specific protein fused to the antigen of interest. In this respect, Anticoli et al., have managed to create cell-derived EVs embedded with various viral antigens such as HPV E7, Ebola VP24/VP40/NP, Influenza NP, West Nile NS3 and hepatitis C virus (HCV) NS3²¹. Subsequent testing of these EVs in intramuscular vaccines induced a specific and enhanced immune response from CD8+ T cells without inducing detrimental over-inflammation²¹.

Overall, with growing evidence demonstrating their potency and safety, several biotech companies have already begun to design virus and adjuvant-free vaccines against Chikungunya, Zika, Dengue, West Nile and coronaviruses¹⁹. In particular, through the recent global outbreak of the novel coronavirus, Severe Acute Respiratory Syndrome Coronavirus 2 (SARS-CoV2), a great deal of interest in creating an EV-based vaccine against SARS-CoV2 has developed. As the highly conserved viral Spike (S) protein is primarily responsible for viral entry into host cells, researchers have altered and stripped it to its core domains for embedding onto EVs²². However, among the four following examples leading in this field of research, the actual construction of the EV varies slightly from company to company¹⁹. Alternatively, some companies have chosen to combine the EV-based vaccine approach with aspects of the DNA-based vaccine approach.

Notably, the company Capricor Therapeutics has achieved success in transfecting HEK293 cells with vectors expressing the four structural SARS-CoV2 proteins to induce the production of EVs carrying all four viral antigens in their native configuration (Figure 2A) Although the S protein mediates viral entry, previous work has shown that immunization with multiple proteins allows for greater range in the modulation of the immune response.

Capricor Therapeutics has also formulated a second vaccine design based on an alternative mRNA approach. Having designed mRNAs for a modified S protein, a full-length N protein, and soluble fragments of the M and E proteins, researchers at Capricor Therapeutics and John Hopkins University then fused these to a Lamp1 mRNA transcript for optimal antigen presentation in the context of MHC (Figure 2B). This strategy is grounded on the well-established knowledge that Lamp1 undergoes intracellular degradation into smaller peptides by the MHC pathway in antigen-presenting cells²². When the proposed vaccine was administered intramuscularly into mice at various concentrations, the animals showed a concentration-dependent antibody response for both S and N proteins²².

The Ciloa Company has also developed an EV-based vaccine against SARS-CoV2 called CoVEVax (Figure 2C). Similar to Capricor Therapeutics, the EVs are derived from transfected HEK293 cells. Although little public information exists on how Capricor Therapeutics guides the translocation of the viral proteins onto the surface of the EV during its genesis, Ciloa has described CoVEVax to utilize their patented EV-sorting peptide, CiPP²². Unlike the Capricor Therapeutic design, Ciloa has chosen to only include a modified version of the S protein (Figure 2C)²². Testing of this vaccine proposal has elicited adequate levels of specific IgG production and enhanced IFN- γ production (Figure 3A and 3B)²².

A third biotech company, Codiak BioSciences, has also presented a similar vaccine to that of Ciloa's. Named the exoVACC, the proposed design uses a proprietary engEX platform (built around a central scaffolding protein called PTFGRN) to preferentially sort and display the viral S protein on EVs (Figure 2D)^{19,23}. As of July 2022, Codiak BioSciences had partnered with the Coalition for Epidemic Preparedness Innovations (CEPI), to continue with preclinical studies as exoVACC had demonstrated the ability to stimulate a broad immune response comprising of both humoral and cell-mediated immunity²³. Unfortunately, Codiak BioSciences, on March 27, 2023, news was released that Codiak BioSciences has filed for bankruptcy and will no longer be continuing with the development of exoVACC²⁴.

Finally, Versatope Therapeutics has proposed an EV-based vaccine that uniquely uses the nano-sized vesicles sourced from bacterial cells (Figure 2E). Known as Outer Membrane Vesicles (OMVs), they possess a high degree of similarity to human EVs. Using an OMV-anchoring protein called cytolysin A (ClyA), Versatope has engineered OMVs to display a modified version of the viral S protein (Figure 2E)²⁵. Although previous studies using OMVs have demonstrated success in eliciting adequate immune responses against the H1N1 influenza virus and MERS-CoV, there remain concerns over the biosafety of bacterial-derived OMVs²⁶.

Evidence of the efficacy of EV-based vaccination

Of the various proposals described above, some have demonstrated promising results in their ability to elicit an appropriate cell-mediated and humoral immune response. Of the five proposals, the Ciloa Company's design has directly demonstrated great capacity in promoting viral antigen-specific IgG antibodies and IFN- γ production in pre-clinical trials¹⁹. When testing their proposal *in vivo*, Ciloa utilized a two-component vaccine comprised of the DNA that encodes for the fused S protein-EV complex (DNA^{S-EV}) and the S-EVs themselves²². Prior *in vitro* testing demonstrated that the inclusion of the DNA^{S-EV} allows for *in situ* production of the desired EV²². Ciloa predicted that *in situ* production would lead to the genesis of a more robust form of immunological memory²².

To test the vaccine's efficacy, the study administered various alterations of the proposed design, alongside the original design, to generate comparative data. The first of the experimental groups received the original vaccine design containing both DNA^{S-EV} and S-EVs; the second group received injections containing DNA^{S-EV} and the S protein itself; and finally, the last group received injections containing only S-EVs²². To then quantify the subsequent immune responses, sera samples were drawn from each group and their antibody concentration levels were measured using an indirect ELISA²². Results demonstrated that mice immunized with PBS possessed no circulating antibodies (Figure 3A). ELISA results from the DNA^{S-EV} and S-EV group and the DNA^{S-EV} and S protein group demonstrated a moderate humoral response, while results obtained from the S-EVs-only group demonstrated the highest antibody titers (Figure 3A)²². However, to ensure that the vaccine could elicit more than antibody production (i.e. the vaccine could stimulate pro-inflammatory cytokine production), a separate ELISA was performed to quantify the concentration of IFN- γ in the extracted sera samples. Unlike the results obtained when quantifying antibody titers, the S-EV-only group demonstrated the lowest IFN- γ concentrations (Figure 3B)²². Hence, it was concluded by Ciloa that both components, the DNA^{S-EV} and the S-EVs, are necessary to induce a proper and protective immune response.

Ciloa's success in creating an EV-based vaccine against SAR-CoV2 that elicits an appropriate and desirable immune response (the production of virus-specific antibodies) is extremely promising to the broader field of EV-based therapeutic research. Further research is needed to determine vaccine kinetics and the longevity of the induced immunity before testing can proceed to stages such as clinical trials.

Discussion

With great potential for a diverse range of clinical applications, the study of EVs has become increasingly popular. Ultimately used as a form of cell-to-cell communication, their ubiquity amongst prokaryotic and eukaryotic cell types contributes greatly to their high degree of biocompatibility and flexibility¹⁹. Of the various applications currently under investigation, substantial attention has fallen on the development of EV-based vaccines against viral diseases. EVs can be modified to present viral antigens, thus mimicking the appearance of a viral particle without the need for pathogenic substances. Furthermore, as several viral vaccines are based on viral vectors, particularly adenoviruses, one of the primary limitations is natural, pre-existing immunity against these vectors²². Pre-existing immunity often implies that the individual's immunological memory will induce an anti-adenovirus immune response, thus overriding and hampering any immune response against the virus of interest²². Due to the localization of memory lymphocytes in the periphery, immunological memory will respond far faster than any attempt to generate a novel immune response²⁷. In the context of emerging viruses, one of the major concerns is the threat of continued re-infections in the general population, thereby driving a virus to become endemic. As seen with the influenza virus, a combination of its enhanced mutation rate and the population's lack of long-lasting immunity has necessitated yearly vaccination campaigns—which may be less feasible for emerging viruses that are of greater immunogenicity²². EV-based vaccines overcome these problems. By preserving the native (or near-native) configuration of viral antigens for display on the EV, the elicited immune response is not only more robust, but studies have shown that its administration leads to enhanced B cell receptor (antibody) crosslinking and circulation as well as memory CD8+ T cell expansion and survival²².

Albeit, that is not to say that EV-based vaccines do not introduce a new set of challenges. Although their ubiquity provides a great deal of flexibility for modifications to resolve biocompatibility issues, a single body of EVs generated from a single cell type may still be a heterogeneous population.

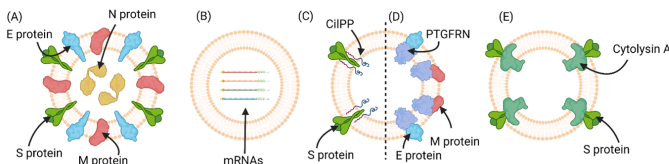


Figure 2. EV-based vaccine designs from various biotechnology companies. (A) By transfecting HEK 293 cells, Capricor Therapeutics have successfully created EVs embedded with/containing S, M, E and N proteins of SARS-CoV2 in their native configurations. (B) Capricor Therapeutics has also successfully loaded EVs with mRNAs for full-length S protein, as well as modified M, E and N proteins of SARS-CoV2. (C) The Ciloa Company has successfully created an EV that displays a modified version of the SARS-CoV2 S protein by using a proprietary EV-sorting peptide called CiPP. (D) Similarly, Codiak BioSciences has created an EV that displays various SAR-CoV2 proteins that have been sorted into the EV using the scaffold protein, PTFGRN. (E) Using a bacterial OMV, Versatope Therapeutics has created an EV that displays Spike protein by fusing it the OMV-anchoring protein cytolysin A(ClyA). (Adapted from Sabanovic et al.)¹⁹ (Created with BioRender.com)

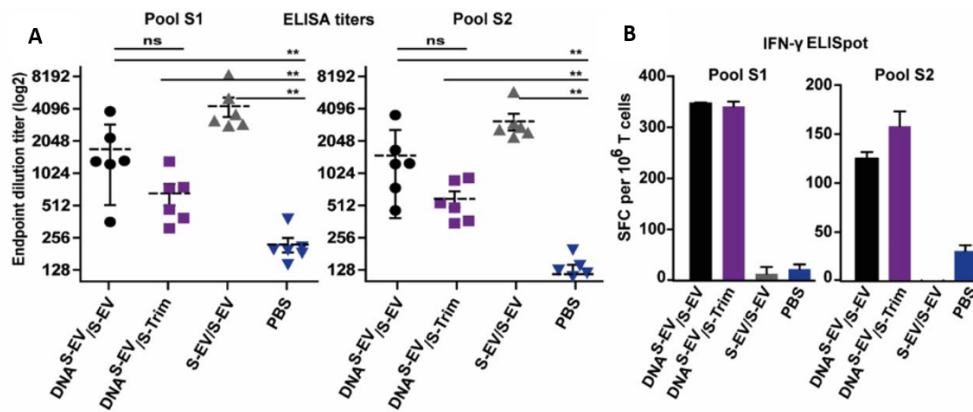


Figure 3. Quantified immune responses after immunizing mice with the Ciloa Company's proposed EV-based vaccine design²². (A) Using an ELISA to quantify the levels of IgG antibodies specific to the SARS-CoV2 S protein complex (designed and constructed by Ciloa), it was demonstrated that three injections of S-EVs alone would elicit the greatest production of antigen specific antibodies²². (B) Conversely, when quantifying the levels of IFN- γ produced following immunization, mice injected with S-EVs alone did not demonstrate increased IFN- γ levels; instead, mice immunized with a combination of DNAS-EV and S-EVs/the S protein complex itself were observed to produce greater levels of IFN- γ . Hence the Ciloa Company has concluded that both are necessary for a protective and effective vaccine²².

Moreover, this issue is further exacerbated by the lack of efficient technological methods to identify the contents of and sort through a large population of EVs^{3,19}. However, ongoing research has already begun to formulate solutions. Studies focused on the identification of increasingly specific EV sub-types, and the standardization of EV-based fluorescence-activated “cell” sorting (FACS) protocols are gradually closing this technical gap^{3,28}.

In light of this, this review proposes that exploiting the immunostimulatory properties of *Leishmania*-derived EVs for EV-based vaccine designs should be explored further. Since these *Leishmania*-derived EVs are immunogenic by themselves but not directly responsible for pathogenesis, engineering *Leishmania* models to produce ‘pre-loaded’ EVs may be an effective improvement to current EV-based vaccine designs⁸. Given the success of Ciloa's vaccine in eliciting the production of desirable antigen-specific antibodies, there is strong evidence that using EV-based vaccine design may be worthwhile to research. Furthermore, as it has been shown that *Leishmania* expression systems can be temporally efficient, cost-effective and compatible with mammalian-derived recombinant proteins, relying on *Leishmania* expression systems may resolve issues with the upscaling of vaccine production¹³. Current industry-standard practices for the production of recombinant EVs use either a yeast-based expression system or transfected immortalized cell lines^{29–31}. Although most yeast species produce glycosylated proteins, these end-products are not fully humanized, which results in downstream issues concerning compatibility when employed in a therapeutic context for humans³⁰. Efforts have been made to genetically alter existing yeast species using CRISPR/Cas9 systems to create new strains with enhanced abilities to produce humanized protein products, but further research is needed to assess whether this would make the overall workflow more efficient while maintaining adequate accuracy³⁰. Additionally, the use of transfected immortalized cell lines (such as HEK293 cells) for EV production presents unique challenges during the purification stage. As the EVs released by transfected cells share similar size and biophysical characteristics as the lentivirus (LV) used to transfect, EVs and LVs are often co-purified together³¹. The lingering presence of LVs in the final EV-based vaccine product would be considered an “impurity” that could potentially induce off-target immune responses³¹.

Altogether, given the works reviewed and described in this review, the natural biocompatibility, immunogenicity, and low-cost nature of *Leishmania*-derived EVs make them a preferable vaccine platform. Moreover, emerging studies have already begun tapping into the biotechnological potential of *Leishmania* EVs for potential vaccines against emerging viral diseases.

This review foresees and suggests that further research into how *Leishmania* can be exploited as an expression system could facilitate greater growth for the prospects of EV-based vaccines.

Acknowledgements

This author would like to express their gratitude towards Dr. Christopher Fernandez-Prada for their guidance throughout the writing of this paper.

References

- Olivier, M. & Fernandez-Prada, C. *Leishmania* and its exosomal pathway: a novel direction for vaccine development. *Future Microbiol.* **14**, 559–561 (2019). <https://doi.org/10.2217/fmb-2019-0087>
- Doyle, L. M. & Wang, M. Z. Overview of extracellular vesicles, their origin, composition, purpose, and methods for exosome isolation and analysis. *Cells* **8**, 727 (2019). <https://doi.org/10.3390/cells8070727>
- Dong, G., Wagner, V., Minguez-Menendez, A., Fernandez-Prada, C. & Olivier, M. Extracellular vesicles and leishmaniasis: Current knowledge and promising avenues for future development. *Mol. Immunol.* **135**, 73–83 (2021). <https://doi.org/10.1016/j.molimm.2021.04.003>
- Marti, M. & Johnson, P. J. Emerging roles for extracellular vesicles in parasitic infections. *Curr. Opin. Microbiol.* **32**, 66–70 (2016). <https://doi.org/10.1016/j.mib.2016.04.008>
- Silverman, J. M. et al. An exosome-based secretion pathway is responsible for protein export from *Leishmania* and communication with macrophages. *J. Cell Sci.* **123**, 842–852 (2010). <https://doi.org/10.1242/jcs.056465>
- Hassani, K., Antoniak, E., Jardim, A. & Olivier, M. Temperature-Induced Protein Secretion by *Leishmania mexicana* Modulates Macrophage Signalling and Function. *PLoS One* **6**, 1–10 (2011). <https://doi.org/10.1371/journal.pone.0018724>
- Mustajab, T. et al. Update on Extracellular Vesicle-Based Vaccines and Therapeutics to Combat COVID-19. *Int. J. Mol. Sci.* **23** (2022). <https://doi.org/10.3390/ijms231911247>

8. Nogueira, P. M. et al. Immunomodulatory Properties of Leishmania Extracellular Vesicles During Host-Parasite Interaction: Differential Activation of TLRs and NF- κ B Translocation by Dermotropic and Viscerotropic Species. *Front. Cell Infect. Microbiol.* **10** (2020). <https://doi.org/10.3389/fcimb.2020.00380>
9. Privé, C. & Descoteaux, A. Leishmania donovani promastigotes evade the activation of mitogen-activated protein kinases p38, c-Jun N-terminal kinase, and extracellular signal-regulated kinase-1/2 during infection of naive macrophages. *Eur. J. Immunol.* **30**, 2235–2244 (2000). [https://doi.org/10.1002/1521-4141\(2000\)30:8<2235::AID-IMMU2235>3.0.CO;2-9](https://doi.org/10.1002/1521-4141(2000)30:8<2235::AID-IMMU2235>3.0.CO;2-9)
10. Joshi, M. B. et al. Molecular characterization, expression, and in vivo analysis of LmexCht1: the chitinase of the human pathogen, Leishmania mexicana. *J. Biol. Chem.* **280**, 3847–3861 (2005). <https://doi.org/10.1074/jbc.M412299200>
11. Guay-Vincent, M.-M. et al. Revisiting Leishmania GP63 host cell targets reveals a limited spectrum of substrates. *PLoS Pathog.* **18**, 1–17 (2022). <https://doi.org/10.1371/journal.ppat.1010640>
12. Zauli, R. C. et al. in *Leishmaniasis* (ed de Azevedo Calderonon, L.) chap. 3 (IntechOpen, 2021). <https://doi.org/10.5772/intechopen.101151>
13. Taheri, T., Seyed, N., Mizbani, A. & Rafati, S. Leishmania-based expression systems. *Appl. Microbiol. Biotechnol.* **100**, 7377–7385 (2016). <https://doi.org/10.1007/s00253-016-7712-4>
14. Shokouhy, M. et al. Isolation, characterization, and functional study of extracellular vesicles derived from Leishmania tarentolae. *Front. Cell Infect. Microbiol.* **12** (2022). <https://doi.org/10.3389/fcimb.2022.921410>
15. Bandi, C. et al. Leishmania tarentolae: a vaccine platform to target dendritic cells and a surrogate pathogen for next generation vaccine research in leishmaniasis and viral infections. *Parasites & Vectors* **16**, 35 (2023). <https://doi.org/10.1186/s13071-023-05651-1>
16. Dai, X., Xiong, Y., Li, N. & Jian, C. in *Vaccines—the history and future* (ed Kumar, V.) chap. 3 (IntechOpen, 2019). <https://doi.org/10.5772/intechopen.84626>
17. Heaton, P. M. Challenges of developing novel vaccines with particular global health importance. *Front. Immunol.* **11**, 517290 (2020). <https://doi.org/10.3389/fimmu.2020.517290>
18. Shkair, L. et al. Membrane microvesicles as potential vaccine candidates. *Int. J. Mol. Sci.* **22**, 1142 (2021). <https://doi.org/10.3390/ijms22031142>
19. Sabanovic, B., Piva, F., Cecati, M. & Giulietti, M. Promising extracellular vesicle-based vaccines against viruses, including SARS-CoV-2. *Biology* **10**, 94 (2021). <https://doi.org/10.3390/biology10020094>
20. Montaner-Tarbes, S., Borrás, F. E., Montoya, M., Fraile, L. & Del Portillo, H. A. Serum-derived exosomes from non-viremic animals previously exposed to the porcine respiratory and reproductive virus contain antigenic viral proteins. *Vet. Res.* **47**, 1–10 (2016). <https://doi.org/10.1186/s13567-016-0345-x>
21. Anticoli, S. et al. An Exosome-Based Vaccine Platform Imparts Cytotoxic T Lymphocyte Immunity Against Viral Antigens. *Biotechnol. J.* **13**, 1700443 (2018). <https://doi.org/10.1002/biot.201700443>
22. Polak, K. et al. Extracellular vesicle-based vaccine platform displaying native viral envelope proteins elicits a robust anti-SARS-CoV-2 response in mice. Preprint at <https://doi.org/10.1101/2020.10.28.357137> (2020).
23. Coalition for Epidemic Preparedness Innovations. CEPI partners with Codiak BioSciences to develop broadly protective Beta-coronavirus vaccine (2022); <https://cepi.net/cepi-partners-codiak-biosciences-develop-broadly-protective-beta-coronavirus-vaccine>
24. Reuters. Cash-strapped biotech firm Codiak files for bankruptcy protection (2023); <https://www.reuters.com/business/healthcare-pharmaceuticals/covid-vaccine-developer-codiak-files-us-bankruptcy-protection-2023-03-27/>
25. Rappazzo, C. G. et al. Recombinant M2e outer membrane vesicle vaccines protect against lethal influenza A challenge in BALB/c mice. *Vaccine* **34**, 1252–1258 (2016). <https://doi.org/10.1016/j.vaccine.2016.01.028>
26. Shehata, M. M. et al. Bacterial Outer Membrane Vesicles (OMVs)-Based Dual Vaccine for Influenza A H1N1 Virus and MERS-CoV. *Vaccines* **7** (2019). <https://doi.org/10.3390/vaccines7020046>
27. Janeway, C. A., Travers, P., Walport, M. & Capra, J. D. *Immunobiology: the immune system in health and disease* (Garland Science, 2000).
28. Shen, W. et al. A Single Extracellular Vesicle (EV) Flow Cytometry Approach to Reveal EV Heterogeneity. *Angew. Chem.* **57**, 15675–15680 (2018). <https://doi.org/10.1002/anie.201806901>
29. de los Milagros Bassani Molinas, M., Beer, C., Hesse, F., Wirth, M. & Wagner, R. Optimizing the transient transfection process of HEK-293 suspension cells for protein production by nucleotide ratio monitoring. *Cytotechnology* **66**, 493–514 (2014). <https://doi.org/10.1007/s10616-013-9601-3>
30. Li, X. & Shen, J. Humanization of yeasts for glycan-type end-products. *Front. Microbiol.* **13**, 930658 (2022). <https://doi.org/10.3389/fmicb.2022.930658>
31. Do Minh, A. et al. Characterization of Extracellular Vesicles Secreted in Lentiviral Producing HEK293SF Cell Cultures. *Viruses* **13** (2021). <https://doi.org/10.3390/v13050797>

